Advancing Datacenter Interconnects with High-Speed Silicon Photonic and Thin-Film Lithium Niobate Transmitters

Essam Berikaa

Department of Electrical & Computer Engineering
McGill University
Montréal, Canada
June, 2023

A thesis submitted to McGill University in partial fulfillment of the requirements of the degree of Doctor of Philosophy

Abstract

The relentless growth of internet traffic demand, along with the rising traction of bandwidth-intensive applications, is driving datacenters to seek higher transmission capacities. The transceiver market is primarily divided into two main architectures: intensity modulation direct detection (IMDD) transceivers, which operate in the O-band for short-reach intra-datacenter communications (under 10 km), and intensity and phase modulation with coherent detection (coherent) transceivers, which operate in the C-band for inter-datacenter and long-haul communications (typically beyond 40 km). The performance of transmission systems has traditionally been limited by the transmitter electro-optic modulator. Therefore, this thesis focuses on studying the architectures and system-level trade-offs for both IMDD and coherent transmission systems utilizing silicon photonics (SiP) and thin-film lithium niobate (TFLN) modulators.

The thesis explores the wavelength-architecture 2×2 matrix. In the first part, we focus on IMDD systems using both SiP and TFLN MZMs in both O-band and C-band applications. With early access to TFLN technology, we demonstrate the capability of driving TFLN MZMs with sub 1 V_{pp} single-ended driving swings, achieving net 300 Gbps transmission rates. Additionally, we propose a transmitter architecture that eliminates the need for separate RF drivers and transmitter digital signal processing (DSP), achieving a record net 400 Gbps/λ transmission rate for single digital-to-analog converter (DAC) operation. Furthermore, we conduct experimental comparisons of TFLN MZMs with different transmitter configurations to highlight system-level trade-offs and optimize transmission performance. Subsequently, we propose and validate the design of a SiP vestigial sideband transmitter (VSB) targeting long-reach C-band IMDD transmission. The proposed SiP VSB transmitter architecture employs

pure intensity modulation with a single differential-output DAC, enabling the transmission of 56 Gbaud PAM4 signals over 60 km of dispersion-uncompensated standard single-mode fiber (SSMF) without adding hardware complexity.

In the second part, we propose and advocate employing TFLN-based coherent transmission systems for short-reach intra-datacenter communications (2 to 10 km). We highlight the challenges facing IMDD to stretch beyond 800 Gbps operation. Moreover, we demonstrate the first O-band transmission system operating at net 1.6 Tbps over a single 10 km optical fiber using a single-carrier TFLN O-band coherent transmitter at 167 Gbaud DP-64QAM and the 25% overhead soft-decision forward error-correction (SD-FEC). Furthermore, we provide a detailed power consumption comparison between the different IMDD and coherent candidate architectures for 1.6 Tbps operation, strongly supporting our proposal for adopting TFLN-based coherent transmission for short-reach applications.

The third part demonstrates the first net 1 Tbps/λ transmission over 80 km of SSMF using a single-segment SiP IQ modulator with only electronic equalization at 105 Gbaud DP-64QAM with the 25% overhead SD-FEC. In addition, we study the system-level trade-offs and optimizations that enabled a 30 GHz modulator to support operating beyond 100 Gbaud and achieve this record transmission rate. Our analysis strongly supports SiP for 800 Gbps/λ operation; however, it highlights the trade-off between bandwidth and driving voltage requirements that will pose significant challenges for 1.6 Tbps/λ operation.

In the last part, we propose and validate a method to reduce the equalization-enhanced in-band noise that can be incorporated into the receiver DSP after conventional equalizers and improve transmission performance. In simulations, and validated with experimental data, we observe a gain of 0.5 dB in the signal-to-noise ratio when the proposed method is employed.

Résumé

La croissance incessante de la demande de trafic sur l'Internet pousse les centres de données à des capacités de transmission plus élevées. Le marché des émetteurs-récepteurs est principalement divisé en deux architectures principales : les émetteurs-récepteurs à détection directe à modulation d'intensité (IMDD), qui fonctionnent dans la bande O pour les communications à courte distance à l'intérieur des centres de données (moins de 10 km), et les émetteurs-récepteurs à modulation d'intensité et de phase avec détection cohérente (cohérent), qui fonctionnent dans la bande C pour les communications inter-centres de données et de longue distances (généralement au-delà de 40 km). Cette thèse se concentre sur l'étude des architectures et des compromis au niveau du système pour les systèmes de transmission IMDD et cohérents utilisant la photonique sur silicium (SiP) et les modulateurs en niobate de lithium à couche mince (TFLN).

Dans la première partie de cette thèse, nous utilisons des systèmes IMDD utilisant SiP ou TFLN MZMs pour les applications en bande O et C. Grace à la technologie TFLN, nous démontrons la capacité à piloter des MZMs avec des amplitudes de conduite unipolaires inférieures à 1 V_{pp}, atteignant des taux de transmission nets de 300 Gbps. De plus, nous proposons une architecture d'émetteur qui élimine le besoin de pilotes RF séparés et de traitement numérique du signal (DSP) de l'émetteur, atteignant un taux de transmission net record de 400 Gbps/λ pour une opération avec un seul convertisseur numérique-analogique (DAC). Nous effectuons des comparaisons expérimentales des MZMs TFLN avec différentes configurations d'émetteurs pour mettre en évidence les compromis au niveau du système. Ensuite, nous proposons et validons la conception d'un émetteur à bande latérale vestigiale (VSB) SiP ciblant les transmissions IMDD en bande

C à longue portée avec un seul DAC en sortie différentielle, permettant la transmission de signaux PAM4 de 56 Gbaud sur 60 km de fibre monomode standard (SSMF).

Dans la deuxième partie, nous proposons l'utilisation de systèmes de transmission cohérente basés sur TFLN pour les communications intra-centres de données à courte distance (de 2 à 10 km). Nous mettons aussi en évidence les défis auxquels l'IMDD est confronté pour dépasser les 800 Gbps. De plus, nous démontrons le premier système de transmission en bande O fonctionnant à 1,6 Tbps nets sur une seule fibre optique de 10 km en bande O à 167 Gbaud DP-64QAM et de la correction d'erreur directe à décision souple (SD-FEC) avec un surtaux de 25 %. De plus, nous effectuons une comparaison détaillée de la consommation d'énergie entre les différentes architectures candidates IMDD et cohérentes pour une opération à 1,6 Tbps, soutenant fortement notre proposition d'adopter la transmission cohérente pour les applications à courte portée.

La troisième partie présente la première transmission nette de 1 Tbps/λ sur 80 km de SSMF en utilisant un modulateur SiP IQ à un seul segment avec une égalisation électronique seulement, à 105 Gbaud DP-64QAM avec le SD-FEC à surtaux de 25 %. De plus, nous étudions les compromis et optimisations au niveau du système qui permettent un modulateur de 30 GHz de fonctionner au-delà de 100 Gbaud et d'atteindre ce taux record de transmission. Notre analyse soutient fortement l'utilisation de SiP pour une opération à 800 Gbps/λ ; cependant, elle met en évidence le compromis entre la largeur de bande et les exigences de tension de commande qui représenteront des défis importants pour une opération à 1,6 Tbps/λ.

Enfin, nous proposons et validons une méthode visant à réduire le bruit amplifié en bande qui peut être incorporée dans le DSP du récepteur après les égaliseurs conventionnels. Dans les simulations, et validées avec des données expérimentales, nous observons un gain de 0,5 dB dans le rapport signal sur bruit lorsque la méthode proposée est utilisée.

Acknowledgments

Alhamdulillah, all praise is due to God.

I am deeply grateful to Prof. *David V. Plant* for his unwavering support, guidance, and trust throughout my Ph.D. journey. Prof. *Plant* not only saved my career by allowing me to join his research group when I was at a crossroads and about to leave McGill, but he also helped me grow as a researcher and a person. Despite coming from a different academic background and lacking expertise in optical communication, he believed in me and provided me with the knowledge, skills, and confidence needed to succeed. Being a member of Prof. *Plant's* group has been a privilege and an honor. His technical expertise and mentorship have not only expanded my knowledge but also enhanced my research skills and opened up many opportunities for me. I am also grateful for his guidance in developing managerial and personal skills that will benefit me in my future career. I am fortunate to have worked with Prof. *Plant*, not only because of his exceptional talent as an advisor but also because of his humility and kindness as a human being. His never-ending support and encouragement have been a constant source of inspiration and motivation for me. I cannot thank him enough for his contribution to my academic and personal growth.

I would like to take this opportunity to extend my heartfelt appreciation to my colleague and brother, Md *Samiul Alam*, for his exceptional mentorship and support. His valuable guidance and expertise have played a critical role in shaping my Ph.D. experience. I am grateful to have had him as a mentor and friend, and I will always appreciate his mentorship as an integral part of my professional journey. Also, I want to give a big shoutout to my friend and brother, *Mostafa Khalil*, for being an amazing companion during my Ph.D. years at McGill. *Mostafa*, you made my time at McGill so much more fun and memorable, and I cannot thank you enough

for that. I am truly grateful for the lovely experiences we shared as teaching assistants, and for your friendship throughout the years. I must thank prof. *Thomas Szkopek* for being an amazing instructor and role model.

I cannot express my appreciation enough for all the members of *Plant's* group, both past and present. To those who have come before me, I have learned so much from your exceptional documentation and brilliant codes. Thank you for setting the foundation for my Ph.D. work. To my colleagues *Adam Helmy, Charles St-Arnault, Codey Nacke, Eslam Elfiky, Jinsong Zhang, Kh. Arif Shahriar, Maxime Jacques, Ramon Gutierrez-Castrejo, Reza Maram, Santiago Bernal, Weijia Li, Yannick D'Mello, Yixiang Hu, Xueyang Li, Zhenping Xing, Zixian Wei*, I am extremely grateful for the incredible experiences we shared together. Your guidance, support, and insights have been invaluable to me. You have all contributed to making my time at *Plant's* group unforgettable. In addition, I am so grateful for Mr. *Brent Snow's* help in setting up all the software and all IT-related issues, and Ms. *Maru Basanez* and Ms. *Kay Johnson* for facilitating all the administrative and procurement activities. Thank you all for making my journey at McGill University so much more rewarding and enjoyable.

I cannot forget to thank my amazing friend *Ahmed Hani Saad* and his wife *Kristen Stecher* for being there for our family. I've known *Ahmed* for over 8 years, and he has been a true brother to me, providing constant support and encouragement throughout the journey. *Kristen's* kind and welcoming nature has also been a source of comfort for our family. Your never-ending love and kindness mean so much to us, and we adore the memories we've made together. Thank you for being a part of our lives, and I look forward to many more years of friendship and fun times.

I owe an immeasurable debt of gratitude to my loving family for their ultimate support throughout my Ph.D. To my parents, *Radwan Helmy Berikaa* and *Nora Abdallah*, and to my

sisters *Shrouk* and *Alaa,* and their children *Mohamed Amr*, *Mostafa Elgendy, and Malek Elgendy*, I cannot thank you enough for being an amazing family. Your unconditional love, encouragement, and belief in my abilities have been my secret driving force. I feel so blessed to have been raised in such a supportive and caring family, and for all the incredible memories we've shared together. I also want to thank you for giving me the opportunity to travel abroad and complete my Ph.D. away from home, and for understanding the sacrifices that came with it. Your love and support have never wavered, and I am eternally grateful for everything you have done for me. Thank you and may Allah bless all your days.

I would like to express my heartfelt gratitude to my wonderful wife, *Aliaa*, and my little angel, *Kayan*. Your unconditional love, support, and understanding have been the bedrock of my academic journey. You have been there for me through thick and thin, offering me comfort and encouragement when I needed it the most. Your belief in my abilities has inspired me to push through even when the going got tough. I am so grateful for the love and joy that you bring into my life every day, and for the sacrifices that you have made to support my dreams. I cannot thank you enough for being my pillar of strength, and for giving me the gift of a beautiful family. You are the center of my world, and I love you both.

Finally, I would like to dedicate this work to the memory of my brother-in-law, *Mohamed Elgendy*, who passed away a few months ago. His kind and gentle spirit touched the lives of everyone who knew him, and his passing has left a profound void in our family. I will always remember him as a source of inspiration and encouragement, and I am grateful for the time we had together. This work is dedicated to his memory, as a tribute to his life and his legacy.

Essam Berikaa
June 2023

Associated Publications

The original contributions of the research work presented in this thesis have resulted in 15 first-authored papers, comprising 9 journal papers and 6 conference papers. In these works, I conceived and verified the idea, designed and performed the experiment, and wrote the paper. The other co-authors contributed to discussing the idea, procurement of some devices, and editing the manuscripts. Additionally, through collaboration with members of the Photonics Systems Group at McGill University and researchers from other research groups, I have co-authored 9 journal papers and 10 conference papers that are not directly related to this thesis despite the relevance of the topics.

Journal Articles Related to the Thesis

1. (***Invited***) **E. Berikaa**, M. S. Alam, S. Bernal, R. Gutiérrez-Castrejón, W. Li, Y. Hu, B. Krueger, F. Pittalà, and D. V. Plant, " Next-Generation O-band Coherent Transmission for 1.6 Tbps 10 km Intra-Datacenter Interconnects." *Journal of Lightwave Technology*, 2023.
2. **E. Berikaa**, M. S. Alam, W. Li, S. Bernal, B. Krueger, F. Pittalà, and D. V. Plant, "TFLN MZMs and Next-Gen DACs: Enabling Beyond 400 Gbps IMDD O-band and C-band Transmission", *IEEE Photonics Technology Letters*, vol. 35, no. 15, pp. 850-853, 2023.
3. **E. Berikaa**, M. S. Alam, and D. V. Plant, "Beyond 300 Gbps Short-Reach Links Using TFLN MZMs With 500 mV pp and Linear Equalization," *IEEE Photonics Technology Letters*, vol. 35, no. 3, pp. 140-143, 2022.

4. **E. Berikaa**, M. S. Alam, and D. V. Plant, "Net 400-Gbps/λ IMDD transmission using a single-DAC DSP-free transmitter and a thin-film lithium niobate MZM," *Optics Letters,* vol. 47, no. 23, pp. 6273-6276, 2022.
5. **E. Berikaa**, M. S. Alam, and D. V. Plant, "Silicon photonic modulators for net 300 Gbps/λ IM/DD and Net 1 Tbps/λ coherent transmission using All-Electronic equalization," *Optical Fiber Technology,* vol. 74, pp. 103056, 2022.
6. **E. Berikaa**, A. Janta-Polczynski, B. Sow, L. Xu, N. Liu, D. Deptuck, Y. Wang, C. Li, P. G.-Q. Lo, and D. V. Plant, "Net 67 Gbps Transmission Over 2 km at Sub 1 V_{pp} Using Packaged Silicon Photonic MZM," *IEEE Photonics Technology Letters,* vol. 34, no. 21, pp. 1139-1142, 2022.
7. **E. Berikaa**, M. S. Alam, and D. V. Plant, "Unamplified Coherent Transmission of Net 500 Gbps/Polarization/λ for Intra-Datacenter Interconnects," *IEEE Photonics Technology Letters,* vol. 34, no. 21, pp. 1135-1138, 2022
8. (***Invited***) **E. Berikaa**, M.S. Alam, A Samani, E. El-Fiky, Y. Hu, S. Lessard, and D.V. Plant, "Silicon Photonic Single-Segment IQ Modulator for Net 1 Tbps/λ Transmission Using All-Electronic Equalization," *Journal of Lightwave Technology*, 2022.
9. **E. Berikaa**, M. S. Alam, M. Jacques, X. Li, P.-C. Koh, and D.V. Plant, "2D Constellation Distortion for Subduing Equalization Noise in Bandwidth-Limited IMDD Systems," I*EEE Photonics Technology Letters,* vol. 34, no. 6, pp. 267-270, 2022.

Conference Articles Related to the Thesis

10. (***Post-Deadline***) **E. Berikaa**, M. S. Alam, S. Bernal, W. Li, B. Krueger, F. Pittalà, and D. V. Plant, "Net 1.6 Tbps O-band Coherent Transmission over 10 km Using a TFLN IQM and DFB Lasers for Carrier and LO." *Optical Fiber Communication Conference (OFC),* p. Th4B. 1, 2023.

11. **<u>E. Berikaa</u>**, M. S. Alam, Y. Hu, W. Li, and D. V. Plant, "C-band 100 Gb/s Transmission over 40 km SSMF Using a Silicon Photonic Vestigial Sideband Transmitter Based on Dual-Drive MZM and Passive Optical Delay Line." *Optical Fiber Communication Conference (OFC)*, p. Th3E. 7, 2023.
12. **<u>E. Berikaa</u>**, M.S. Alam, and D.V. Plant, "EDFA-Free Net 500 Gbps Transmission over 2 km Using a Thin-Film Lithium Niobate IQM," *IEEE Photonics Conference (IPC)*, p. TuF3.2, 2022.
13. **<u>E. Berikaa</u>**, M. S. Alam, Y. Hu, S. Lessard, and D. V. Plant, "Equalization Noise Reduction Through Constellation Distortion in Coherent Systems." *Signal Processing in Photonic Communications (SPPCom)*, p. SpM2I. 4, 2022.
14. **<u>E. Berikaa</u>**, M.S. Alam, A. Samani, S. Bernal, S. Lessard, and D.V. Plant, "Transmission of 100 GBaud 64QAM Using an All-Silicon IQ modulator," *Conference on Lasers and Electro-Optics (CLEO)*, p. SF3M. 3, 2022.
15. **(*Post-Deadline*)** **<u>E. Berikaa</u>**, M.S. Alam, A. Samani, S. Lessard, and D.V. Plant, "Net 1 Tbps/λ Transmission Over 80 km of SSMF Using a Single Segment SiP IQM With All-Electronic Equalization," *Optical Fiber Communication Conference (OFC)*, p. Th4A.5, 2022.

Journal Articles Not Directly Related to the Thesis

16. J. Zhang, **<u>E. Berikaa</u>**, R. Gutierrez-Castrejon, M. S. Alam, F. Cavaliere, S. Lessard, Z. Wei, W. Li, and D. V. Plant, "PAPR reduction and nonlinearity mitigation of optical digital subcarrier multiplexing systems with a silicon photonics transmitter," *Journal of Lightwave Technology*, 2023.
17. (***Invited***) Y. Hu, X. Li, D. Mao, M. S. Alam, **<u>E. Berikaa</u>**, J. Zhang, S. Bernal, A. Samani, M. E. Mousa-Pasandi, M. O'Sullivan, and D. V. Plant, "Silicon Photonic

Phase-diverse Receiver Enabling Transmission of >Net 250 Gbps/λ over 40 km for High-speed and Low-cost Short-Reach Optical Communications" *Journal of Lightwave Technology*, 2023.

18. M. Khalil, H. Sun, **E. Berikaa**, D. V. Plant, and L. R. Chen, "Electrically reconfigurable waveguide Bragg grating filters," *Optics Express*, vol. 30, no. 22, pp. 39643-39651, 2022.
19. M. S. Alam, **E. Berikaa**, and D. V. Plant, "Net 350 Gbps/λ IMDD transmission enabled by high bandwidth thin-film lithium niobate MZM," *IEEE Photonics Technology Letters,* vol. 34, no. 19, pp. 1003-1006, 2022.
20. Y. D'Mello, S. Bernal, A. Helmy, **E. Berikaa**, O. Carpentier, I. Alamgir, M.S. Alam, E. El-Fiky, and D.V. Plant, "Standalone, CMOS-based Faraday rotation in a silicon photonic waveguide," *Optics Express*, vol. 30, no. 14, pp. 24602-24610, 2022.
21. M. S. Alam, X. Li, M. Jacques, **E. Berikaa**, P.-C. Koh, and D.V. Plant, "Net 300 Gbps/λ Transmission Over 2 km of SMF with a Silicon Photonic Mach-Zehnder Modulator," *IEEE Photonics Technology Letters*, vol. 33, no. 24, pp. 1391-1394, 2021.
22. Y. Zhong, **E. Berikaa**, J. Lu, X. Yin, and S. Zhao, "Molecular beam epitaxial growth and optical characterization of AlGaN nanowires with reduced substrate temperature," *AIP Advances,* vol. 10, no. 2, pp. 025022, 2020.
23. F. M. Pont, A. Molle, **E. Berikaa**, S. Bubeck, and A. Bande, "Predicting the performance of the inter-Coulombic electron capture from single-electron quantities," *Journal of Physics: Condensed Matter,* vol. 32, no. 6, pp. 065302, 2019.
24. A. Molle, **E. Berikaa**, F. M. Pont, and A. Bande, "Quantum size effect affecting environment assisted electron capture in quantum confinements," *The Journal of Chemical Physics*, vol. 150, no. 22, pp. 224105, 2019.

Conference Articles Not Directly Related to the Thesis

25. W. Li, F. Eltes, **E. Berikaa**, M. S. Alam, S. Bernal, C. Minkenberg, S. Abel, and D. V. Plant, “Performance Analysis of BTO-Based MZM for 200 Gbps/λ O-band Intra-Datacenter Interconnects” *European Conference and Exhibition on Optical Communication (ECOC)*, 2023.

26. (***Invited***) M. Khalil, **E. Berikaa**, M. S. Alam, K. A. Shahriar, Y. Xie, J. Liu, Z. Lu, P. J. Poole, J. Weber, D. V. Plant, and L. R. Chen, “Performance of Quantum-Dash Mode-Locked Laser Diode (QD-MLLD) for Data Rates Beyond Tb/s in WDM Coherent Transmission Over 80 km-SMF,” *Signal Processing in Photonic Communications (SPPCom),* 2023.

27. (***Invited***) L. R. Chen, M. Khalil, Y. Xie, H. Sun, **E. Berikaa**, M. S. Alam, D. V. Plant, J. Liu, and Z. Lu, “Quantum Dash Optical Frequency Comb Sources for Optical Communications and Microwave Photonics.” *Photonics North (PN)*, p. 1, 2023.

28. (***Post-Deadline***) F. Eltes, W. Li, **E. Berikaa**, M. S. Alam, S. Bernal, C. Minkenberg, D. V. Plant, and S. Abel, "Thin-film BTO-based modulators enabling 200 Gb/s data rates with sub 1 V_{pp} drive signal." *Optical Fiber Communication Conference (OFC),* p. Th4A. 2, 2023.

29. M.S. Alam, **E. Berikaa**, and D.V. Plant, “High Bandwidth Thin-Film Lithium Niobate MZM for Net 300 Gbps/λ IM/DD Transmission,” *IEEE Photonics Conference (IPC),* p. TuF3.3, 2022.

30. **E. Berikaa**, S. Bernal, M. Hammood, L. Chrostowski, and D.V. Plant, “Misalignment-Tolerant MultiTip Inverse Tapered Silicon Nitride Edge Couplers,” *IEEE Photonics Conference (IPC)*, p. ME4.1, 2022.

31. (***Post-Deadline***) Y. Hu, X. Li, D. Mao, M. S. Alam, **E. Berikaa**, J. Zhang, A. Samani, M. E. Mousa-Pasandi, M. O’Sullivan, and C. Laperle, "Transmission of Net 200 Gbps/λ

over 40 km of SMF Using an Integrated SiP Phase-Diverse Receiver." *European Conference and Exhibition on Optical Communication (ECOC),* p. Th3B. 6, 2022.

32. **E. Berikaa**, S. Bernal, Y. D'Mello, D. Mao, and D. Plant. "Misalignment-Tolerant Ultra-Broadband Edge Coupler Based on 10 inverse tapers" *Photonics North (PN)*, p. 1, 2021.
33. **E. Berikaa**, F. Cavaliere, J. Zhang, R. Gutiérrez-Castrejón, L. Giorgi, A. D'Errico, S. Lessard, and D. Plant, "Adapting the Classical Optical Communication Simulation Framework for Continuous- Variable Quantum key Distribution Simulations," *International Conference on Optical Network Design and Modeling (ONDM)*, pp. 1-4, 2021.
34. **E. Berikaa**, A. Khalil, H. Hossam, M. El-Dessouky, and H. Mostafa, "Multi-bit rram transient modelling and analysis." *International Conference on Microelectronics (ICM)*, pp. 232-235, 2018.

Contents

List of Figures

List of Tables

List of Common Acronyms

1D	One-Dimensional
2D	Two-Dimensional
ADC	Analog-to-Digital Converter
AMF	Advanced Micro Foundry
ASE	Amplified Spontaneous Emission
ASIC	Application-Specific Integrated Circuit
AWG	Arbitrary Waveform Generator
AWGN	Additive White Gaussian Noise
B2B	Back-to-Back
BER	Bit Error Rate
BOX	Buried Oxide
BPD	Balanced Photodiode
BW	Bandwidth
CCDM	Constant Composition Distribution Matcher
CD	Chromatic Dispersion
CMOS	Complementary Metal Oxide Semiconductor
CW	Continuous Wave
CWDM	Coarse Wavelength Division Multiplexing
DAC	Digital-to-Analog Converter
DC	Direct Current
DCI	Data Center Optical Interconnects
DD	Direct Detection

DFB	Distributed Feedback
DML	Directly Modulated Laser
DP	Dual Polarization
DSP	Digital Signal Processing
DWDM	Dense wavelength-division multiplexing
ECL	External Cavity Laser
EDFA	Erbium Doped Fiber Amplifier
EML	Externally Modulated Laser
ENoB	Effective Number of Bits
EO	Electro-Optic
ER	Extinction Ratio
FAU	Fiber Array Unit
FFE	Feed Forward Equalizer
FFT	Fast Fourier Transform
FIR	Finite Impulse Response
FO	Frequency Offset
GaAs	Gallium Arsenide
GSSG	Ground-Signal-Signal-Ground
GVD	Group Velocity Dispersion
HD-FEC	Hard-Decision Forward Error Correction
IL	Insertion Loss
IQM	In-Phase Quadrature Modulator
IM	Intensity Modulation
IMDD	Intensity Modulation Direct Detection

InP	Indium Phosphide
ISI	Inter Symbol Interference
IQ	In-phase and Quadrature
KP4-FEC	KP4 Forward Error Correction
LMS	Least Mean Squares
LN	Lithium Niobate
LO	Local Oscillator
LUT	Look-Up Table
MIMO	Multiple-Input and Multiple-Output
MLSD	Maximum Likelihood Sequence Detector
MMF	Multi-Mode Fiber
MPW	Multi-Project Wafer
MSA	Multi-Source Agreement
MZM	Mach-Zehnder Modulator
NGMI	Normalized General Mutual Information
OCT	On-Chip Termination
OIF	Optical Internetworking Forum
OH	Overhead
OMA	Optical Modulation Amplitude
OOK	On-off keying
OSA	Optical spectrum analyzer
OSNR	Optical Signal-to-Noise Ratio
PAM	Pulse Amplitude Modulation
PAPR	Peak-to-average power ratio

PBC	Polarization Beam Combiner
PBS	Polarization Beam Splitter
PC	Polarization Controller
PCB	Printed Circuit Board
PD	Photo-Detector
PDFA	Praseodymium-Doped Fiber Amplifier
PDM	Polarization-Division Multiplexing
PIC	Photonic Integrated Circuit
PLL	Phase-Locked Loop
PMD	Polarization Mode Dispersion
PRBS	Pseudo Random Binary Sequence
PS	Probabilistic Shaping
PSD	Power Spectral Density
QAM	Quadrature Amplitude Modulation
QPSK	Quadrature Phase Shift Keying
RC	Raised Cosine
RF	Radio Frequency
RMS	Root Mean Square
ROP	Received Optical Power
RRC	Root Raised Cosine
RTO	Real Time Oscilloscope
Rx	Receiver
SD-FEC	Soft-Decision Forward Error Correction
SE	Spectral Efficiency

SiP	Silicon Photonics
SMF	Single Mode Fiber
SNR	Signal-to-Noise Ratio
SOI	Silicon-On-Insulator
SOP	State of Polarization
SPP	Series Push-Pull
sps	Sample Per Symbol
TIA	Trans-impedance Amplifier
TFLN	Thin-Film Lithium Niobate
TPS	Thermal phase shifter
TW-MZM	Traveling-Wave Mach-Zehnder Modulator
Tx	Transmitter
VCSEL	Vertical Cavity Surface Emitting Laser
VGC	Vertical Grating Couplers
VNLE	Volterra Nonlinear Equalizer
VOA	Variable Optical Attenuator
VODL	Variable Optical Delay Line
WDM	Wavelength-division multiplexing

Chapter 1

Introduction

1.1 Motivation

The explosive growth and wide deployment of data/bandwidth-hungry applications such as high-definition video streaming, cloud-based services and storage solutions, artificial intelligence, and the internet of things are driving an insatiable increase in global Internet traffic demand. Therefore, it is of utmost priority to improve the data exchange efficiency and bandwidth utilization alongside an increase in the transmission capacity. Datacenter communications dominate the internet traffic with a forecasted traffic of 175 Zettabytes by 2025 [1]. Thus, significant efforts are exerted to increase the capacity of optical datacenter interconnects (DCI) to meet the demand [2, 3]. DCIs serve both intra-datacenter and inter-datacenter communications, which differ inherently in transmission reach as illustrated in Table 1.1. Intra-DCIs function inside the datacenter (500 m to 10 km) with stringent constraints on power consumption, cost, and form factor [2]. Whereas Inter-DCIs handle the communications between datacenters at higher transmission capacities. DCIs employ small form factor pluggable optical transceivers (transmitter-receiver modules) that integrate the application-specific integrated circuit (ASIC) digital signal processing (DSP) engines, RF driving circuitry, and the optical transmitter-receiver componentry.

The optical transceivers market concentrates on minimizing the cost and power consumption per bit while reducing the form factor (size) as much as possible. In reality, power consumption and cost are closely related because of the electricity and cooling running costs, which is a major concern for datacenters [4]. With the expanding energy crisis and soaring prices for oil and gas, it is expected that datacenter operators will consider new transceiver architectures with a higher original (fixed) cost and lower running costs.

The transceiver and network specifications are defined based on the transmission reach, as shown in Table 1.1. The dominant flavors of optical transceivers are (1) intensity modulation with direct detection (IMDD); and (2) intensity and phase modulation with coherent detection (coherent). Compared to coherent, IMDD systems have a simpler architecture and consume less power; hence, they are employed in intra-DCIs. Coherent systems have higher spectral efficiency and achieve higher transmission rates, which makes them the ideal solution for long-reach inter-DCIs [5]. The two system architectures are explained in Chapter 2. The server-to-server communications (under 500 m) employ vertical cavity surface emitting laser (VCSEL) based IMDD transceivers with multi-mode fiber (MMF) [6]. Beyond 500 m, the inter-modal dispersion becomes intolerable, dictating operating with standard single-mode fibers (SSMF). Currently, IMDD transceivers stand as the optimum choice for intra-DCIs up to 10 km, whereas coherent transceivers dominate the inter-DCIs market beyond 40 km [7]. The transitional region between both architectures currently resides between 10 km and 40 km; however, coherent transceivers' standardized reach is continuously growing, and it is anticipated that coherent transceivers will go inside datacenters and dominate the intra-DCIs market in the coming decade [8-12].

Table 1.1. Status of data communication systems

Wavelength	**O-band (1260-1360 nm)**			**C- and L-bands (1530-1625 nm)**		
Architecture	**IMDD**					**Coherent**
Reach (km)	**< 0.5**	**0.5 - 2**	**2 – 10**	**10 – 40**	**40 – 80**	**80 –120**
	Inside the datacenter (Intra-DCI)			**Outside the datacenter (Inter-DCI)**		

The general objective of this thesis is to study the different ways to reduce the cost per bit of intra- and inter-DCIs by increasing the data transmission rate without overlooking power consumption. The optical receivers are well-advanced; 140 GHz bandwidth photodiodes are commercially available [13]. Therefore, our study focuses on the optical transmitter side, particularly the electro-optic modulator and the RF driving scheme. The electro-optic modulator is the device that converts the RF signal carrying data to optical pulses where its main performance metrics are modulation efficiency (voltage requirements), bandwidth, optical insertion loss, linearity, and footprint. Several material systems are used in fabricating electro-optic modulators, such as lithium niobate (LN), indium phosphide (InP), gallium arsenide (GaAs), and silicon (Si) [14]. We focus on Si photonic (SiP) and thin-film lithium niobate (TFLN) modulators because both can be fabricated in commercial foundries accessible by everyone [15-18]. In addition, each platform is better suited for specific application scenarios.

SiP processes have matured in the last decade; enabling the fabrication of high-speed electro-optic modulators, phase shifters, and photodetectors [19-21]. The SiP platform is advantageous considering the fabrication costs, yield, small footprint, and compatibility with the complementary metal oxide semiconductor (CMOS) processing. However, SiP modulators are limited by the high driving voltage requirements and the high optical insertion loss of the devices. Laser integration remains the hardest challenge for SiP; however, III-V lasers are readily heterogeneously integrated into silicon [22, 23].

TFLN is a promising emerging platform that offers high-bandwidth modulators with low driving voltage requirements and ultra-low insertion loss [15, 16]. However, TFLN modulators have a larger footprint, while their fabrication is costly and incompatible with CMOS. Unlike SiP, lasers can be integrated on the TFLN platform in an easier manner [24]. Figure 1.1 presents an illustrative comparison between SiP and TFLN electro-optic modulator typical metrics, based on the public literature. The SiP platform is more mature and has economical advantages; however, its modulators have inferior specifications (performance) compared to TFLN modulators.

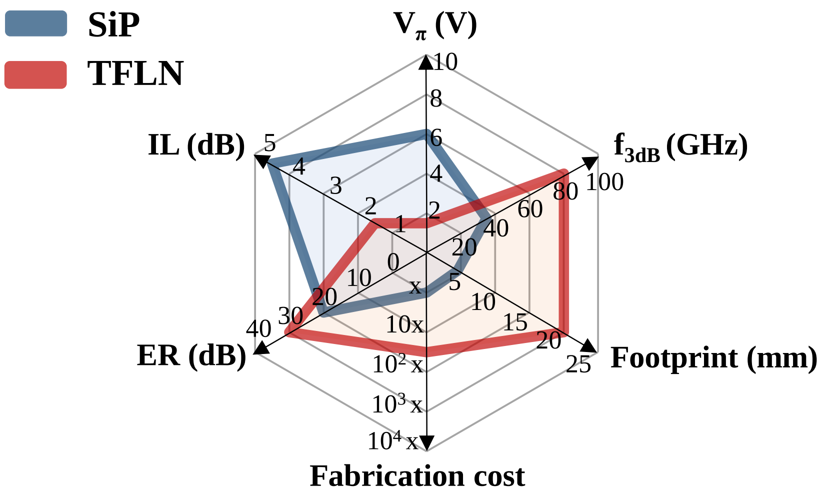

Figure 1.1. Comparison of the typical metrics of SiP and TFLN electro-optic modulators. V_π: half-wave voltage; f3dB: 3-dB electro-optic bandwidth (S21); IL: optical insertion (excess) loss; ER: optical extinction ratio.

Therefore, the objectives of the thesis are: (1) experimentally demonstrate high-speed data transmission using SiP and TFLN modulators for intra-DCIs and inter-DCIs reach; (2) study the system-level and design-level trade-offs for both material systems in practical systems; (3) validate possible hardware and DSP simplifications that lead to power consumption reduction; (4) investigate the gains and requirements for operating coherent transmission systems inside datacenters (2 to 10 km); and (5) outline the impairments stemming from the high-speed transmission that limit the performance.

1.2 Background

This thesis explores the wavelength-architecture 2×2 matrix, as depicted in Table 1.2. In addition to wavelength and architecture, the transmission reach is considered as a third dimension in this analysis, as it uniquely affects the transmission performance of each configuration. Here, we introduce and explore these various configurations, discussing their specific use cases and challenges. Furthermore, we review the current state-of-the-art performance reported for each configuration.

Table 1.2. The wavelength-architecture 2×2 matrix

	O-band	**C-band**
IMDD transmission	0.5 -10 km (Standard)	10-100 km
Coherent transmission	2 – 20 km	Over 20 km (Standard)

1.2.1 O-band IMDD transmission:

Conventionally, O-band IMDD systems have been widely deployed in data centers for short-reach applications that do not require optical amplification. To enhance their capacity, wavelength division multiplexing (WDM) is employed with spacing of 10 or 20 nm between adjacent channels. Three common transmitter architectures are utilized: directly modulated lasers (DML), externally modulated lasers (EML), and continuous wave (CW) lasers coupled with a Mach-Zehnder modulator (MZM). DML offers a cost-effective solution but suffers from severe frequency chirp as the RF signal is directly applied to the laser cavity, and it is typically limited to 4-level pulse amplitude modulation (PAM4) modulation [25]. EML is also affected by the transient frequency chirp caused by changes in refractive index induced by the RF signal, leading to both the desired intensity modulation and a parasitic phase modulation [25]. The interplay between chirp and chromatic dispersion at the edges of the O-band further limits the DML and EML performance. In contrast, MZMs can operate without introducing chirp when driven in a push-pull configuration, which is an inherent advantage motivating their use over DML and EML solutions.

Recent studies have reported transmission rates of 200 Gbps per lane using both O-band DML and EMLs [26-28]. By leveraging next-generation 256 GSa/s digital-to-analog converter (DAC) and an O-band DML, researchers demonstrated the transmission of 256 Gbaud on-off keying (OOK) and 145 Gbaud PAM4 over 6 km of SSMF with the 6.25% overhead hard-decision forward error correction (HD-FEC), resulting in net rates of 240 Gbps and 273 Gbps, respectively [29]. Another study achieved net 348 Gbps transmission over 5 km using an O-band EML, 128 GSa/s DAC, and strong nonlinear equalization techniques [30]. However, these performances fall short compared to what can be achieved with MZMs, as MZMs allow for higher modulation formats and their versatile structure benefits from advancements in different electro-optic modulator platforms (such as SiP, InP, TFLN, etc.). Using a 70 GHz O-band TFLN MZM, we successfully demonstrated net 400 Gbps transmission over 10 km using 172 Gbaud probabilistically-shaped (PS)-PAM8 modulation with a 20% overhead soft-decision forward error correction (SD-FEC) [31]. Furthermore, researchers achieved net 494.5 Gbps transmission using PS-PAM16 modulation with a C-band TFLN MZM (limited by availability) over 120 m, which is equivalent to the dispersion induced by 2 km at the edges of the O-band [32]. Thus, MZMs prove to be a more practical solution for next-generation interconnects, considering their advantages and the advancements in various electro-optic modulator platforms.

The IEEE 802.3dj standard defines the specifications for the 800GBASE-FR4 Ethernet interface, which operates over a distance of 1-2 km using a coarse (C)-WDM4 200 Gbps/λ solution [33]. However, the challenge lies in extending the performance to support 1.6 Tbps Ethernet while maintaining the same reach. The next milestone on the Ethernet roadmap is 1.6Tbps. Several architectures can achieve this goal, including WDM16 100 Gbps/λ, WDM8 200 Gbps/λ, and WDM4 400 Gbps/λ. Each architecture presents its own set of challenges and limitations. The 100 Gbps/λ and 200 Gbps/λ transceiver technologies are mature, and the main challenge is integrating 16 or 8 copies of these architectures into a small form factor pluggable (SFFP) module while maintaining a feasible power budget. On the other hand, the 400 Gbps/λ architecture is still under development as it requires components with ~100 GHz of bandwidth and it suffers from power fading caused by chromatic dispersion at the edges of the conventional CWDM4 grid. One possible solution is to reengineer the WDM grid, but this requires careful design due to the interplay between chromatic dispersion, fiber nonlinearities, and four-wave mixing (FWM).

1.2.2 C-band IMDD transmission:

The C-band is not considered ideal for direct detection in optical transmission systems due to the presence of chromatic dispersion, which results in significant frequency-selective power fading in the received signal. This power fading penalty becomes more pronounced with higher symbol rates or longer transmission distances, as the first spectral null shifts towards DC (0 Hz). However, C-band IMDD transmission systems are still a viable solution for long-reach applications, particularly in remote areas where optical amplification is necessary. Unlike the O-band, where praseodymium-doped fiber amplifiers (PDFA) are expensive and bulky, C-band systems can leverage the cost-effective and compact erbium-doped fiber amplifiers (EDFA). EDFAs can be integrated into the SFFP modules and provide amplification across the entire C and L wavelength bands. Additionally, the fiber loss in the C-band is approximately 0.12 dB lower than in the O-band, which means that transmitting an O-band signal over 25 km would require twice the optical (laser electrical) power compared to the C-band due to a 3 dB difference. This supports the use of C-band IMDD transmission for applications that require very long-reach capabilities, typically beyond 20 km.

The main challenge in C-band IMDD transmission is the power fading caused by chromatic dispersion, which is discussed in detail in Chapter 2. To overcome this issue, three possible approaches are considered: compensating the chromatic dispersion phase response; transmitting single sideband (SSB) signals; or employing extremely complex DSP to mitigate it. One can compensate for the chromatic dispersion in the optical domain using dispersion-compensating fibers (DCF) inserted before the receiver; however, DCFs are costly. Alternatively, electronic pre-compensation can be performed using complex modulation that manipulate the phase, which can be achieved with a dual-drive (DD)-MZM [34] or In-phase and quadrature (IQ) modulator [35]; this approach requires doubling the number of RF components in the transmitter. The transmission of 100 Gbps/λ over 50 km of dispersion-uncompensated fiber is achieved through digitally pre-compensating the chromatic dispersion with a finite impulse response (FIR) filter and employing an IQ modulator for phase modulation [36]. On the other hand, SSB generation can be achieved through the use of sharp and expensive optical filters or by employing complex modulation, which introduce additional RF componentry and DSP complexity [37, 38]. In [39], they used an RF quadrature hybrid and DD-MZM to create SSB signal, which effectively enabled transmitting over 100 Gbps/λ through 60 km of dispersion-uncompensated fiber. Extensive research efforts are still being devoted to mitigating this impairment with minimal added complexity and cost, aiming to find efficient solutions.

1.2.3 O-band coherent transmission:

The O-band is typically not used for coherent transmission due to several reasons. First, coherent transmission is capable of tolerating chromatic dispersion, so there is no inherent advantage of using the O-band over the C-band in terms of dispersion tolerance. Second, the O-band experiences higher fiber loss compared to the C-band, which can limit the transmission distance. Third, optical amplification in the O-band using PDFAs is costly and impractical. Lastly, coherent transmission requires narrow linewidth lasers, a technology that is not yet mature in the O-band. Moreover, the performance of O-band IMDD transmission has been satisfactory for short-reach communications, making coherent transmission in the O-band less necessary. Consequently, there has been limited motivation to consider O-band coherent transmission, especially considering its potentially higher power consumption in short-reach applications and its unsuitability for long-reach transmission.

The increasing demand for short-reach datacenter communications in the range of 2 to 10 km, coupled with the challenges faced in scaling the capacity of O-band IMDD solutions, has led to the emergence of O-band coherent transmission as a viable option. By operating in the O-band and employing coherent transmission techniques, several system objectives can be effectively addressed. Capacities can be readily increased compared to IMDD solutions. For distances up to 10 km, optical amplification is not required. Digital dispersion compensation is not necessary in the receiver's DSP, which helps reduce power consumption. O-band coherent transmission experiences less equalization-enhanced phase noise (EEPN) in the absence of chromatic dispersion [40]. Lastly, it allows for the use of cost-effective laser sources with larger linewidth. Chapter 4 discusses these points in more details. Additionally, the ongoing scaling of CMOS technology from 7 nm to 3 nm nodes suggests that the power consumption of the

ASIC engines for both IMDD and coherent transceivers will converge, thereby reducing the barriers for coherent solutions to enter the datacenter market [41, 42].

The research on O-band coherent solutions is still relatively limited; however, there have been notable developments in this area [43-46]. Some studies have explored the use of analog coherent architecture, which eliminates the need for extensive DSP at the receiver, aiming to reduce power consumption and overall costs of coherent transceivers [46, 47]. Recently, researchers showcased an integrated SiP transceiver capable of supporting 256 Gbps operation using 64 Gbaud DP-QPSK modulation in a self-homodyne receiver configuration, offering promising results in terms of performance and power efficiency [46]. In terms of high-speed demonstrations, we demonstrated the first O-band coherent transmission system operating at a net capacity of 1.6 Tbps over a distance of 10 km using a single optical carrier and a TFLN modulator [12]. These advancements signify progress towards realizing efficient and high-capacity O-band coherent solutions for intra-DCIs.

1.2.4 C-band coherent transmission:

C-band coherent transmission systems have been standardized for long reach applications, particularly when optical amplification is required. These systems play a critical role in global communications, connecting continents through terrestrial and submarine networks. Currently, the Optical Internetworking Forum (OIF) is working on defining the specifications for the next-generation coherent optical communication interfaces, namely the OIF 800ZR standard [48]. This standard considers various scenarios and specifications based on different transmission distances. For longer reach applications of 80 to 120 km, dense wavelength division multiplexing (DWDM) links with 800 Gbps/λ in the C-band are being considered with the use of optical amplification. In line with our previous discussion on O-band coherent transmission, the OIF is also exploring unamplified fixed wavelength 800 Gbps/λ links for transmission distances of 2 to 10 km. The SiP platform is well-suited for 800 Gbps/λ transmission, but it faces limitations in scaling up to 1.6 Tbps/λ due to the limited electro-optic bandwidth and high driving voltage requirements of SiP modulators.

In [49], researchers developed a SiP IQ modulator capable of supporting 120 Gbaud dual polarization 16-point quadrature amplitude modulation (DP-16QAM) transmission over a distance of 100 km, meeting the requirements set by the OIF 800ZR standard. Additionally, through DP emulation, we demonstrated the successful transmission of a net rate of 1 Tbps using a single-segment SiP IQ modulator over 80 km of SSMF, employing 105 Gbaud DP-64QAM and a 25% overhead SD-FEC [50]. However, it appears that we have reached the practical limits of what can be achieved with SiP technology. The industry is now looking towards alternative material systems to scale the capacity to 1.6 Tbps and beyond. Among the most promising platforms are InP and TFLN, offering higher bandwidth and lower driving voltage requirements, enabling increased capacity and reduced power consumption compared to SiP, albeit with higher costs. Recently, Ciena announced the development of commercial coherent transceivers supporting 1.6 Tbps/λ, which are expected to be available to customers in early 2024 [51]. These transceivers employ InP IQ modulators and will be built using the 3 nm CMOS process. This announcement marks the shift from SiP to other platforms and reflects the industry's direction towards higher symbol rates and wider bandwidths (~100 GHz).

1.3 Organization of the thesis

The thesis is divided into 7 chapters.

In Chapter 2, we discuss the architecture of IMDD and coherent transceivers in detail, along with a description of the data generation and DSP methods.

Chapter 3 focuses on high-speed IMDD systems for the intra-datacenter reach (500 m to 10 km). First, we study the implications of dispensing the RF driver with TFLN modulators. Then, we propose and experimentally validate a simplified transmitter architecture for TFLN-based IMDD systems. Next, we assess the gain of employing the next generation of interleaved DACs, which uses 2 DACs per IMDD channel. Furthermore, we analyze the feasibility of dispensing the RF driver for SiP MZMs. Finally, we propose and validate a SiP vestigial sideband transmitter that reduces the power fading induced by chromatic dispersion and extends the reach of C-band IMDD links.

In Chapter 4, we propose employing TFLN-based coherent solutions inside datacenters in short-reach applications (i.e., 2-10 km). We report the transmission performance of an O-band TFLN-based coherent system employing distributed-feedback (DFB) lasers as a carrier and local oscillator (LO). In addition, we detail the transmission characteristics of an unamplified C-band coherent transmission system and highlight the penalty incurred in the absence of optical amplification. Finally, we discuss the implications of employing external cavity lasers (ECL) versus DFB lasers and operating at the C-band versus the O-band from power consumption, DSP, and technology readiness perspectives.

Chapter 5 presents our work on studying and optimizing SiP coherent systems for inter-DCIs (i.e., 40 km and beyond). We start with a comparative study of two SiP C-band IQ modulators highlighting the design trade-offs and transmission performance. Then, we demonstrate the first net 1 Tbps transmission using a single-segment SiP IQ modulator over 80 km in the C-band with only linear DSP processing, a major milestone for SiP modulators.

In Chapter 6, we concentrate on equalization-enhanced colored noise and its influence on the performance of bandwidth-limited IMDD and coherent systems. We propose a technique based on geometric distortion that effectively subdues colored correlated noise. The proposed method is evaluated using experimental data from the previous chapters' work.

Chapter 7 concludes this thesis and discusses the outcomes of the previous chapters. We further discuss our perspectives on future research work based on this thesis.

1.4 Contributions to Original Knowledge

The original contributions of this thesis can be summarized as follows:

High-speed IMDD transmitters for intra-datacenter reach

- We demonstrate the potential of TFLN modulators with sub 1 V_{pp} driving levels and simplified DSP, while achieving data rates as high as net 300 Gbps. This showcases the capability of TFLN modulators to handle high-speed data transmission with significantly reduced power consumption requirements.
- We further improve the transmission performance of the TFLN MZM by modifying the transmitter architecture and using a higher modulation format. We propose utilizing the DAC at 1 sample per symbol (sps) without any signal processing, directly driving the TFLN modulator without RF amplification. This approach substantially improves the signal-to-noise ratio (SNR) of the transmitted signal, leveraging the low V_{π} characteristic of TFLN MZMs. As a result, we achieve net 410 Gbps transmission at 128 Gbaud PAM16 with the 25% overhead SD-FEC.
- Additionally, we experimentally validate the gain of employing the next generation of interleaved DACs with a sampling rate of 256 GSa/s and improved bandwidth in conjunction with the TFLN platform. Our findings demonstrate that the TFLN platform is currently limited by the bandwidth of the RF components, indicating the potential for even higher transmission rates. Leveraging this advanced DAC, we successfully

transmit 180 Gbaud PAM8, achieving a net data rate of 450 Gbps and a 25% increase in link capacity compared to state-of-the-art 128 GSa/s DAC.

- To provide a comprehensive analysis, we compare the transmission performance achieved using the TFLN MZM with the four different transmitter configurations, enriching the discussion and highlighting important system trade-offs.
- Furthermore, we experimentally assess the potential of employing SiP MZMs with sub 1 V_{pp} driving voltage. Our results reveal that while SiP MZMs are capable of transmitting net 67 Gbps over a distance of 2 km using an 800 mV_{pp} drive signal, there is a significant penalty in performance compared to employing an RF driver, amounting to approximately 50%.
- We propose, design, and experimentally validate a novel SiP vestigial sideband transmitter, which incorporates a DD-MZM with an optical delay line integrated into one of the branches. The primary objective of this VSB transmitter is to mitigate the detrimental effects of chromatic dispersion-induced power fading commonly encountered in long-reach C-band IMDD systems. The designed DD-MZM exhibits a 6-dB bandwidth of 26 GHz, enabling the transmission of 56 Gbaud PAM4 (net 100 Gbps) over 60 km of dispersion-uncompensated SSMF under the 6.7% overhead HD-FEC threshold.

Coherent transmission for high-speed intra-datacenter interconnects (2-10 km)

- We demonstrate the first O-band transmission system operating at net 1.6 Tbps over 10 km of a single fiber by adopting TFLN-based coherent transmission and next-generation of DACs with 167 Gbaud DP-64QAM at the 25% overhead SD-FEC.
- In addition, we experimentally showcase that the penalty associated with using DFB lasers in the system compared to narrow linewidth ECLs is less than 1 dB.

- We present a comprehensive power consumption analysis comparing the different architectures for 1.6 Tbps operation, which supports our proposal of employing TFLN-based single carrier coherent transmission in intra-datacenter interconnects (2-10 km).
- Furthermore, we present the characteristics of TFLN-based unamplified coherent transmission systems, highlighting the requirements on driving swing, optical power budget, and receiver sensitivity.

SiP coherent transmitters for inter-datacenter and long-reach networks

- We present the design and characterization of a single-segment SiP IQ modulator that supports net 1 Tbps operation with only electronic equalization and linear DSP. The SiP IQ modulator has 4 mm phase shifters in series-push-pull (SPP) configuration, featuring 36 GHz 6-dB bandwidth and 10.5 V DC V_π under 1 V reverse bias. Using the state-of-the-art 128 GSa/s DACs and dual-polarization emulation, we transmit 105 Gbaud DP-64QAM over 80 km of SSMF under the 25% overhead SD-FEC bit error rate (BER) threshold, corresponding to a net rate of 1 Tbps. Furthermore, we discuss the design trade-off space and system-level optimizations enabling this performance.

Equalization-enhanced noise reduction in bandwidth-limited systems

- We propose a novel multiplication-free lookup table-based technique that effectively mitigates equalization-enhanced noise in bandwidth-limited IMDD and coherent systems. The proposed method is based on geometrically distorting the signal in higher order to decorrelate colored noise. We validate the proposed method through simulations and with experimental data from SiP transmission experiments under practical bandwidth limitations. We observe 0.5 dB of SNR gain, which improves the transmission performance with modest additional complexity.

Chapter 2

Fundamentals of IMDD and Coherent Systems

2.1 Overview

IMDD and coherent optical transceivers are the two most popular architectures and are widely adopted commercially for various transmission distances. However, there is a continuous competition between system providers to dominate the optical transceiver market. While the concept of coherent detection was well established by 1980 [52, 53], the community abandoned it because of its complex architecture and IMDD systems' sufficient capacity fulfilling the traffic demand until the mid-2000s. Initially, IMDD systems employing OOK sufficiently addressed the market demand. With the increase in data traffic and abundance of bandwidth, WDM emerged and was supported by the co-existence of EDFAs [54]. However, IMDD systems employing OOK have a spectral efficiency of 1 bit/symbol, which could not cope with the exponential growth of data rates. The advancements in microelectronics yielded the development of high-speed DACs and ADCs, paving the way for using higher modulation formats and utilizing DSP at its full potential [55]. Thus, the last two decades have witnessed the revival of spectrally efficient coherent systems alongside IMDD adopting higher pulse amplitude formats, i.e. PAM4. DSP algorithms deployed on ASIC processors handle the data generation, noise filtering, fiber impairments such as polarization mode dispersion and chromatic dispersion, and signal recovery [55].

This chapter reviews the basic architectures of IMDD and coherent systems and analyzes the system impairments in both cases and the state-of-the-art DSP blocks used at the transmitter and receiver. Here, we focus on IMDD and coherent systems only; there are other system architectures proposed in the literature that bridge the spectral efficiency and architectural complexity gap between IMDD and coherent systems, such as carrier-assisted differential detection (CADD) and asymmetric self-coherent detection (ASCD) [56, 57]. However, it is important to acknowledge that these architectures are still in a developmental phase and have yet to reach commercialization.

2.2 Fundamentals of IMDD systems

2.2.1 IMDD transceiver architecture

In conventional IMDD systems, the bit stream is imprinted on the intensity of the optical signal. The intensity modulation at the transmitter can be achieved using DML, EML, or external electro-optic modulators. Although DML and EML solutions are cheaper; however, their usage is limited to relatively low-speed applications due to the chirp. Electro-optic MZMs driven in push-pull configuration enable operating chirp-free and support high-speed operation based on the MZM bandwidth and material platform.

The basic architecture of IMDD systems is depicted in Figure 2.1. At the transmitter, a continuous wave (CW) laser feeds the intensity modulator, MZM, with constant power optical signal. A single DAC channel, either differential or single-ended, is needed to load the signal to the modulator. The DAC output voltage swing is commonly small and insufficient to drive the modulator; hence, the DAC output is first amplified with an RF driver. The output power of the MZM is proportional to the driving modulated signal. Then the optical signal is transmitted over SSMF for a few km, typically up to 10 km. At the receiver, the photodiode (PD) converts the optical signal to a proportional photocurrent that is boosted using a trans-impedance amplifier (TIA) before the ADC. The transmitter and receiver DSP blocks are explained in the following subsections.

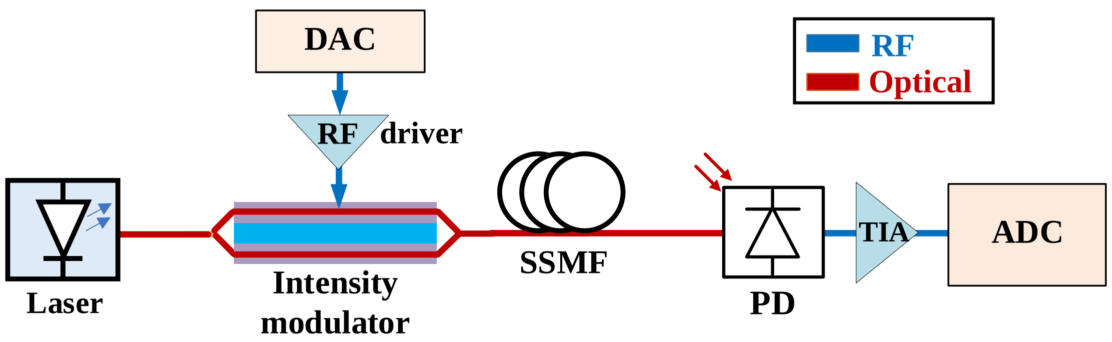

Figure 2.1. Architecture of conventional IMDD systems.

2.2.2 System impairments

2.2.2.1 Fiber attenuation (loss)

IMDD systems operate without optical amplification for cost-effectiveness in the intra-DCI reach. Therefore, considering the fiber loss in power budget calculations is essential. The fiber loss arises from the connectors coupling loss, typically less than 0.5 dB per connector, and the attenuation of the fiber itself that is around 0.35 dB/km in the O-band and 0.2 dB/ km in the C-band. The fiber loss is critical because it defines the signal power at the receiver, and consequently the SNR. Reducing the fiber length (attenuation) increases the received optical power (ROP), and yields better transmission performance.

2.2.2.2 Intersymbol interference (ISI)

Inter-symbol interference (ISI) stems from the limited bandwidth of practical components, i.e. the DAC, RF driver, MZM, PD, TIA, and ADC. The low pass filtering of each of these components broadens the optical pulses in time, leading to their interference. Moreover, the chromatic dispersion (CD) arising from fiber propagation leads to ISI. Chromatic dispersion manifests the dependency of the refractive index (n) and propagation constant (β) on the frequency (ω). The Taylor series expansion of β is given by:

$$\beta(\omega) = \beta_0 + \beta_1(\omega - \omega_0) + \frac{1}{2}\beta_2(\omega - \omega_0)^2 + \cdots \tag{2.1}$$

The Taylor expansion coefficients is given by:

$$\beta_m = \left(\frac{d^m\beta}{d\omega^m}\right)_{\omega-\omega_0}, \text{ for } m = 0, 1, 2, 3, \ldots. \tag{2.2}$$

β_2 is responsible for the major source of dispersion and is often referred to as group velocity dispersion (GVD) coefficient. β_2 can be written as:

$$\beta_2 = \frac{d\beta_1}{d\omega} = \frac{d}{d\omega}\left(\frac{1}{v_g}\right) = \frac{1}{c}\left(2\frac{dn}{d\omega} + \omega\frac{d^2n}{d\omega^2}\right) \tag{2.3}$$

where v_g is the group velocity at which the envelope of the optical pulses propagates in the fiber, and c is the speed of light in vacuum. The fiber dispersion is commonly quantized by the dispersion coefficient D, which is proportional to β_2 according to:

$$D = \frac{-2\pi c}{\lambda^2}\beta_2 \tag{2.4}$$

here λ is the wavelength in vacuum. For SSMF, $D(\lambda)$ equals 0 near 1310 nm (zero-dispersion wavelength). Therefore, IMDD systems used in intra-DCIs operate in the O-band as near as possible to the zero-dispersion wavelength. The CD transfer function is approximated by:

$$H_{CD}(\omega, z) = e^{j\left(\frac{\beta_2 \omega^2}{2} z\right)} \tag{2.5}$$

where z is the propagation distance. CD response acts as all-pass filter with a quadratic phase response. Considering CD, the different frequency components of the signal travel at different velocities or phases, which effectively broadens the pulses in the time domain and adds more ISI. The extension of the symbol pulse to neighbor pulses acts as adding noise to these pulses, which degrades the transmission performance. Fortunately, the impact of ISI can be reduced through transmitter pulse shaping and receiver equalization, as discussed in the DSP section.

2.2.2.3 Chromatic dispersion-induced power fading

Since CD is wavelength dependant, the left and right sidebands of the intensity modulated double sideband (DSB) signal will experience different dispersive phase changes. This difference will cause some incoherence at the phase-insensitive photodetector. This phenomenon results in sharp dips at some frequencies after detection and is referred to as chromatic dispersion-induced power fading. The transfer function of a dispersive IMDD channel in the absence of chirp, assuming push-pull MZM is employed, is given by:

$$H(\omega) = \left|\cos\left(\frac{\beta_2 \omega^2 L}{2}\right)\right| \tag{2.6}$$

where L is the length of the fiber. The position of the spectral dips depends on the dispersion coefficient D and the transmission distance L. The spectral position of the kth dip is given by:

$$f_k = \sqrt{\frac{1+2k}{4\pi|\beta_2|L}} \text{ , for } k = 0, 1, 2, 3, \ldots. \tag{2.7}$$

The frequency of the dips is inversely proportional to $\sqrt{L}$, which sets the limit for the IMDD transmission reach at a given wavelength. Figure 2.2 shows the simulated dispersive IMDD channel response assuming the optical carrier is at the edge of the O-band (Figure 2.2(a)) and the center of the C-band (Figure 2.2(b)). Practically, IMDD systems operate in the O-band near

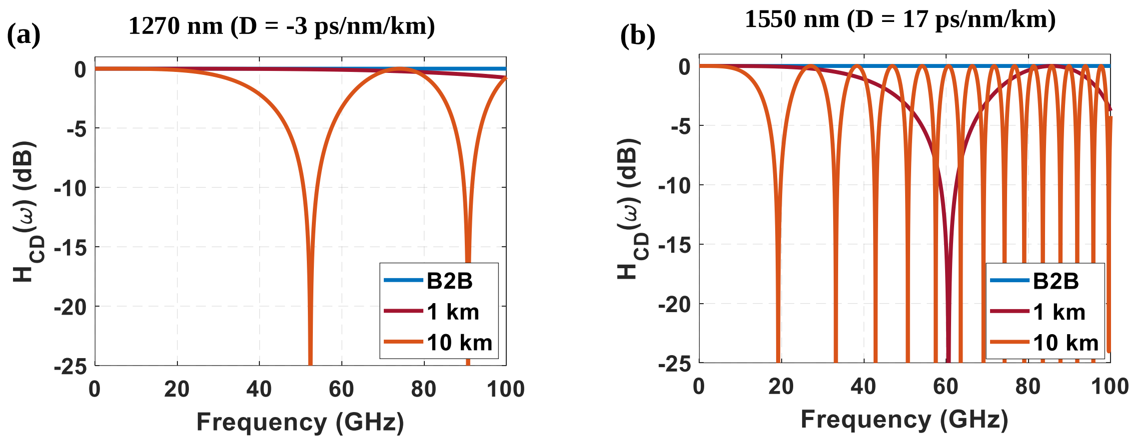

Figure 2.2. The transfer function of dispersive IMDD channel (chirp-free). (a) At the edge of the O-band channel (λ = 1270 nm), and (b) at the center of C-band (λ = 1550 nm)

the zero-dispersion wavelength to avoid these spectral nulls with an acceptable reach of up to 10 km. C-band IMDD systems suffer severely from the CD-induced fading and are limited to less than 1 km; hence, they are not practically deployable from the intra-DCIs market perspective.

2.2.2.4 Nonlinearity

There are several sources of nonlinearity in the IMDD system. Starting from the DAC, the output driving signal is not perfectly linear; especially at higher swing levels. Moving to the RF driver, the transfer function is never linear because of the gain saturation. It is generally recommended to operate below the RF driver 1-dB compression point, where the output power deviates by only 1 dB from the ideal linear transfer function. Similarly, the photodiode saturates when the received optical power is sufficiently high, which adds to the nonlinearity of the system.

Another source of nonlinearity is the MZM transfer function plotted in Figure 2.3, which can be written as:

$$\frac{I_{out}}{I_{in}} = \frac{1}{2} + \frac{1}{2}\cos\left(\frac{\pi}{V_\pi}V(t) + \,\Phi\right) \tag{2.8}$$

where I_{out} is the output intensity, I_{in} is the input intensity, V_π is the half-wave voltage of the MZM, Φ is a phase term to account for the MZM bias point, and $V(t)$ is the modulating signal. The transfer function is not linearly proportional to $V(t)$; however, it is approximately linear for $V(t) << 2V_\pi/3$ and $\Phi = \pi/2$ [58]. In IMDD transmission, we bias the MZM at the quad point (3 dB from maximum), which corresponds to the linear part of the transfer function of the MZM as shown in Figure 2.3. The ratio $V(t)/V_\pi$ is known as the modulation depth and it is a measure of the driving signal strength and linearity. Here we assumed a linear proportionality between the phase and $V(t)$; however, this linear proportionality assumption is only valid for MZMs based on Pockels effect as LN MZMs. Other material systems have nonlinear phase-voltage mapping such as SiP MZMs, which are based on the plasma dispersion effect [58, 59]. Additionally, the optical fiber is a nonlinear transmission channel. SSMF exhibits a third-order nonlinear effect that is known as Kerr nonlinear effect [60]. The Kerr nonlinearity effect refers to the perturbation of the refractive index of the fiber in proportionality to the optical power. Hence, the refractive index is slightly different for high-power pulses.

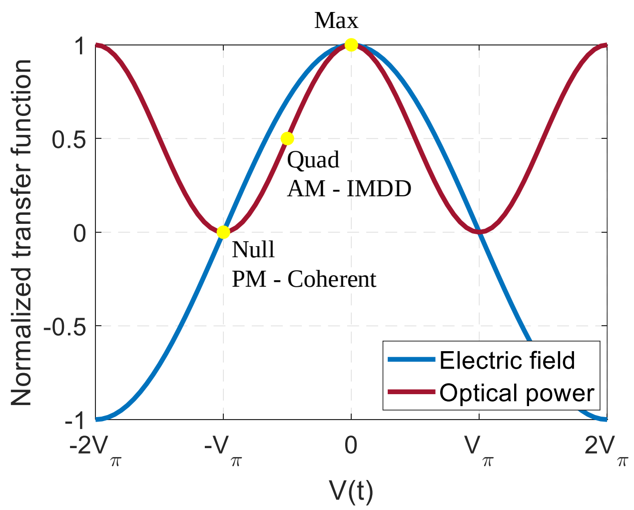

Figure 2.3. The transfer function of the MZM. AM: amplitude modulation; PM: phase modulation

Higher order modulation formats suffer more from the system nonlinearity because of the higher number of levels. The outer levels will have a higher probability of error with smaller eye openings. These nonlinear effects arise from either the strong driving signal or the high optical power launched into the fiber or the photodiode. Although reducing the driving signal swing and the optical power alleviates the nonlinearity constraints, it will degrade the SNR of the signal at the receiver leading to worse performance. Thus, there is a trade-off between signal linearity and SNR, which depends on the receiver's electrical noise. The signal nonlinearity can be compensated at the transmitter with nonlinear pre-distortion of the driving signal [61] or with nonlinear equalization of the received signal [62].

2.2.2.5 Noise

There exist several sources of noise in the IMDD system that limits the achievable SNR. The laser sources exhibit relative intensity noise (RIN) due to spontaneous emissions. Also, all the componentry with electrical interfaces such as the DAC, RF driver, PD, TIA, and ADC suffer from thermal electrical noise. The DAC and ADC also contribute additional noise during signal generation and recovery, such as clock leakage, flicker noise, and quantization noise. Also, DACs and ADCs operate with a finite effective number of bits (ENoB), which distorts the signal and is referred to as quantization noise [63]. In general, higher modulation formats in an IMDD system tend to have a lower tolerance to noise due to the reduction in the Euclidean distance between constellation points (smaller eye openings). In higher-order modulation schemes, more information bits are transmitted per symbol, resulting in a denser constellation diagram with closely spaced constellation points. When the distance between constellation points is smaller, the likelihood of errors increases, as noise can cause the received signal to fall closer to neighboring points, leading to incorrect symbol detection. Therefore, while higher modulation formats offer increased data rates, they also have higher SNR requirements.

2.2.3 IMDD DSP routine

Motivated by the advancements in electronics and the reduction of the cost of ASIC chips, optical transceivers employ DSP engines to compensate for the system impairments and to increase the transmission data rates [2]. The shrinking of the fabrication technology node following Moore's law increases the transistor speed and reduces the power consumption and the footprint of the ASIC chips. These improvements enable optical transceiver market players to include more DSP blocks and functionalities while maintaining the power consumption at an acceptable level for pluggable modules. Here we review the basic DSP blocks used in IMDD transmission systems.

2.2.3.1 Transmitter DSP

At the transmitter, we start by generating the PAM symbols from the binary bit sequence. If the number of PAM levels (PAM order) is a power of 2, the symbol to binary mapping is done by concatenating the binary bits according to the exponent for PAM4, PAM8, and PAM16. However, the generation of PAM6 and PAM12 requires symbol to binary mapping in the complex domain, whereas PAM6 and PAM12 symbols are generated from the standard 32QAM and 128QAM, respectively. Hence, the generation of PAM6 and PAM12 symbols requires an extra time-interleaving step to generate the complex-valued constellation. Moreover, the bit mapping of the 32QAM and 128QAM constellations is not gray bit mapping, which means that 2 neighbor symbols might differ in more than one bit. This increases the error probability slightly and is represented by the gray mapping penalty. After symbol generation, we do some filtering to shape the signal in the time and frequency domains before loading it to the DAC as follows.

2.2.3.1.1 Pulse shaping

As discussed earlier, bandwidth-limited systems introduce ISI that degrades the transmission performance. An effective way to limit the signal bandwidth without introducing more ISI is through pulse shaping with Nyquist pulse-shaping filters. The Nyquist criterion in the time-domain for ISI-free pulse shaping follows:

$$h_{shaping}(nT_s) = \begin{cases} 1 & , for\ n = 0 \\ 0 & , for\ n \neq 0 \end{cases} \tag{2.9}$$

where n is the pulse number ($n = 0$ refers to the center of the original pulse), and $T_s$is the pulse (symbol) duration. This criterion means that the pulse shaping filter does not change the signal at the sampling time of the original pulse (n = 0), and it is equal to zero for all the other pulses ($n \neq 0$) at their sampling times only. This condition guarantees that the filtering will not introduce any ISI, assuming the signals are sampled at the right sampling point. Theoretically, the best pulse-shaping filter is the $sinc$ function because it will shrink the signal bandwidth to its minimum, and is given by:

$$h_{shaping}(t) = \frac{1}{T_s}\frac{\sin(\pi t/T_s)}{\pi t/T_s} = \frac{1}{T_s}\ sinc\left(\frac{t}{T_s}\right) \tag{2.10}$$

$$H_{shaping}(f) = \begin{cases} 1 & , for\ |f| < \dfrac{1}{2T_s} \\ \dfrac{1}{2} & , for\ |f| = \dfrac{1}{2T_s} \\ 0 & , for\ |f| > \dfrac{1}{2T_s} \end{cases} \tag{2.11}$$

The $sinc$ filter is non-causal. It has an infinite duration in the time domain; thus, it does not exist practically. Truncated $sinc$ function filters exit, where they truncate the time-domain pulse shaping to a finite number of pulses. However, the time-domain truncation yields a non-ideal low pass filter in the frequency domain with relatively strong side lobes.

A more practically deployable pulse-shaping filter from the Nyquist family is the raised-cosine (RC) filter because of its flexible implementation. For RC filtering, the impulse response of the filter is controlled by the roll-off parameter α. Small values of α indicates that the filter frequency response approaches the ideal low pass filter. The RC pulse shaping filter has the following impulse response:

$$h_{shaping}(t) = \begin{cases} \dfrac{\pi}{4T_s} sinc(\dfrac{1}{2\alpha}) & , for\ t = \pm\dfrac{T_s}{2\alpha} \\ \dfrac{1}{T_s} sinc\left(\dfrac{t}{T_s}\right) \dfrac{\cos\left(\dfrac{\pi\alpha t}{T_s}\right)}{1-\left(\dfrac{2\alpha t}{T_s}\right)^2} & , otherwise \end{cases} \tag{2.12}$$

$$H_{shaping}(f) = \begin{cases} 1 & , for\ |f| < \dfrac{1-\alpha}{2T_s} \\ \dfrac{1}{2}[\ 1+\cos\left(\dfrac{\pi T_s}{\alpha}(|f| - \dfrac{1-\alpha}{2T_s})\right)] & , for\ \dfrac{1-\alpha}{2T_s} < |f| < \dfrac{1+\alpha}{2T_s} \\ 0 & , for\ |f| > \dfrac{1+\alpha}{2T_s} \end{cases} \tag{2.13}$$

So far, we have considered performing the entire pulse-shaping filtering at the transmitter; however, theoretically employing a matched pulse-shaping filter at the receiver maximizes the SNR. Therefore, the root-raised-cosine (RRC) filters family emerged, which is simply a filter whose frequency response is the square root of the RC filter. Performing RRC filtering at the transmitter and receiver effectively yields the same frequency response as a single RC filter. The RRC filter on its own does not satisfy the Nyquist ISI-free criterion. Yet, the combined response of RRC filtering at the transmitter and receiver yields an ISI-free pulse shaping. The impulse response of the RRC filter is given by:

$$h_{shaping}(t) = \begin{cases} \dfrac{1}{T_s}[1+\alpha\left(\dfrac{4}{\pi}-1\right)] & , for\ t = 0 \\ \dfrac{\alpha}{\sqrt{2}T_s}[\left(1+\dfrac{2}{\pi}\right)\sin\left(\dfrac{\pi}{4\alpha}\right) + (1-\dfrac{2}{\pi})\cos\left(\dfrac{\pi}{4\alpha}\right)] & , for\ t = \pm\dfrac{T_s}{4\alpha} \\ \dfrac{\dfrac{1}{T_s}[sin\left(\dfrac{t\pi}{T_s}(1-\alpha)\right) + \dfrac{4\alpha t}{T_s}\cos\left(\dfrac{t\pi}{T_s}(1+\alpha)\right)]}{\dfrac{t\pi}{T_s}[1-\left(\dfrac{4\alpha t}{T_s}\right)^2]} & , otherwise \end{cases} \tag{2.14}$$

$$H_{shaping}(f) = \begin{cases} 1 & , for\ |f| < \frac{1-\alpha}{2T_s} \\ \sqrt{\frac{1}{2}[\,1 + \cos\,(\frac{\pi T_s}{\alpha}(|f| - \frac{1-\alpha}{2T_s}))]} & , for\ \frac{1-\alpha}{2T_s} < |f| < \frac{1+\alpha}{2T_s} \\ 0 & , for\ |f| > \frac{1+\alpha}{2T_s} \end{cases} \quad (2.15)$$

Other less popular pulse shaping filters exist, such as the gaussian shaping filter. However, we limited the discussion to the RC and RRC filters, which we employed in the experimental work of this thesis.

The roll-off factor (α) is an important optimization parameter that allows adjustment of the signal bandwidth, DAC output swing, and SNR at the transmitter. In Figure 2.4, the simulated eye diagrams illustrate a 64 Gbaud signal pulse-shaped with an RC filter at 2 sps, without bandwidth limitations or added noise. Each subplot notes the roll-off factor, signal bandwidth, and peak-to-average power ratio (PAPR). Increasing the roll-off parameter reduces the signal overshoot (PAPR), resulting in improved eye-opening and higher signal bandwidth. However,

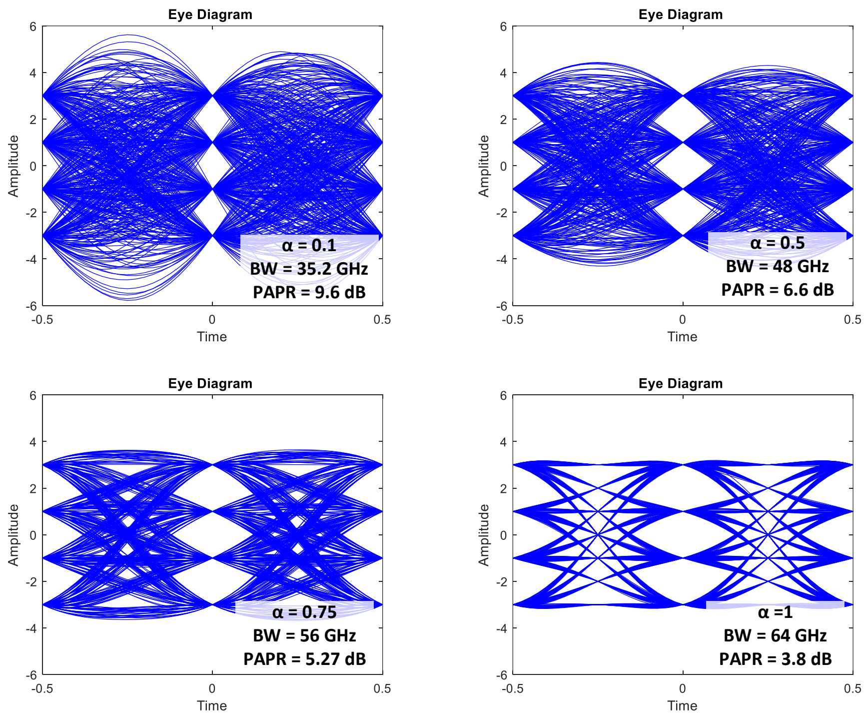

Figure 2.4. The simulated eye diagrams of the signal at the transmitter after RC pulse shaping at different roll-off factor values. BW: bandwidth; PAPR: peak-to-average power ratio

a higher roll-off factor with larger signal bandwidth can introduce significant ISI due to the channel's typical low-pass response. Conversely, using a small roll-off factor increases the signal's PAPR. This overshooting limits the utilization of the DAC's full ENoB since the majority of the signal resides near its average, leading to reduced bit resolution. Consequently, this lowers the root-mean-square (RMS) level of the DAC's output voltage, resulting in lower electrical SNR at the transmitter. As discussed in the next sections, signal clipping may be employed to limit PAPR and preserve SNR, but it comes at the cost of signal distortion. Hence, selecting the appropriate roll-off factor necessitates careful consideration of the symbol rate, modulation format, and channel bandwidth. It is a balance between achieving higher data rates and better spectral efficiency while managing the trade-offs related to PAPR, ISI, and DAC performance.

2.2.3.1.2 Digital pre-emphasis filtering

Pulse-shaping can effectively limit the signal bandwidth to match the system response, which reduces the ISI. Yet, high-speed systems operate at high symbol rates and are limited by the system bandwidth. Therefore, we pre-compensate the frequency response of the transmitter channel partially or completely at the transmitter with a pre-emphasis digital filter. The pre-emphasis digital filter response is ideally the inverse of the response of the system. The transmission system components have a low-pass response; hence, the pre-emphasis filter acts as a high-pass filter to equalize the system frequency response and flatten the signal spectrum

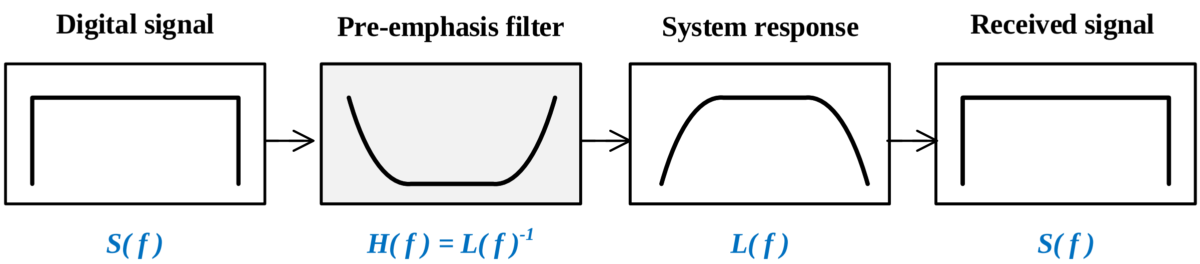

Figure 2.5. Schematic of the pre-emphasis filtering process.

at the receiver. Figure 2.5 presents an illustrative schematic of the pre-emphasis filter response.

Although the receiver employs an equalizer that can compensate for the system frequency response, it is advised to do the pre-emphasis at the transmitter. At the receiver, the signal has already propagated through the channel with additive white gaussian noise (AWGN); thus, the receiver equalizer operates on the low-pass filtered signal alongside the white noise. Equalizing the noise at the receiver correlates the noise samples and is referred to as equalization-enhanced colored noise [64]. Handling the colored correlated noise is more complicated and degrades the transmission performance [64, 65]. Therefore, the transmitter pre-emphasis is very important even in the presence of a receiver equalizer to split the equalization load and reduce the impact of equalization-enhanced noise. In practice and for such high-speed systems, we do partial pre-emphasis filtering at the transmitter because the strong high-pass filtering increases the signal PAPR, which reduces the output signal swing of the DAC and might degrade the RF signal quality and deteriorates the SNR at the transmitter.

In [66], the authors presented an analytical analysis regarding the optimal allocation of pre-emphasis in the transmitter and receiver, taking into account the relative levels of noise at each stage. The findings suggest that the allocation of pre-emphasis depends on the ratio of noise at the transmitter to the noise introduced during channel propagation. If the noise at the transmitter dominates the overall noise contribution, it is optimal to split the pre-emphasis equally between the transmitter and receiver. On the contrary, if the AWGN introduced by the channel dominates the overall noise, it is recommended to perform the entire pre-emphasis at the transmitter. This approach avoids the noise-enhancement effect that could occur at the receiver's equalizer. Therefore, the optimal allocation of pre-emphasis depends on the noise characteristics of the transmitter and the channel. By carefully considering this ratio, the pre-emphasis can be appropriately distributed to optimize the system performance.

2.2.3.1.3 Clipping

The pulse-shaping and pre-emphasis filtering lead to significant time-domain overshooting in the digital signal before loading it to the DAC. The DAC has a finite number of levels and maps the signal to those levels; hence, overshooting leads to a lower average output swing of the DAC. The impact of overshooting is quantized by the PAPR of the digital signal $s[n]$, which is given by:

$$PAPR = \frac{P_{max}}{P_{average}} = \frac{[\max(|s[n]|)]^2}{\frac{1}{n}\sum_n [s[n]]^2} \tag{2.16}$$

High PAPR leads to a small RMS swing out of the DAC. One way to reduce the PAPR is by clipping the signal to limit the PAPR to a reasonable value. Based on the experimental work carried out in this thesis, we observe that the highest acceptable PAPR is 10 dB. Therefore, we always clip the signal to limit its PAPR to a maximum of 10 dB. Yet, too much clipping distorts the signal as clipping impacts only the outer levels and acts as a source of nonlinearity. This distortion is more pronounced at the higher modulation formats (i.e., PAM8).

2.2.3.1 Receiver DSP

At the receiver, the main DSP block is the equalizer that compensates for the introduced ISI. Despite employing pulse-shaping and pre-emphasis filtering, high-speed (symbol rate) transmission requires challenging the system bandwidth. Hence, the receiver DSP compensates for this residual ISI and equalizes the frequency response of the received signal. The linear feed-forward equalizer (FFE) is the most popular equalizer and is already deployed in commercial products because of its simple architecture and low computational complexity. The FFE is represented by:

$$y[k] = \sum_{i=-N}^{N} w_i \, x[k-i] \tag{2.17}$$

where $x[k]$ is the sampled received signal before equalization, $y[k]$ is the output of the equalizer, w_i is the i^{th} filter tap weight, and N is related to the number of filter taps by $N_{taps} = 2 \times N + 1$. This is a linear finite impulse response (FIR) filter and its computational complexity depends on the number of filter taps N_{taps}. Since the FFE compensates for the channel response, the FFE FIR filter has typically a high-pass filter response. Thus, one drawback of FFE is that it converts the channel AWGN to a colored correlated noise at the receiver, commonly referred to as equalization-enhanced noise. However, FFE is advantageous because it compensates for the ISI regardless of the sample position, both pre-cursor and post-cursor ISI. Other equalizers do not enhance the noise as FFE as the decision feedback equalizer (DFE) and the maximum likelihood sequence estimation (MLSE) equalizer; nevertheless, their practical deployment is limited because they are computationally more exhaustive than FFE [2, 67]. After equalization, the equalized symbols are mapped to binary bits based on the modulation format.

2.3 Fundamentals of coherent systems

2.3.1 Coherent transceiver architecture

Coherent transmission systems harness the phase and polarization spaces for modulation; hence, their spectral efficiency is usually 4× that of IMDD systems at the expense of added complexity and DSP processing [10, 52]. Figure 2.6 depicts the transmitter and receiver architectures of a full dual-polarization (DP) coherent transceiver. At the transmitter, four DAC channels generate the in-phase (I) and quadrature (Q) signals for both X and Y polarizations. The RF signals are first amplified by a matched quad set of RF amplifiers. The matching here is critical to minimize the timing and power skew between the four signals. The RF signals drive a DP-IQ modulator, which is composed of two IQ modulators fed with orthogonal polarizations of a CW laser. The IQ modulator is formed by parallelly connecting two MZMs while inducing a 90^0 phase shift to one of them; hence, the outputs of the two MZMs are orthogonal in the phase space. Then, the polarization beam combiner (PBC) combines the outputs of the two IQMs [68]. Coherent transmission systems are typically employed in long-reach inter-DCIs (beyond 40 km); thus, optical amplification after fiber transmission with EDFAs is necessary.

At the receiver, the optical signal is split into two orthogonal polarizations. These two signals do not correspond to the orthogonally polarized signals generated at the transmitter

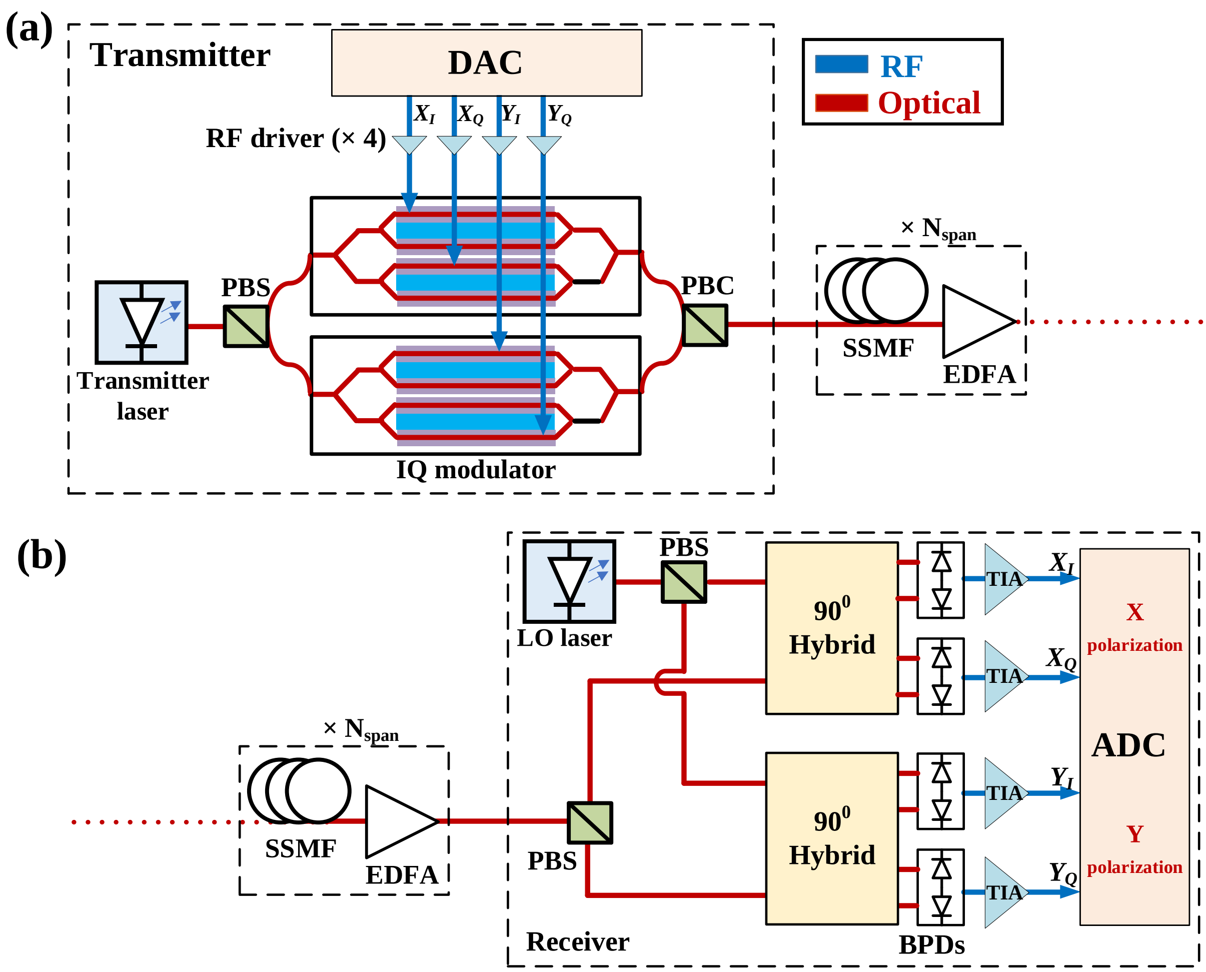

Figure 2.6. Architecture of conventional coherent systems; (a) the IQ transmitter, and (b) the coherent receiver.

because of fiber polarization mode dispersion (PMD). The receiver DSP compensates for the polarization scrambling with adaptive filtering, as discussed in the following subsection. Each signal is mixed with its matched polarization of a local oscillator (LO) laser at nearly the same optical carrier frequency. The outputs of the optical hybrids are detected with a matched quad set of balanced photodetectors (BPD). A matched set of trans-impedance amplifiers (TIA) amplifies the BPDs outputs before feeding them to four ADCs. The matching here means that the set components have similar group delay, frequency response, and gain. After digitizing the signal, the receiver DSP is carried out to compensate for the system imperfections and channel impairments.

2.3.2 System impairments

Coherent systems experience similar impairments as IMDD systems, but with different implications. Fiber attenuation is inevitable; however, coherent systems employ cheap EDFAs that can actually amplify all signals across the C and L wavelength bands. Therefore, unlike IMDD systems, coherent systems' performance is noise-limited, not loss-limited. EDFAs operate in the C-band, which dictates operating coherent inter-DCIs in the C-band wavelength range, whereas IMDD intra-DCIs work in the O-band to avoid dispersion. In addition to the sources of noise discussed for IMDD systems, EDFAs in a coherent system add amplified spontaneous emission (ASE) noise, which limits the optical (O)-SNR and consequently the transmission performance.

As for CD, the coherent receiver captures both the phase and the intensity of the signal; hence, the CD can be compensated easily with a static filter at the receiver DSP because it is a deterministic impairment with a known transfer function. Moreover, the same sources of nonlinearity exist as for IMDD systems. Yet, in coherent transmission, the inner MZMs are biased at the null point to modulate the phase, as shown in Figure 2.3. The MZM's transfer function exhibits an approximate quadratic response, rather than a linear one. As a result, the nonlinearity stemming from the MZM transfer function is more pronounced in coherent transmission compared to IMDD. In the following subsections, we will focus on the impairments related specifically to coherent systems.

2.3.2.1 Laser phase noise and frequency offset

Laser phase noise stems from the undesirable spontaneous emission occurring at both transmitter and receiver LO lasers. The phase noise results in a finite laser linewidth rather than an ideal monochromatic source, which deviates the phase of the CW laser from that of an ideal sinusoidal signal. The laser phase noise is a Gaussian random process with a Lorentzian spectral shape around the laser center frequency [69, 70].

Alongside the phase noise, there is always a finite difference between the center frequencies of the transmitter and receiver lasers because they are independent and not locked in frequency, commonly referred to as frequency offset (FO) ΔF. Therefore, the phase of the output signal of the coherent receiver will be modulated by the offset frequency. Mathematically, the phase noise and frequency offset effect is represented by:

$$r(t) = s(t)e^{j(\Phi_{TX}(t)+\Phi_{RX}(t)+2\pi\Delta F t)} + AWGN \tag{2.18}$$

here $r(t)$ is the received signal after the coherent receiver, $s(t)$ is the transmitted signal, $\Phi_{TX}(t)$ is the transmitter laser phase noise, $\Phi_{RX}(t)$ is the receiver laser phase noise, and ΔF is the frequency offset between the two lasers. $\Phi_{TX}(t)$ and $\Phi_{RX}(t)$ are independent processes.

Coherent transmitters modulate the phase and intensity of the signal altogether, but these impairments distort only the phase of the received signal. External cavity lasers have lower phase noise and laser linewidth; thus, they are used in coherent communication systems.

Fortunately, the receiver DSP corrects both impairments through carrier phase recovery and frequency offset estimation, as discussed in the subsequent sections.

2.3.2.2 IQ timing skew and quadrature error

A serious issue of coherent systems is the timing skew between the signal quadratures (I and Q) arising from the different group delays incurred from the transmission systems components. With this skew, the two signals corresponding to the I and Q quadratures are sampled at a different point relative to their symbols away from the optimum sampling point. This deteriorates the transmission performance severely unless it is accounted for at the receiver DSP by an interpolator that corrects the skew for one quadrature [5].

Quadrature error refers to the static distortion of the received signal because of a nonorthogonal I and Q quadratures in the phase space, namely phase and amplitude imbalance. This quadrature error might arise from an imperfect 90^0 optical hybrid, which induces a $90^0 \pm \theta_{err}$ phase difference between the output signals. In that case, the received signals corresponding to the I and Q quadratures are not perfectly orthogonal, whereas the crosstalk between the two quadratures is proportional to θ_{err}.

Similarly, the imperfect biasing of the IQ modulator leads to a quadrature error; because the orthogonality of the I and Q quadratures is actually established at the transmitter by the parent MZM of the IQ modulator. If the parent MZM is not biased exactly at the quadrature point (3 dB from the maximum transmission point), this will induce some crosstalk between the signal quadratures and distort the received constellation [71].

2.3.2.3 Fiber impairments

We introduce fiber-induced nonlinearities in the previous section impairing IMDD systems; however, coherent systems are more affected by Kerr's effect due to longer transmission distances. In coherent systems, the optical signal is amplified periodically with EDFAs; hence, the optical power after the EDFA is strong enough to trigger several fiber nonlinear processes. Therefore, optimizing the optical launch power into the fiber is critical to address the trade-off between fiber nonlinearities and the SNR at the receiver [60].

Yet, the limitation for coherent systems is the polarization mode dispersion (PMD) which randomly rotates the two orthogonal polarizations of the signal and induces a relative delay and phase difference between them as they propagate along the fiber [72]. PMD originates from the imperfect fabrication of the SMF fiber and the mechanical and thermal stresses applied to the fiber, which asymmetrically deform its core and is denoted as birefringence. Thus, the orthogonal polarization states propagate with slightly different and randomly varied refractive indices. Due to birefringence, the two states of polarization (SOP) exchange their power periodically according to the beat length given by:

$$L_B = \frac{\lambda}{|n_x - n_y|} \tag{2.19}$$

where n_x and n_y are the refractive indices of the two orthogonal polarization modes along the axes of the fiber. Birefringence is a random process, and its significance randomly changes along the fiber. Hence, a convenient representation of the random birefringence stemming from a small section of the fiber is described by:

$$H_z(\omega) = R_z^{-1} D_z(\omega) R_z \tag{2.20}$$

$$D_z(\omega) = \begin{bmatrix} e^{j\left(\frac{\omega\tau}{2}\right)} & 0 \\ 0 & e^{-j\left(\frac{\omega\tau}{2}\right)} \end{bmatrix}, and\ R_z = \begin{bmatrix} \cos(\theta_z) & \sin(\theta_z) \\ \sin(\theta_z) & \cos(\theta_z) \end{bmatrix} \tag{2.21}$$

here τ is the induced differential group delay between the 2 SOPs, and θ_z is the angle of rotation of the SOPs relative to the fiber principle axis. Yet, the total PMD induced by the optical fiber adds the impact of all the segments according to:

$$H_{PMD}(\omega) = \prod_{z} H_z(\omega) \tag{2.22}$$

At the receiver, the optical signal, at random but orthogonal SOPs, is not aligned with the coherent receiver polarization axes. This induces some crosstalk between the two polarizations after mixing with the LO, but the main issue is that the signal SOP changes randomly on the time scale of 1 ms (KHz). The receiver DSP handles the PMD-induced crosstalk by using a multiple-input and multiple-output (MIMO) adaptive equalizer, which updates its filter coefficient at a frequency high enough to follow the changes in SOPs [72].

2.3.3 Coherent DSP routine

2.2.3.1 Transmitter DSP

The coherent transmitter DSP is similar to that of IMDD discussed earlier; however, in a DP coherent system, four IMDD transmitters are effectively required. The complex QAM symbols are generated by concatenating binary bits based on the QAM order. The I signal carries the real part of the QAM symbol, while the Q signal transmits the imaginary part of the symbol. Therefore, the I and Q signals transmit PAM symbols, similar to IMDD. The coherent transmitter DSP blocks, including pulse-shaping filtering, linear pre-emphasis filtering, and clipping, are the same as in IMDD. If the timing skew is measured or known for the system, it can be corrected at the transmitter by introducing some delay on one of the quadrature signals.

However, the main difference lies in the bias point of the modulators. In a coherent system, the child MZMs loaded with the data are biased at null, allowing them to modulate both the phase and amplitude of the signal. Since the modulator is biased at null, the optical signal power is significantly lower compared to the case of IMDD, where an optical carrier is present. This difference gives rise to the term 'modulation loss,' which refers to the difference between the maximum output power of the IQ modulator and the actual output power after loading the RF signal. The typical value for modulation loss is 8 to 10 dB, compromising signal linearity and output power.

2.2.3.2 Receiver DSP

The coherent receiver DSP differs from that of the IMDD systems because coherent optical receivers preserve the phase information of the signal. Here, the coherent receiver DSP deals with two complex-valued signals corresponding to the DP QAM signal. At the receiver, we first correct the timing skew and quadrature errors by delaying one of the signal quadratures and applying Gram-Schmidt orthogonalization [71].

Then, we perform CD compensation. The accumulated CD can be compensated in the time domain by a FIR filter [73] or in the frequency domain by directly multiplying the signal with the inverse of the CD transfer function given by:

$$H_{CD\ comp.}(\omega, z) = H_{CD}(\omega, z)^{-1} = e^{-j\left(\frac{\beta_2\omega^2}{2}z\right)} \tag{2.23}$$

It is recommended to perform the entire receiver DSP in either the frequency domain or the time domain, which minimizes the required computational resources.

After CD compensation, it is essential to estimate the frequency offset and compensate for it. The FO is polarization independent; hence, estimating it for one polarization is sufficient. We estimate the FO frequency from the 4th power of the received signal. Raising the signal to its 4th power folds the phase space and reduces the dependency on the transmitted information; then, the FO frequency component becomes explicit in the spectrum [74]. The FO compensation is performed by multiplying the received signal $r[k]$ with the following phase correction term based on the estimated FO ΔF_{est}:

$$r[k] = r[k]e^{-j(2\pi\Delta F_{est}T_s)} \tag{2.24}$$

Then, an adaptive MIMO equalizer is used to compensate for the ISI and PMD. Assuming a true DP coherent transmission system, the 2×2 complex-valued MIMO equalizer is given by:

$$\begin{bmatrix} E_X^{out} \\ E_Y^{out} \end{bmatrix} = \begin{bmatrix} h_{xx} & h_{xy} \\ h_{yx} & h_{yy} \end{bmatrix} \begin{bmatrix} E_X^{in} \\ E_Y^{in} \end{bmatrix} \tag{2.25}$$

where E_X^{in} and E_Y^{in} are the input complex-field signals, h_{xx}, h_{xy}, h_{yx}, and h_{yy} are the adaptive filters, and E_X^{out} and E_Y^{out} are the equalized complex-field signals corresponding to the polarization multiplexed signals. This equalizer tracks the polarization of the signals and equalizes their frequency response. The complex-valued MIMO equalizer assumes that the I and Q quadratures are orthogonal and synchronized; thus, the filters operate on the complex fields rather than the individual quadratures. Practically, the timing skew and quadrature errors favor employing real-valued 4×4 MIMO equalizers, which can track the polarization, equalize the frequency response, correct timing skew between signal quadratures, and compensate for IQ imbalances [75, 76]. The MIMO 4×4 transfer function is given by:

$$\begin{bmatrix} E_{X,I}^{out} \\ E_{X,Q}^{out} \\ E_{Y,I}^{out} \\ E_{Y,Q}^{out} \end{bmatrix} = \begin{bmatrix} h_{xx,ii} & h_{xx,iq} & h_{xy,ii} & h_{xy,iq} \\ h_{xx,qi} & h_{xx,qq} & h_{xy,qi} & h_{xy,qq} \\ h_{yx,ii} & h_{yx,iq} & h_{yy,ii} & h_{yy,iq} \\ h_{yx,qi} & h_{yx,qq} & h_{yy,qi} & h_{yy,qq} \end{bmatrix} \begin{bmatrix} E_{X,I}^{in} \\ E_{X,Q}^{in} \\ E_{Y,I}^{in} \\ E_{Y,Q}^{in} \end{bmatrix} \tag{2.26}$$

here $h_{\emptyset,\vartheta}$ refers to the filter responsible for the $\emptyset$ (xx, xy, yx, yy) polarization states and ϑ (ii, iq, qi, ii) field individual quadratures. The advantage of employing a real-valued MIMO equalizer is that it operates on each quadrature independently; therefore, it mitigates any residual IQ imbalance or skew [75, 76]. The only drawback is that the real-valued MIMO equalizer requires twice the memory requirements compared to the complex-valued MIMO to store the additional filter taps [75]. These filters adopt a butterfly structure, and their taps are adaptively updated using the least-mean squares (LMS) algorithm.

Eventually, the equalized symbols are demapped to a bit sequence using a hard decision or slicing the symbols' soft values. In this thesis, we assume that the input bit stream is encoded using either a hard decision or a soft-decision forward error correction (FEC) code. Similarly, we have not implemented the FEC decoder at the receiver, but we always consider the FEC code overhead in calculating the net information transmission rate.

2.4 Discussion

Despite the differences between IMDD and coherent transceivers in terms of their architecture, requirements, power consumption, and cost, both will continue to coexist for at least the next decade due to their inherent advantages and features. Table 2.1 presents the system requirements for achieving 800 Gbps with both architectures, based on the current state-of-the-art 200 Gbps per λ or quadrature structures. It is evident that coherent transmission has an advantage in terms of hardware component count compared to IMDD. However, IMDD transmission offers benefits in terms of simpler DSP requirements and lower power consumption.

One of the primary drawbacks of coherent transmission is the fixed fanout granularity, which refers to the flexibility of the output capacity and is approximately four times that of an IMDD system. Additionally, matching the transmitter and receiver LO laser wavelengths requires the use of a thermoelectric cooler (TEC), which consumes considerable power and adds complexity and cost. Yet, the next generation of 400 Gbps/λ WDM IMDD solutions is expected to require TECs. The conventional CWDM grid can not be used at this high symbol rate because of chromatic dispersion; hence, a denser WDM grid is mandatory.

Both architectures benefit from advancements in CMOS technology and the shrinking of process nodes. However, the power consumption reduction achieved through these advancements is more significant for coherent transmission, thereby reducing the difference in power consumption between the two architectures. Consequently, it is anticipated that as technology evolves, the coherent transmission will increasingly penetrate shorter-reach applications and intra-DCIs.

Table 2.1. Overall comparison between IMDD and coherent transceivers requirements for 800 Gbps links

Point of comparison	IMDD transmission	Coherent transmission
Topology	4 × 200 Gbps	1 × 800 Gbps
Number of lasers	4	1 (at higher power)
Laser requirements	uncooled	cooled, linewidth<1MHz
Modulator requirements	4 × MZMs	1 × DP-IQM (4 MZMs)
MZM driving swing	V_D	~ 2 × V_D
Number of DACs	4	4
Number of RF drivers	4	4
Number of photodiodes	4 (single-ended)	4 (balanced)
Number of TIAs	4	4
Number of ADCs	4	4
Tx DSP	pulse-shaping pre-emphasis and clipping	pulse-shaping pre-emphasis and clipping
Rx DSP	Timing recovery Feedforward equalization	IQ deskew CD compensation (C-band) Timing recovery FO estimation Carrier phase recovery Adaptive equalization
Optical Mux/Demux	1	-
Spectral bandwidth	4 × B	B
Fan-out granularity	200 Gbps	800 Gbps

Chapter 3

High-Speed IMDD Transmitters for the Intra-Datacenter Reach

3.1 Overview

As highlighted in Chapter 1, the increasing demand for data traffic, driven by bandwidth-intensive applications like augmented reality, cloud-based services, and streaming platforms, necessitates an increase in the capacity of short-reach intra-DCIs. Currently, IMDD systems are preferred over coherent solutions for distances up to 10 km due to their simpler architecture and lower power requirements. However, with the ongoing surge in demand, it is anticipated that the market will gradually shift towards coherent solutions, a topic further explored in Chapter 4.

Nonetheless, IMDD systems will continue to be relevant and exist, and it is imperative to continue pushing the boundaries of their capacity. The 800G multi-source agreement (MSA) has defined specifications for 200 Gbps/lane IMDD links [33], but there is a persistent need to operate at even higher data rates. In this chapter, we discuss our work on enhancing the performance of IMDD systems, focusing on transmission data rate, power consumption, and reach, leveraging both SiP and TFLN modulator platforms.

3.2 Driver-Less TFLN Transmitters

IMDD systems employing simple PAM formats require wide bandwidth electro-optic (EO) modulators to transmit high symbol rate signals. TFLN has emerged as a promising platform for EO modulators because of its high modulation efficiency, negligible optical insertion loss (~0.7 dB/cm), and low microwave loss [15]; allowing the development of 100 GHz modulators [77, 78]. Yet, TFLN's real promise is operating with CMOS-compatible driving levels and dispensing the power-hungry RF driver circuitry from the transmission system [15, 16, 79]. This is very attractive for DCI applications as it reduces the power consumption of the optical transceiver considerably. The primary limitation of TFLN modulators is the large footprint; however, novel compact designs are being developed to address this footprint challenge without compromising the EO bandwidth or the modulation efficiency [80, 81]. Several studies considered TFLN in IMDD systems; however, only a few studies operated without RF drivers with sub 1 V_{pp} driving. In [16], the authors demonstrated the driver-less transmission of 70 Gbps OOK signal under the 6.7% overhead HD-FEC BER threshold of 3.8×10^{-3} using 60 mV_{pp} driving swing and a 45 GHz TFLN MZM. The driver-less transmission of 100 Gbaud PAM4 under the KP4-FEC BER threshold of 2.4×10^{-4} is reported using a 45 GHz TFLN MZM [80]. This section presents our experimental results on driver-less IMDD transmission using different TFLN MZMs (commercially available through HyperLight). Additionally, we propose a simplified transmitter architecture that eliminates the requirement for an RF driver altogether with the transmitter DSP, while maintaining excellent transmission performance.

3.2.1 Beyond 300 Gbps Short-Reach Links Using TFLN MZMs with 500 mV$_{pp}$ and Linear Equalization [82]

Here, we evaluate the driver-less transmission performance of two C-band TFLN MZMs with varied electrode lengths, 23 mm and 18 mm. Although these MZMs are designed for the C-band, our target application focuses on conventional IMDD systems in the O-band. At the time of the study, the O-band TFLN MZM was still under development. To simulate the O-band conditions, we conduct the transmission over a distance of 500 m in the C-band, which corresponds to a dispersion of 8.5 ps/nm. This dispersion value is equivalent to transmission over more than 2 km at the edges of the O-band.

During our experiments, we characterize thoroughly the MZMs and compare their transmission performance, highlighting the design trade-offs and the characteristics of driver-less operation. Using the long MZM with 500 mV$_{pp}$ driving signal and only linear equalization, we report the transmission of 136 Gbaud PAM8 with the 19.02% SD-FEC, corresponding to a net rate of 342 Gbps.

3.2.1.1 Experimental setup and MZM characterization

Figure 3.1 shows the experimental setup and the DSP blocks employed. At the transmitter, PAM4 and PAM8 symbols are generated directly from a random binary sequence, whereas the

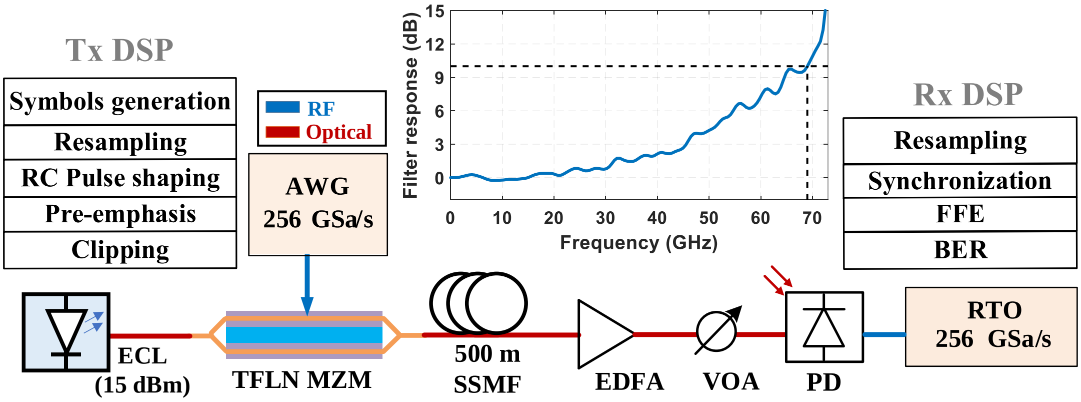

Figure 3.1. (a) The experimental setup and DSP blocks employed at the transmitter (Tx) and receiver (Rx). The inset shows the pre-compensation filter response

PAM6 symbols are derived from the standard 32QAM constellation. The generated symbols are then filtered by a RC pulse shaping filter at 2 sps, and then resampled to the arbitrary waveform generator (AWG) sampling rate (256 GSa/s). This AWG uses an external module to interleave two 128 GSa/s DACs with a 10-dB bandwidth of 70 GHz. The interleaving technology used in the module, although it reduces the overall bandwidth, allows for operation beyond 128 Gbaud while still adhering to the Nyquist criterion. The module has a hard stop at 75 GHz with more than 20 dB of attenuation. We pre-compensate the frequency response of the AWG and a 10 cm RF cable (1.85 mm connectors) up to 74 GHz using the digital pre-emphasis filter depicted in the inset of Figure 3.1. The 10 dB point is around 70 GHz. We are not employing a RF driver after the AWG; thus, clipping the signal is essential to limit its PAPR. Signal clipping reduces the PAPR and subsequently increases the RMS of the driving signal at the expense of inducing some nonlinearity and distortion in the generated signal. The clipped signal is loaded to the AWG running at 256 GSa/s, which drives the TFLN MZM directly through a 67 GHz GSG probe.

Optically, the TFLN MZM is fed by a 15 dBm tunable ECL and is connected via vertical grating couplers (VGC) that have 10 dB back-to-back coupling loss. The output of the MZM is transmitted over 500 m of SSMF, corresponding to ~8-9 ps/nm dispersion. This is equivalent to the dispersion induced by ~3 km O-band transmission for the edge channels in the CWDM grid (i.e., 1270 and 1330 nm). We needed to boost the optical power (to 7 dBm) before the receiver using an EDFA to compensate for the VGCs loss since we employed a conventional 70 GHz PIN photodiode (0.63 A/W) without a TIA. Practically, the TFLN MZM will be connected via edge couplers (1.5 dB/facet), and a high bandwidth PIN PD with TIA can improve the receiver sensitivity; dispensing the need for optical amplification. The variable optical attenuator (VOA) is added for sweeping the received optical power (ROP). The PD output is captured by the 256 GSa/s real-time oscilloscope (RTO) and processed offline.

At the receiver, we first resample the received signal to 2 sps and process it with a 71 tap T/2 spaced linear feed-forward equalizer (FFE), unless mentioned otherwise. Finally, the equalized signals are down-sampled to 1 sps for BER and the normalized generalized mutual information (NGMI) calculations.

Operating without an RF driver has several implications on the system performance as follows: (1) the driving signal swing is smaller, which alleviates the nonlinearity concerns at the expense of a lower optical extinction ratio after modulation; (2) it yields higher transmitter SNR for the driving RF signal; and (3) it improves the system bandwidth as the RF driver induces some drop at 70 GHz. Thus, only linear signal processing is considered in this work. Employing nonlinear equalizers improves the performance marginally, which does not justify the added complexity. Moreover, dispensing the RF driver reduces the overall system cost, power consumption, and packaging requirements; however, it might lead to a manageable penalty in the transmission performance, as discussed in the next section.

This work compares the transmission performance of two TFLN MZMs fabricated on the same run at an accessible commercial foundry (HyperLight). The MZMs have the same structure and differ only in the coplanar waveguide electrode lengths: 23 mm long MZM and 18 mm short MZM. The MZMs come with nearly 50 Ω on-chip termination and are biased with a thermal phase shifter. Figure 3.2(a) shows the measured frequency response of both

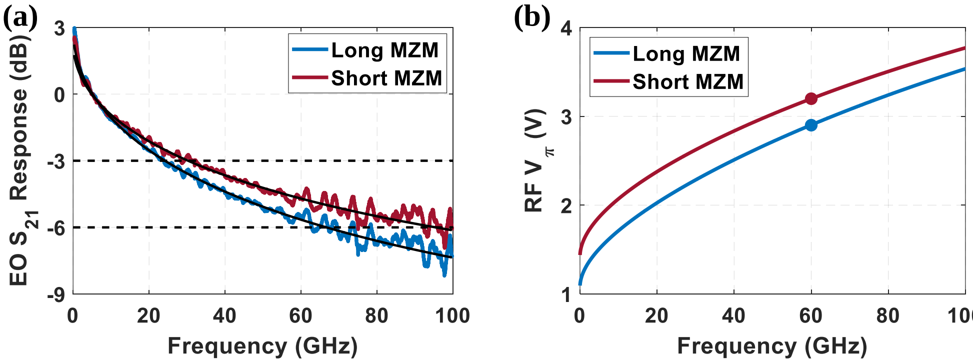

Figure 3.2. (a) The EO frequency response normalized to 5 GHz. (b) The measured and extrapolated RF V_π of the long and short TFLN MZMs.

MZMs. The long MZM has a 24 (66) GHz 3-(6-) dB bandwidth, while the short MZM has 30 (95) GHz 3-(6-) dB bandwidth. Since we pre-compensate the AWG frequency response at the transmitter, the receiver DSP needs to equalize the frequency response of the MZM and PD only. Thus, the 6-dB bandwidth is more relevant in this case. Despite the difference in their 6-dB bandwidths, the difference at 70 GHz is only 1 dB owing to the slow roll-off response of TFLN modulators [15]. Figure 3.2(b) indicates the measured RF V_π for both MZMs. The RF V_π is measured by biasing the MZM at maximum transmission and monitoring the output average optical power as a function of the amplitude (V_{pp}) of a 60 GHz single-tone signal. The V_π at 60 GHz is extracted from the normalized optical power versus the V_{pp}/V_π relationship, which follows a Bessel function formula. Then, we extrapolate the RF V_π from DC to 100 GHz using the MZMs' measured frequency response. The low-MHz V_π of the long and short MZMs are 1.25 V and 1.5 V, which increase to 3 V and 3.3 V at 70 GHz, respectively. The measured DC extinction ratio of the long MZM is 25 dB compared to 35 dB for the short MZM. Our system is limited by the driving swing and the bandwidth of the AWG; therefore, the difference in their V_π is more impactful than the difference in the bandwidth and extinction ratio.

3.2.1.2 Driver-less transmission results

Figure 3.3 presents the transmission performance achieved using the long and short MZMs. The BER versus symbol rate of PAM4 and PAM6 signals after 500 m transmission is given in Figure 3.3(a) with the summary in Table 3.1. The long MZM outperforms the short MZM throughout the considered symbol rates (100 to 150 Gbaud). Using the long MZM, we transmit 108 and 132 Gbaud PAM6 signals under the KP4-FEC threshold and the 3.8×10^{-3} HD-FEC BER threshold, which correspond to a net rate of 256 and 309 Gbps, respectively. Besides, we transmit 105 and 128 Gbaud PAM6 signals using the short MZM below the KP4-FEC and HD-FEC BER thresholds, corresponding to net rates of 250 and 300 Gbps. Thus, we successfully transmit net 300 Gbps with both MZMs and a practical HD-FEC with 500 mV_{pp} drive signal.

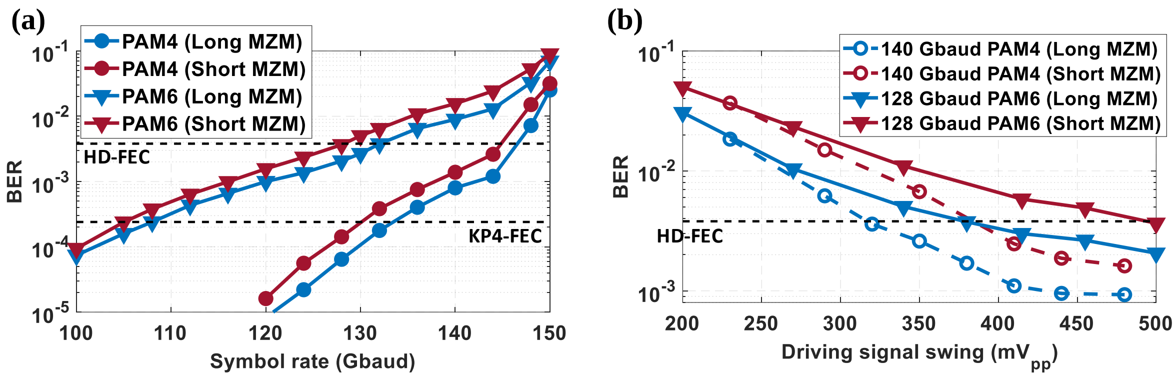

Figure 3.3. (a) The BER versus the symbol rate (ROP = 7 dBm). (b) The BER sensitivity to the driving voltage swing (ROP = 7 dBm).

Table 3.1. Summary of Net Bitrate Achieved after 500 m Transmission Using ~500 mV$_{pp}$ Drive Signals and FFE

FEC	**Short TFLN MZM**		**Long TFLN MZM**	
	Modulation format	Net rate (Gbps)	Modulation format	Net rate (Gbps)
KP4-FEC	105 Gbaud PAM6	250	108 Gbaud PAM6	256
	128 Gbaud PAM4	242	132 Gbaud PAM4	250
HD-FEC	128 Gbaud PAM6	300	132 Gbaud PAM6	309
	144 Gbaud PAM4	270	144 Gbaud PAM4	270
SD-FEC	132 Gbaud PAM8	332	136 Gbaud PAM8	342

Figure 3.3(b) shows the BER dependency on the driving signal swing for 140 Gbaud PAM4 and 128 Gbaud PAM6 signals using both long and short MZMs. Using the long MZM, we transmit 140 Gbaud PAM4 using an exceptionally low swing of 325 mV$_{pp}$ under the HD-FEC BER threshold, while a minimum of 400 mV$_{pp}$ is required for transmitting 128 Gbaud PAM6. The short MZM requires a higher swing to achieve the same BER because of its higher V_π. The smaller driving signal swing implies reducing the power consumption, which is extremely important for short-reach DCI solutions. CMOS can fulfill these low swing requirements, which supports TFLN as a platform for next-generation EO modulators.

The BER sensitivity to the ROP both in back-to-back (B2B) and after 500 m transmission is given in Figure 3.4(a). Compared to the long MZM, the short MZM exhibits a ~1 dB ROP penalty. This ROP penalty arises from the inherent difference in the modulation efficiency of

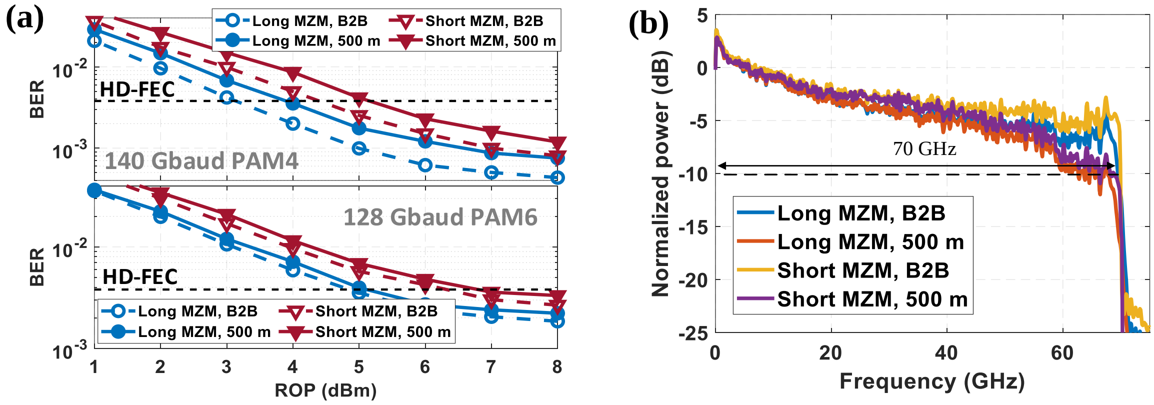

Figure 3.4. (a) The BER versus ROP at 140 Gbaud PAM4 and 128 Gbaud PAM6 in B2B and after 500 m transmission. (b) The received RF spectra of 140 Gbaud PAM4 signals.

the long and short MZM. Going from B2B to 500 m, the transmission penalty is more pronounced for the 140 Gbaud PAM4 cases because of the stronger CD-induced power fading. Figure 3.4(b) shows the received RF spectra of 140 Gbaud PAM4 signals. Compared to the short MZM, the long MZM has an extra 1 dB drop at 70 GHz because of the difference in their EO response. However, the ~5.5 dB drop at 70 GHz after transmission stems from the CD-induced power fading.

The swing limitations in our system dictate optimizing the PAPR to compromise the swing and nonlinearity constraints. Here we control the PAPR by clipping the digital signal before loading it to the AWG. Figure 3.5(a) shows the BER performance of 128 Gbaud PAM6 signals after 500 m transmission and the received signal RMS as a function of the PAPR of the digital signal loaded to the AWG. The clipping improves the signal swing, leading to an increase in extinction ratio. However, strong clipping distorts the signal and causes overall BER degradation. For our system, the optimum PAPR for 128 Gbaud PAM6 signal is ~ 7.8 dB and 7.25 dB for the long and short MZMs, respectively. Besides, the received signal RMS for the long MZM is considerably higher than that for the short MZM owing to the higher modulation depth in the former case.

The BER sensitivity to the number of FFE taps is given in Figure 3.5(b). Only 11 filter taps

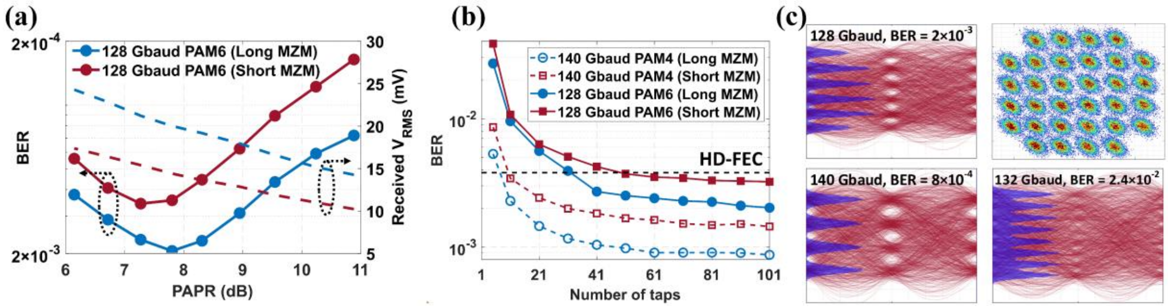

Figure 3.5. (a) The BER versus the PAPR of 128 Gbaud PAM6, and the corresponding received signal RMS on the right y axis. (b) The BER sensitivity to the number of FFE taps. (c) The eye diagrams after the FFE for 140 Gbaud PAM4, 128 Gbaud PAM6 (constellation diagram), and 132 Gbaud PAM8 after 500 m transmission using the long MZM.

are needed for transmitting 140 Gbaud PAM4 under the HD-FEC threshold, and 51 taps are required to reach the BER floor for both MZMs as the difference in the received frequency response is marginal (~1 dB). Figure 3.5(c) shows the generated eye diagrams of the equalized signals at different symbol rates and PAM formats after 500 m transmission using the long MZM. Interestingly, the generated constellation from the 128 Gbaud PAM6 signal shows elliptical noise distribution, highlighting the impact of the FFE-enhanced in-band noise [65].

To determine the attainable transmission rates, we considered PAM8 transmission adopting SD-FEC with an NGMI threshold of 0.8798 (code rate: 0.84) [83]. Here, we employ the NGMI as a metric instead of the traditional BER to ensure a fair comparison of the PAM8 transmission performance with previous work that utilized the same short TFLN MZM but with an RF driver [84]. Accordingly, we can quantize the penalty incurred by eliminating the RF driver in terms of the achievable transmission rate. Figure 3.6(a) shows the calculated NGMI after 500 m transmission. Using only linear equalization and 500 mV_{pp} driving signal, we transmit 136 Gbaud PAM8 using the long MZM well above the NGMI threshold, corresponding to a net rate of 342 Gbps. The short MZM enabled transmitting 132 Gbaud PAM8, which corresponds to a net rate of 332 Gbps. Figure 3.6(b) shows the ROP performance of 132 Gbaud PAM8 for both MZMs. Here, the short MZM exhibits a higher ROP penalty of ~ 2 dB, which stems from

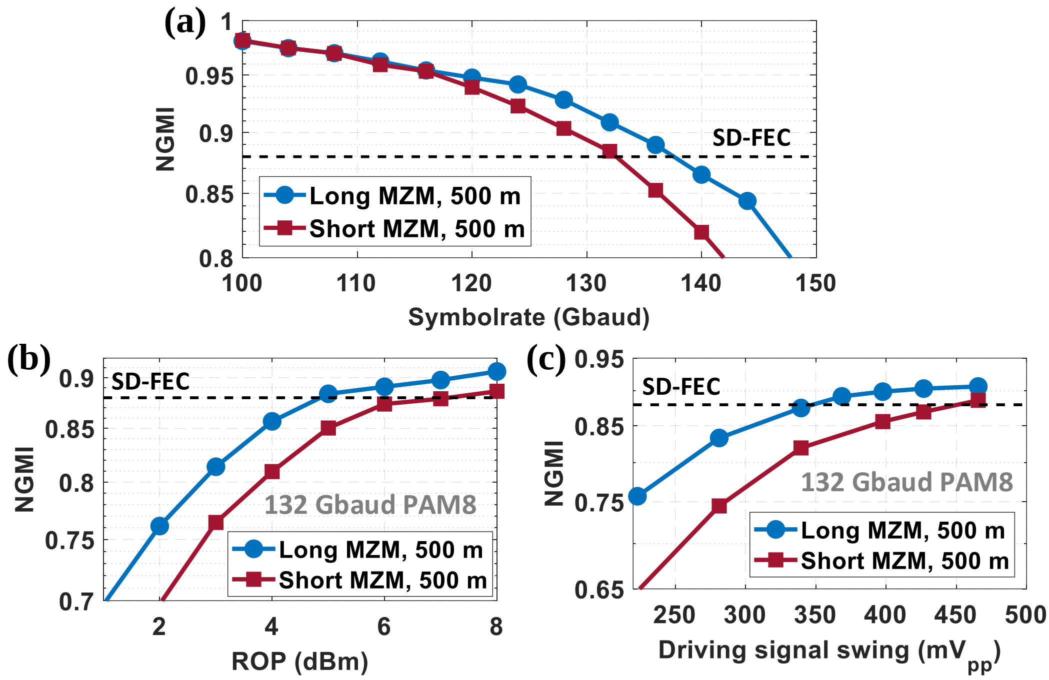

Figure 3.6. (a) NGMI versus symbol rate for PAM8 signals. (b) NGMI versus ROP and (c) NGMI sensitivity to the driving swing of 132 Gbaud PAM8.

the higher number of levels of PAM8 and the higher sensitivity to the ADC noise. Figure 3.6(c) shows the NGMI sensitivity to the driving signal swing, the difference in performance between the long and short MZMs is more pronounced in the PAM8 case. We transmit 132 Gbaud PAM8 over 500 m above the SD-FEC threshold with only 375 mV$_{pp}$ using the long MZM.

The differences in transmission performance between the long and short MZMs are mainly because of the difference in their V_π, given their high bandwidth and the AWG bandwidth limitations. Although the short MZM has higher bandwidth and extinction ratio, its higher V_π results in lower modulation depth, smaller signal swing at the receiver, and slightly worse overall performance. Thus, reducing the MZM V_π via increasing its length is advantageous in the presence of other sources of bandwidth limitations. The sensitivity of the performance to the driving swing scales with the PAM order because of the higher number of levels and the modest optical extinction ratio after modulation; thus, PAM4 is more suitable for such driver-less systems.

These results indicate the promise of 300 Gbps short-reach DCI links based on TFLN MZMs with reduced DSP complexity and low driving voltage requirements (below 500 mV_{pp}). Employing stronger DSP will not yield a performance improvement that justifies the added complexity; hence, we only considered simple linear equalization. In [84], we report the transmission results obtained using the short MZM and employing an RF driver, where we demonstrated the transmission of 132 Gbaud PAM6 signal over 500 m below the HD-FEC BER threshold, and 140 Gbaud PAM8 signal above the SD-FEC NGMI threshold using nonlinear processing at the transmitter and receiver, which respectively correspond to net rates of 309 and 352 Gbps. Those results are on par with what is achieved using the long MZM without the RF driver and only linear equalization. Comparing these values with the summary in Table 3.1 for the long MZM, we achieve the same performnace at the HD-FEC threshold and we exhibit less than 3% performance difference at the SD-FEC. This suggests that the driving signal swing improvement because of the RF driver is counteracted by the added noise, which degrades the RF signal quality and results in marginal improvement.

3.2.2 Net 400 Gbps/λ IMDD Transmission Using Single-DAC DSP-free Transmitter and C-band TFLN MZM [85]

The previous section showed the driver-less transmission performance of the TFLN MZMs, achieving a net data rate of 342 Gbps with only a marginal degradation compared to the case when an RF driver is employed. However, neither configuration was able to achieve the target net data rate of 400 Gbps, which is the next milestone for IMDD systems aiming for 4λ 1.6T interfaces. In this section, we propose and experimentally validate a driver-less transmitter architecture that significantly improves the performance and enables a net data rate of 400 Gbps/λ. However, it is important to note that this architecture comes with certain design limitations, which will be discussed towards the end of this section.

Increasing the system capacity of IMDD systems mandates either transmitting higher symbol rate signals or adopting higher pulse amplitude modulation (PAM) formats. The former choice requires a higher sampling rate (beyond 200 GSa/s) DAC that does not currently exist without interleaving, while the latter requires DAC and ADC with higher effective number of bits (ENoB). A solution adopted in academic research is to interleave multiple DAC channels operating between 90-128 GSa/s, yielding a higher sampling rate interleaved DAC assembly that can support data transmission at higher symbol rates.

In [32], the authors interleaved three DACs, referred to as digital-band-interleaved (DBI) DAC, to transmit 200 Gbaud probabilistically shaped (PS)-PAM16 (net 494.5 Gbps) over 120 m of SSMF with a C-band TFLN MZM above the 26% overhead SD-FEC NGMI threshold of 0.8456. Additionally, the authors in [86] used an analog multiplexer (AMUX) to multiplex 2 DAC channels, enabling the transmission of 162 Gbaud PS-PAM16 (net 420 Gbps) above the 0.857 NGMI threshold. We also report the transmission of 180 Gbaud PAM8 using a C-band TFLN MZM over 120 m using an interleaved 256 GSa/s DAC with the 20% overhead SD-FEC [31], as discussed in the next section.

The cost-effectiveness of IMDD systems favors single-DAC operation; however, achieving net 400 Gbps transmission using a single DAC channel has not yet been demonstrated. Figure 3.7 reviews the high-speed IMDD reports employing conventional PAM formats. In this work,

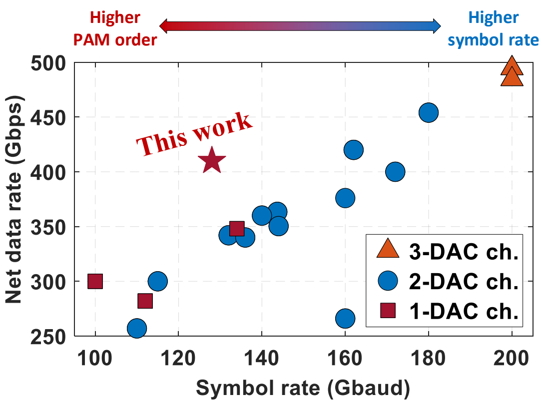

Figure 3.7. Summary of the IMDD demonstrations categorized based on the transmitter configuration.

we demonstrate the transmission of 128 Gbaud PAM16 under the 25% overhead SD-FEC BER threshold and 128 Gbaud PS-PAM16 below the 20% SD-FEC threshold using a C-band TFLN MZM driven directly with a single DAC (128 GSa/s, 800 mV_{pp} at 1 sps), which respectively correspond to net rates of 410 and 400 Gbps.

3.2.2.1 Experimental setup

A schematic of our experimental setup and the receiver DSP routine is given in Figure 3.8. The proposed architecture is to employ a single DAC at 1 sps without any DSP or signal conditioning at the transmitter. We employ a DSP-free transmitter; thus, we only create the PAM symbols and load them directly to the DAC (AWG: Keysight M8199A) without any DSP manipulation. We operate the AWG at 1 sps with neither pulse shaping nor frequency pre-emphasis filtering; this minimizes the PAPR of the signal and maximizes the driving signal swing (maximum of 800 mV_{pp}). The TFLN MZM is driven directly with the AWG output using a 67 GHz GSG probe. We use the long MZM from the previous section, which has has a 24(66) GHz 3-(6-) dB EO bandwidth with a low-MHz V_π of 1.25 V. The low V_π is a key enabler of the achieved driver-less transmission performance. The output of the MZM is transmitted over 120 m, which corresponds to 2 ps/nm dispersion and is equivalent to around 1 km in the O-band with the CWDM grid. The rest of the experimental setup follows the previous section. At the receiver, the signal is resampled to 2 sps (for symbol rates other than 128 Gbaud), and then processed with a polynomial nonlinear equalizer (PNLE), unless mentioned otherwise. PNLE

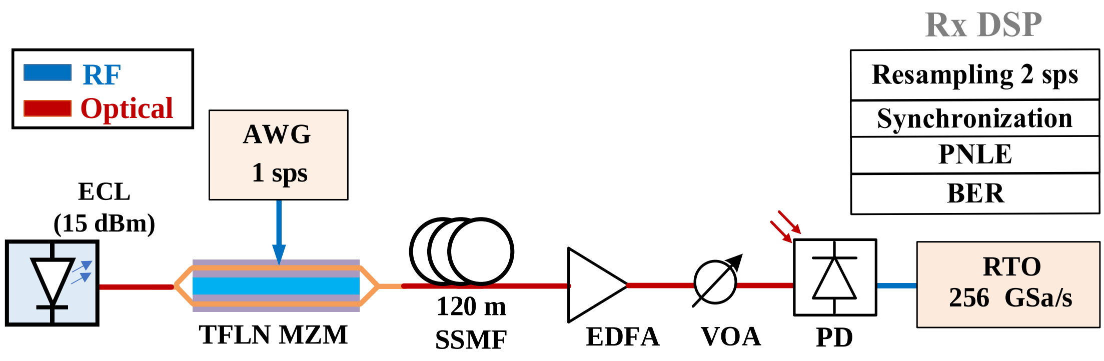

Figure 3.8. Experimental setup and receiver DSP blocks.

is a simplified form of the Volterra nonlinear equalizer (VNLE) that uses only the self-beating terms and yields a considerable reduction in computational complexity [87]. Finally, the BER is calculated from the equalized signal.

3.2.2.2 Standard PAM transmission performance

Figure 3.9 presents the transmission performance of the standard PAM formats employing a DSP-free transmitter. The BER versus the symbol rate is given in Figure 3.9(a), with the summary in Table 3.2. We sweep the symbol rate by changing the sampling rate of the AWG (100 to 128 GSa/s) while operating at 1 sps. With an 800 mV_{pp} driving swing, we transmit 128 Gbaud PAM16 at a BER of 3.4×10^{-2} under the 25% overhead SD-FEC threshold, which corresponds to a net rate of 410 Gbps. Besides, we transmit 108 Gbaud PAM8 below the 2.4×10^{-4} KP4-FEC BER threshold.

Figure 3.9(b) shows the BER sensitivity of 128 Gbaud PAM16 signal to the ROP with different receiver equalizers. We considered linear FFE, second order PNLE, and third order PNLE with/without maximum likelihood sequence detection (MLSD). The lengths of the equalizer kernels are indicated in the figure. PAM16 signaling is more sensitive to the nonlinearities stemming from the AWG, MZM transfer function, and bias point drifting. Thus, we observe a considerable improvement in the BER with third-order PNLE. MLSD improves

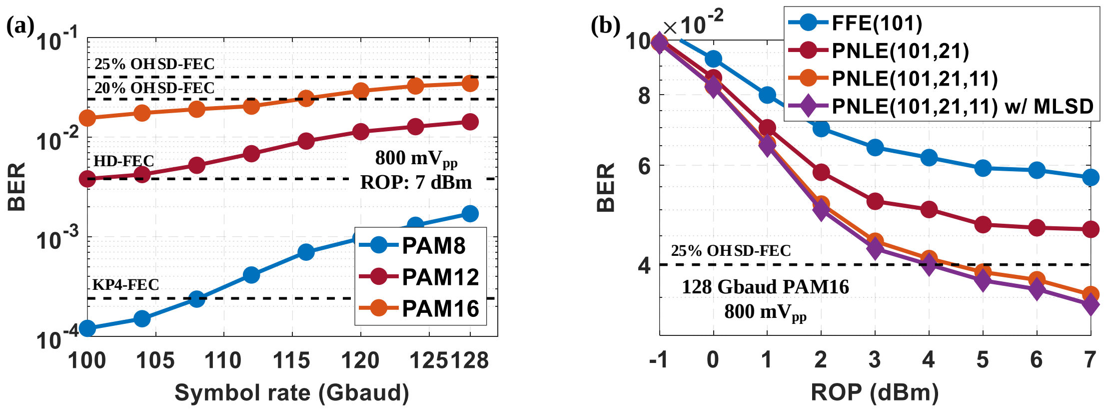

Figure 3.9. Summary of the standard PAM transmission performance. (a) BER versus the symbol rate. (b) BER sensitivity to the ROP with different receiver equalization schemes.

the BER marginally, which does not justify the added complexity. Therefore, we limited ourselves to third-order PNLE with 101 first order, 21 second order, and 11 third order beating terms; the further increase in the number of terms improves the BER negligibly. It is worth noting that the gain of employing third-order PNLE diminishes as we decrease the PAM order; however, we used it for processing all the data points in Figure 3.9 for consistency.

A major aspect of this work is operating without an RF driver, owing to the high modulation efficiency of TFLN. The BER sensitivity to the driving swing of the different PAM formats at 128 Gbaud is shown in Figure 3.10(a). The system is swing-limited, and the BER keeps improving with increasing the swing. We transmit 128 Gbaud PAM4 under the KP4-FEC threshold with only a 200 mV_{pp}. CMOS technology can readily support these swing requirements, which highlights the potential to discard transmitter RF driver. Dispensing the RF driver and the transmitter DSP (pulse shaping and pre-emphasis filtering) reduces the power consumption significantly, which is attractive for the short-reach DCI because of their stringent power constraints. Figure 3.10(b) shows the optical spectra of 128 Gbaud PAM16 signal with various driving swings. The optical signal is not limited in frequency and follows a sinc function rather than a rectangle due to the absence of pulse-shaping. The laser wavelength is set to 1565 nm to match the peak transmission of the grating couplers.

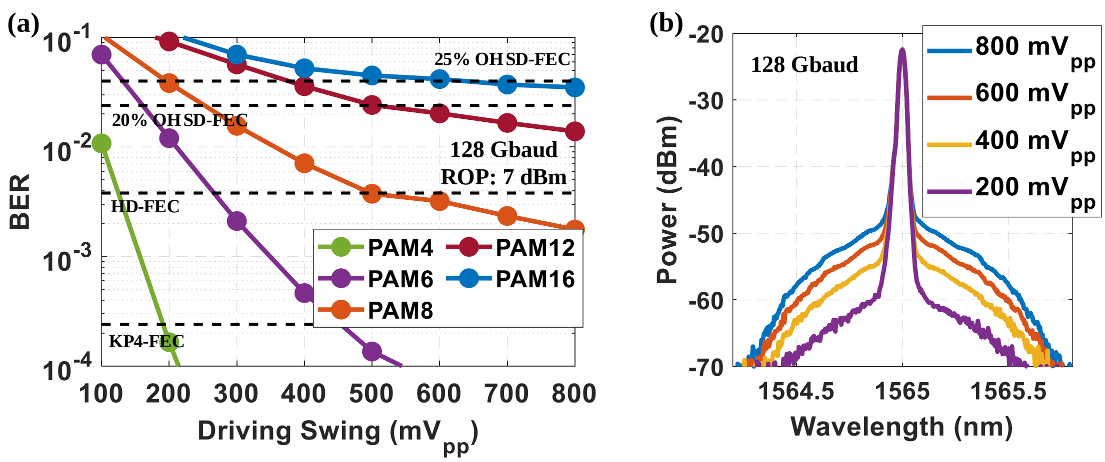

Figure 3.10. (a) BER sensitivity to the driving swing at 128 Gbaud for the standard PAM formats. (b) The optical spectra of 128 Gbaud PAM16 at different driving levels.

Table 3.2. Summary of Net Bitrates using the DSP-free transmitter architecture (at 1 sps, 800 mV$_{pp}$)

FEC BER threshold	FEC OH	Modulation format	Net rate (Gbps)
2.4×10^{-4}	5.8%	108 Gbaud PAM8	306
		128 Gbaud PAM6	302
3.8×10^{-3}	6.7%	128 Gbaud PAM8	360
2.4×10^{-2}	20%	128 Gbaud PS-PAM16	400
		128 Gbaud PAM12	373
4×10^{-2}	25%	128 Gbaud PAM16	410

3.2.2.3 PS-PAM transmission performance

Given the high SNR requirement for PAM16 transmission and its sensitivity to nonlinearities, this section focuses on PS-PAM16 transmission. PS offers more granular control over the transmitted signal source entropy (bits/symbol) at the expense of adding a DSP block (power consumption and latency) to the transmitter. We generate PS-PAM16 signals at different source entropies using the constant composition distribution matcher (CCDM) with a Maxwell-Boltzmann distribution. Figure 3.11(a) shows the BER versus the source entropy and the corresponding line rate for PS-PAM16 compared to standard PAM formats. Here, PAM8 (PAM16) corresponds to an entropy of 3 (4) bits/symbols. We transmit PS-PAM16 at a source

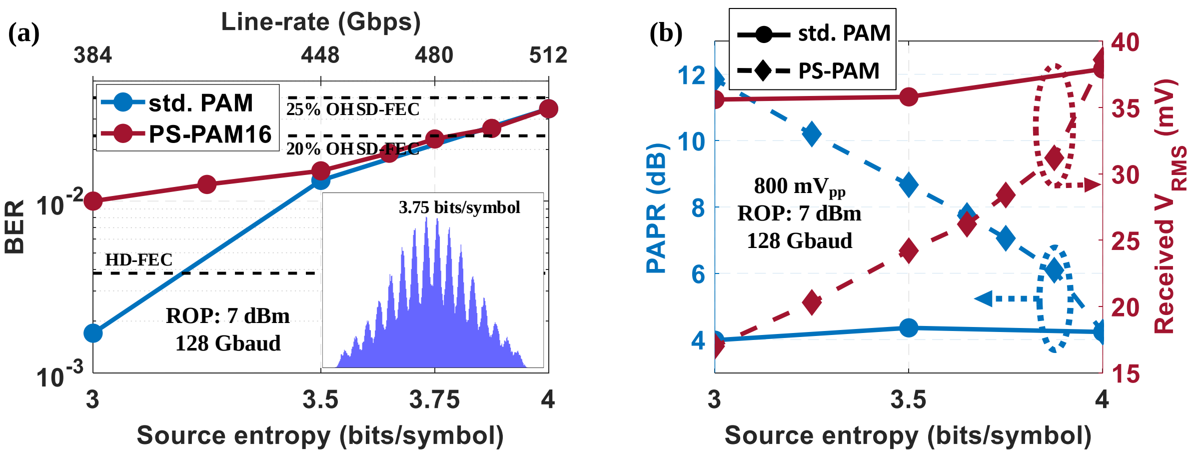

Figure 3.11. (a) BER versus the source entropy (line-rate) of PS-PAM16 and standard PAM at 128 Gbaud. The inset shows the histogram of PS-PAM16 (3.75 bits/symbol) after equalization. (b) The PAPR of the transmitted signal and RMS of the received signal versus the entropy.

entropy of 3.75 bits/symbol under the 2.4×10^{-2} BER threshold of the 20% overhead SD-FEC, corresponding to a net rate of 400 Gbps. Due to the higher number of inner levels, PS-PAM16 at an entropy of 3 bits/symbol is significantly worse than PAM8. Whereas both PAM-12 and PS-PAM16 show similar performance. However, our range of interest is primarily between 3.5 and 4.0 bits/symbol.

Figure 3.11(b) shows the PAPR of the transmitted PS-PAM and standard PAM signals before loading to the DAC and the corresponding received RMS swing as a function of the source entropy or PAM format. For standard PAM (Solid curves), the PAPR and the received RMS swing are approximately constant as we operate at 1 sps without any signal processing. However, PS increases in the transmitted signal PAPR, which reduces the DAC output swing and subsequently the received signal RMS leading to a degradation in performance.

The BER sensitivity to the ROP of 128 Gbaud PS-PAM16 (3.75 bits/symbol) is shown in Figure 3.12(c). Compared to PAM16, PS-PAM16 has a higher nonlinearity tolerance, as the edge symbols are sent with lower probabilities (inset of Figure 3.11(a)). Thus, the improvement incurred from employing third order PNLE compared to the second order PNLE is less pronounced for the PS-PAM16 case, compared to the PAM16 (Figure 3.9(b)). Interestingly, the BER keeps improving with the ROP; hence, a higher ROP is expected to improve the performance further.

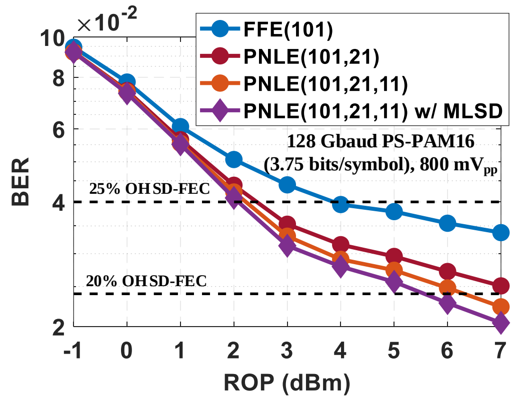

Figure 3.12. BER sensitivity to the ROP of 128 Gbaud PS-PAM16 (3.75 bits/symbol).

As mentioned earlier, the target application for this work is high-speed O-band IMDD transmission for intra-DCIs. In this context, we have investigated the impact of chromatic dispersion, represented by fiber length, on the transmission performance as depicted in Figure 3. Figure 3(a) presents the BER for different PAM formats at a symbol rate of 128 Gbaud after transmission over varying fiber lengths. There is a performance penalty moving from B2B to 500 transmission. This degradation occurs despite the fixed ROP. Figure 3(b) shows the received RF spectra of 128 Gbaud PAM16 signals. For a transmission distance of 500 m (equivalent to 8.5 ps/nm dispersion), there is approximately a 3 dB drop in the frequency response at 70 GHz. While this marginally degrades the BER performance, it highlights the impact of chromatic dispersion-induced power fading. Figure 3(c) provides the simulated transfer function of a dispersive IMDD system operating at 1565 nm (dispersion coefficient = 17 ps/nm/km). The simulated transfer function demonstrates how the power fading induced by chromatic dispersion limits the transmission reach of high symbol rate systems.

3.2.2.4 Discussion

This work demonstrates the IMDD transmission of net 400 Gbps on a single carrier using a 800 mV_{pp} driving signal from a single DAC channel (128 GSa/s) without external RF amplification, with two different schemes: (1) DSP-free transmitter supporting 128 Gbaud PAM16 with the 25% overhead SD-FEC; and (2) employing PS-PAM16 at 128 Gbaud with

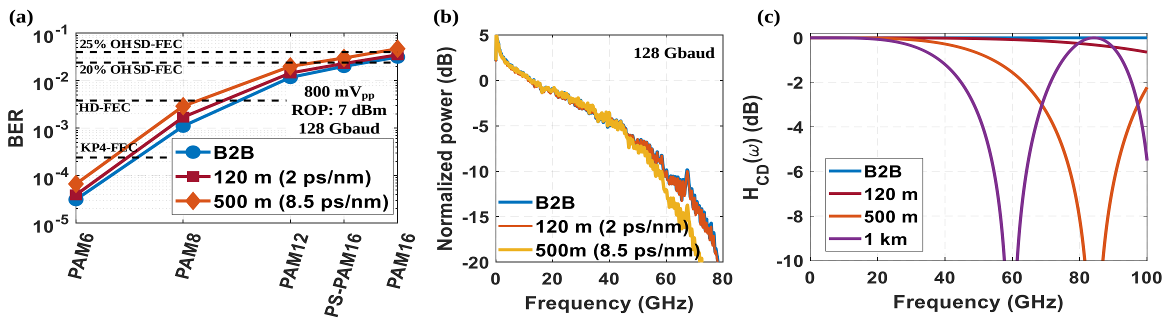

Figure 3.13. (a) The BER versus the PAM format for different transmission distances at 128 Gbaud. (b) The received electrical RF spectra after transmission over different fiber lengths. (c) The transfer function of a dispersive (chirp-free) IMDD system.

the 20% overhead SD-FEC. Therefore, the decisive parameters are the power consumption and induced latency of the PS module versus employing a lower code rate FEC.

The proposed architecture indeed introduces the challenge of employing high-order PAM formats, such as PAM16. It is true that the industry has largely supported PAM4 due to its simpler architecture and lower SNR requirements. In comparison, PAM16 demands more than 9 dB higher SNR than PAM4 to achieve the same BER, equivalent to an 8-fold increase in signal power at the same noise level. This level of power increase is impractical, making PAM16 less likely to be adopted as an industry standard.

However, despite the limitations associated with PAM16, the proposed architecture still exhibits significant improvements in achieved BER for lower-order PAM formats. When comparing the results in Table 3.1 and Table 3.2, a notable improvement of more than 20% in transmission capacity is observed at the KP4-FEC threshold, which is already adopted in commercial products. Therefore, while PAM16 may not be practical, the proposed architecture remains effective and enhances performance for different PAM formats by eliminating the noise introduced by the RF driver.

These results suggest that DSP-free transmitters combined with the TFLN platform low V_π can operate without an RF driver, without incurring any performance penalties. This finding highlights the potential benefits of the proposed architecture in terms of simplifying the transmitter design and improving transmission performance for lower-order PAM formats.

3.3 TFLN MZMs and Next-Generation of DACs [31]

In the previous section, we demonstrated the potential for achieving net 400 Gbps/λ transmission using a single 128 GSa/s DAC and PAM16 modulation. However, the high SNR requirements of PAM16 make it impractical for the industry. In this section, we aim to explore the performance improvements that can be achieved by utilizing the next generation of commercial DACs that integrate an interleaver to multiplex two 128 GSa/s DACs into a single 256 GSa/s DAC, while maintaining the required bandwidth. Additionally, our investigation aims to determine whether the performance limitations observed in the previous sections were primarily due to the bandwidth limitations of the TFLN modulator or the DAC.

Recently, Ciena made an exciting announcement regarding the development of a 1.6 Tbps/λ coherent solution [51]. This product utilizes ASIC engines that are fabricated using the highly advanced 3 nm process node and support 200 Gbaud operation. This development highlights an industry trend that prioritizes expanding the operational bandwidth of transmission systems rather than solely focusing on increasing the modulation order. Furthermore, the announcement suggests that the industry has made significant progress in developing and deploying 100 GHz RF components, including DACs, RF drivers, TIAs, and ADCs. These components are essential for achieving high-performance, high-speed communication systems.

The objective of this work is to assess the effectiveness of employing the latest generation of DACs and RF drivers with the TFLN platform. Specifically, the study utilizes Keysight's M8199B prototype AWG with both O-band and C-band TFLN MZMs. The AWG works at 256 GSa/s with an integrated interleaver and RF driver, which supports operating beyond 85 GHz with a sufficiently high driving swing for the TFLN MZMs. Using this transmitter configuration, we demonstrate the transmission of 180 Gbaud PAM8 with the C-band MZM and 172 Gbaud PS-PAM8 with the O-band MZM under the 20% overhead SD-FEC BER threshold, achieving net data rates of 450 and 400 Gbps, respectively. This is the first report of an O-band IMDD system supporting net 400 Gbps/λ operation, an important milestone based on the Ethernet roadmap. Figure 3.14 provides a summary of recent reports on high-speed IMDD systems, categorized based on their operating wavelength with the modulator platform indicated. While IMDD transmission at high speeds is primarily deployed in the O-band, the majority of the demonstrations employ C-band devices. This preference for C-band devices can be attributed to several factors. Firstly, product development in the C-band has proven to be more efficient and mature compared to the O-band, resulting in a wider range of readily available components and technologies for achieving high-speed transmission. Additionally, the C-band market for coherent transmission is larger, further contributing to its prominence in these demonstrations.

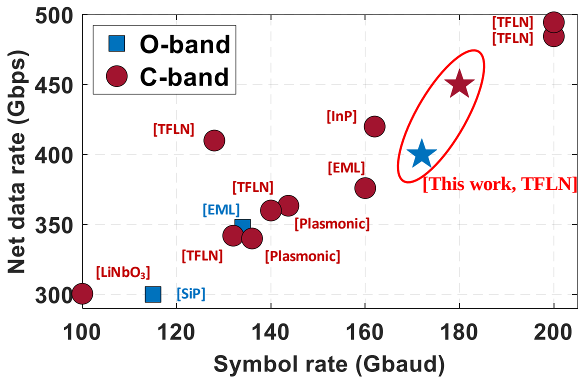

Figure 3.14. Summary of the high-speed IMDD demonstrations.

3.3.1 Transmission experiment

In this work, we employ C-band and O-band MZMs with different designs and specifications as shown in Figure 3.15. The C-band MZM is the 23 mm MZM employed in the previous sections. It has a fiber-to-fiber insertion loss (IL) of 12 dB at peak transmission (including grating couplers loss) and a DC optical extinction ratio of more than 26 dB. The O-band MZM has 18 mm electrodes with nearly 50 Ω on-chip termination and is connected via edge couplers. Unfortunately, due to a fabrication error, the O-band MZM has a fiber-to-fiber IL of 24 dB with a modest DC optical ER of 20 dB. However, this error does not affect the MZM's RF characteristics.

The C-band MZM has a 24 (66) GHz 3-(6-) dB bandwidth, while the O-band MZM has a 3-dB bandwidth of more than 70 GHz, as shown in Figure 3.15(a). The RF V_π is measured at

20 GHz and extrapolated based on the MZM's frequency response, as illustrated in Figure 3.15(b). The low-MHz V_π of the C-band and O-band MZMs are respectively 1.25 V and 1.7 V, which increase to 3.3 V and 2.9 V at 90 GHz.

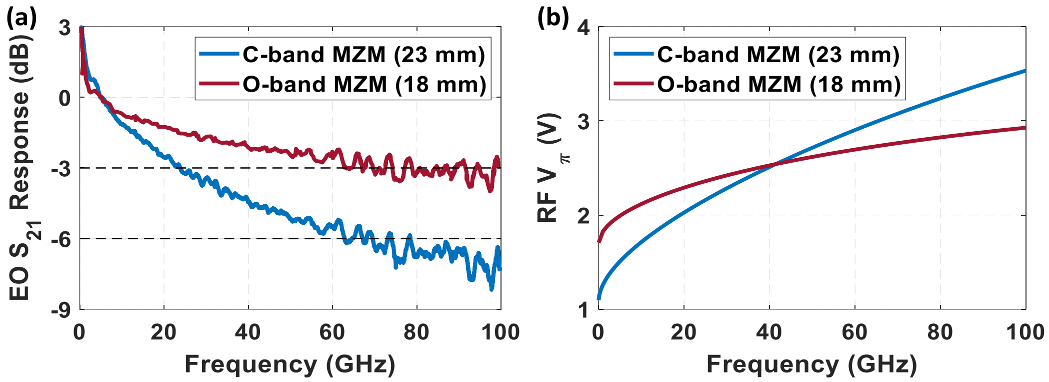

Figure 3.15. The TFLN MZMs characteristics: (a) the electro-optic (EO) response, and (b) the RF V_π.

3.3.1.1 C-band transmission performance

Figure 3.16 depicts the experimental setup and DSP routine employed in the C-band transmission experiment, which follows the conventional IMDD architecture described in section 3.2.1.1. The main difference in the transmitter DSP stack lies in including a nonlinear (NL) compensation step. This step involves pre-distorting the symbols using a nonlinear lookup table with a 3-symbol memory length [88]. In addition, the digital pre-emphasis filter, shown in the inset of Figure 3.16, compensates for the frequency response of the AWG (DAC and internal driver) and 20 cm of 1 mm connectorized RF cable. The transmitter RF chain has a 10 dB drop at 84 GHz, which enables operating beyond 160 Gbaud. The other difference in the

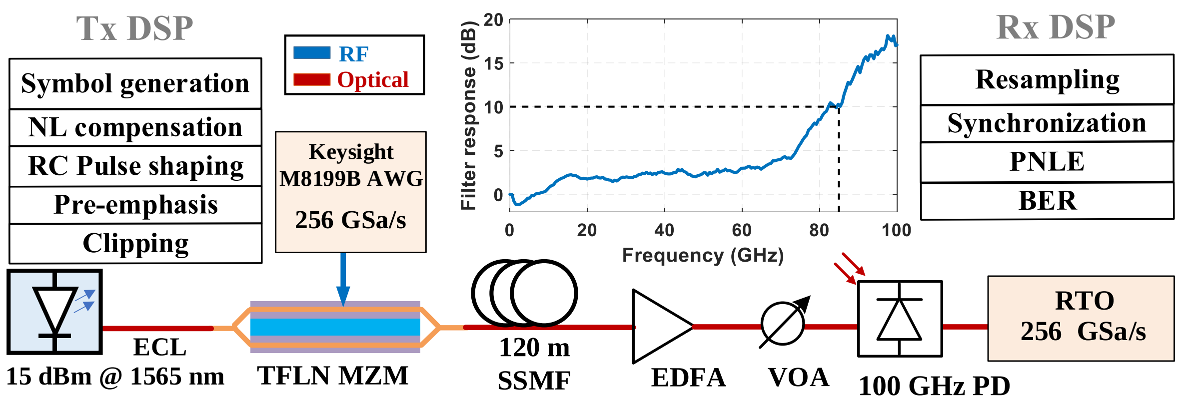

Figure 3.16. The C-band experimental setup and DSP routines. The inset shows the pre-emphasis filter.

experimental setup is that we upgraded the receiver hardware with a 100 GHz PD to alleviate the bandwidth limitations at the receiver.

The C-band transmission performance is summarized in Figure 3.17 and Table 3.3. Figure 3.17(a) shows the BER versus the symbol rate for the different PAM formats at 7 dBm ROP. The PAM6 symbols are derived from the standard cross 32QAM constellation with a pseudo-Gray bit mapping, which has a gray mapping penalty of 1.1667. We transmit 164 Gbaud PAM4 and 172 Gbaud PAM6 under the KP4-FEC and the 6.7% overhead HD-FEC thresholds, which corresponds to net 310 and 402 Gbps, respectively. To our knowledge, this is the first demonstration of a net data rate of 400 Gbps employing a standard PAM format at the 6.7% HD-FEC threshold, which has significant implications for power consumption and latency. Additionally, we demonstrate the transmission of 180 Gbaud PAM8 under the 2.4×10^{-2} 20% overhead SD-FEC BER threshold corresponding to a net data rate of 450 Gbps, which offers 12.5% margin for 400 Gbps/λ operation.

Figure 3.17(b) shows the BER versus the driving swing into the MZM. The AWG has an internal driver capable of providing up to 2.5 V_{pp} single-ended output; however, the digital pre-emphasis filter and the high PAPR reduce the actual output driving swing. The reported values are measured using the electrical head of a 100 GHz digital communication analyzer (DCA).

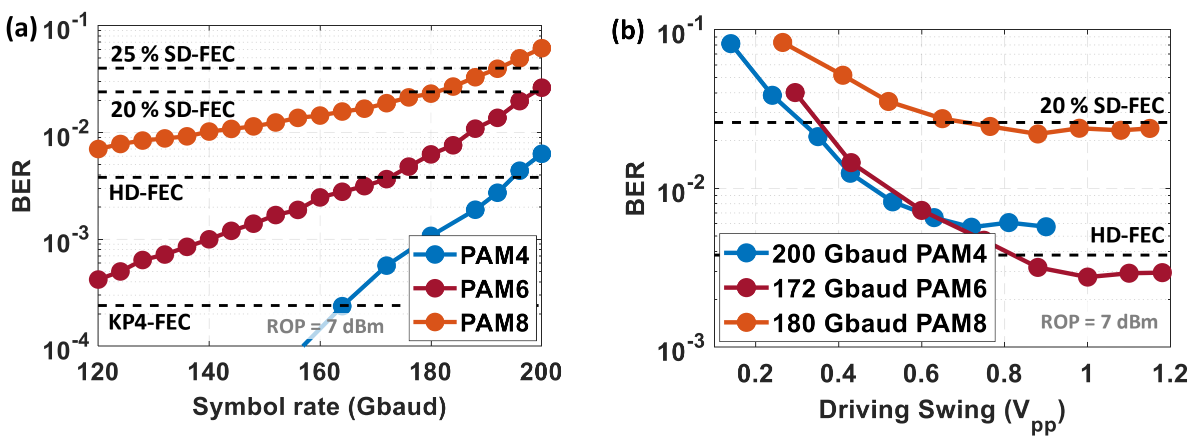

Figure 3.17. The C-band transmission performance. (a) The BER versus the symbol rate. (b) The BER versus the driving swing after digital pre-emphasis.

Our measurements demonstrate that a driving swing of only 1 V_{pp} is sufficient for achieving the reported performance, which is attributed to the low V_π of the TFLN MZM. This relaxes the requirements on the driver swing, letting the designers focus more on improving the bandwidth of the modulators.

Figure 3.18(a) shows the BER sensitivity to the ROP of 172 Gbaud PAM6 and 180 Gbaud PAM8 using a linear feed-forward equalizer, and second-order PNLE to assess the linearity of the received signal. The BER reaches the error floor at ROP of 5 dB. Although PAM8 suffers more from nonlinearity, the gain for PAM6 is higher because of PAM8's higher SNR requirement, and the lengths of the equalizer kernels are indicated in the figure. Figure 3.18(b) shows the eye diagrams of the RF signal before the MZM and after processing at the receiver with PNLE. The RF signal eye diagrams reveal that the nonlinearity in the signal stems from the nonlinear transfer function of the AWG internal driver, whereas the eye-opening decreases with the increases in signal level.

The impact of chromatic dispersion is illustrated in Figure 3.19(a) by transmitting the signal over different fiber lengths. The power fading observed for 500 m (8.5 ps/nm) transmission at 80 GHz is due to chromatic dispersion, which imposes a fundamental limit on the reach of high symbol rate IMDD systems. Figure 3.19(b) shows the optical spectra of 200 Gbaud PAM4

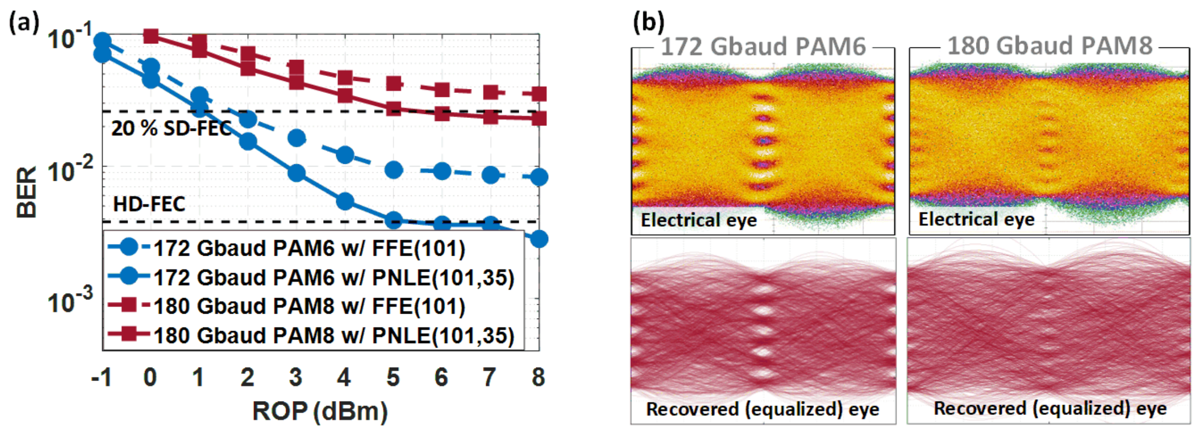

Figure 3.18. (a) The BER versus the ROP. (b) The eye diagrams of the AWG output and the corresponding equalized signals.

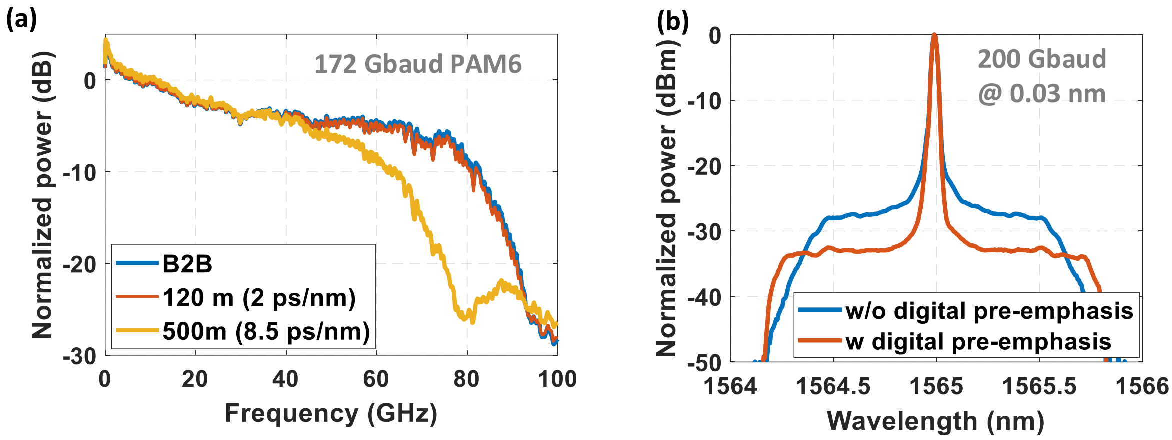

Figure 3.19. (a) The received RF spectra of 172 Gbaud PAM6 at different dispersion levels. (b) The optical spectra after the MZM of 200 Gbaud PAM4 with and without digital pre-emphasis.

signals after the MZM with and without digital pre-emphasis. The difference in signal power between the two spectra arises from the reduction in driving swing after pre-emphasis. Nonetheless, the digital pre-emphasis is essential for transmitting high symbol rate signals beyond 150 Gbaud.

3.3.1.2 O-band transmission performance

Figure 3.20 shows the modified experimental setup for O-band operation. To operate in the O-band, we utilize an 18 dBm DFB laser at 1310 nm, which is near the zero dispersion wavelength and allows for transmission up to 10 km. Due to fabrication error, the MZM IL is fairly high at 24 dB, so we use a 2-stage PDFA with a noise figure of 6.5 dB to amplify the signal to 7 dBm. Moreover, the additional noise introduced by the PDFA and the lower ER of the O-band MZM result in inferior overall performance compared to the C-band MZM.

In Figure 3.21, we present a summary of the O-band transmission performance, which is

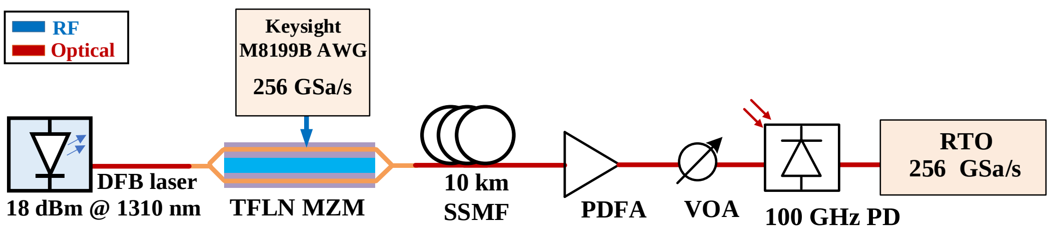

Figure 3.20. Modified setup for the O-band transmission experiment.

summarized by Table 3.3. Figure 3.21(a) shows the impact of symbol rate and PAM order on the BER. We transmit 170 Gbaud PAM8 signals under the 4×10^{-2} 25% overhead SD-FEC BER threshold, achieving a net rate of 408 Gbps. However, achieving a net rate of 400 Gbps under the 20% SD-FEC threshold with standard PAM modulation is not feasible. Therefore, we adopt the PS-PAM8 format and optimize the source entropy to achieve a net rate of 400 Gbps under the 20% SD-FEC BER threshold, as depicted in Figure 3.21(b). The PS-PAM8 signals are generated using a constant composition distribution matcher (CCDM) with a Maxwell–Boltzmann distribution [89]. The PS format improve the performance by leveraging the trade-off between bandwidth limitations and SNR requirements, offering a finer spectral efficiency granularity. With PS-PAM8, we transmit 172 Gbaud at a source entropy of 2.79 bits/symbol under the 20% SD-FEC BER threshold, resulting in a net rate of 400 Gbps. This is the first demonstration of net 400 Gbps transmission in the O-band over a distance of 10 km.

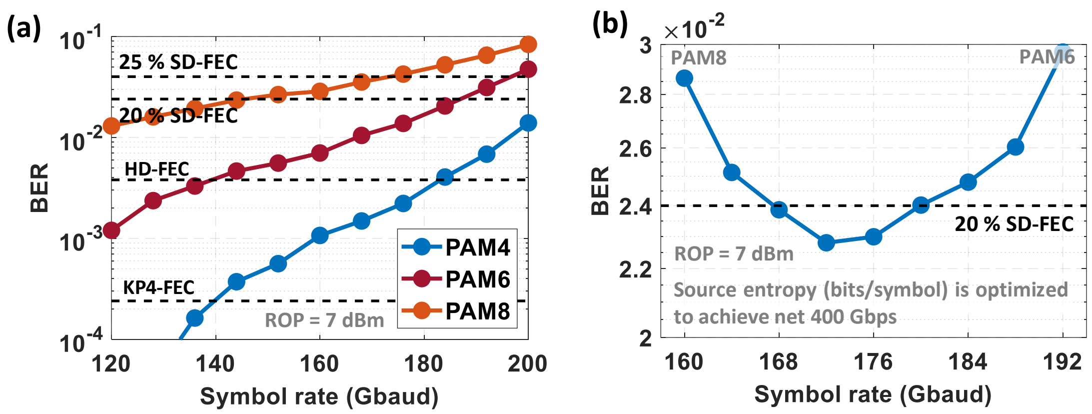

Figure 3.21. The O-band transmission performance. (a) The BER versus the symbol rate. (b) The BER versus the symbol rate of PS-PAM8 with optimized entropies to achieve net 400 Gbps assuming 20% overhead.

Table 3.3. Summary of Net Bitrate Achieved Using the TFLN MZMs with the Next-Generation of DACs

FEC	Overhead	C-band MZM		O-band MZM	
		Format	Net rate (Gbps)	Format	Net rate (Gbps)
KP4-FEC	5.4 %	164 Gbaud PAM4	310	136 Gbaud PAM4	258
HD-FEC	6.7 %	172 Gbaud PAM6	402	176 Gbaud PAM4	330
SD-FEC	20 %	180 Gbaud PAM8	450	172 Gbaud PS-PAM8	400
SD-FEC	25 %	192 Gbaud PAM8	460	170 Gbaud PAM8	408

3.3.2 Discussion

This work demonstrates the transmission of net 400 Gbps in the O-band over a distance of 10 km. However, it may be premature to consider 4λ×400 Gbps for 1.6 Tbps solutions over a range of 2 to 10 km. Currently, 800 Gbps IMDD solutions rely on CWDM with either 4λ×200 Gbps or 8λ×100 Gbps and are standardized for a reach of up to 2 km. 1.6 Tbps can be achieved in different configurations, including 16λ×100 G, 8λ×200 G, and 4λ×400 G. The 4λ approach is preferred due to its simpler architecture and lower device count, but it requires a high symbol rate that is not feasible at the edge channels of the CWDM grid. One solution is to modify the WDM grid to concatenate the 4λ in smaller bandwidth near the zero dispersion wavelength, but this is challenging due to channel nonlinearities and four-wave mixing (FWM). Another option is to deploy four parallel single-mode fibers (PSM), each operating at the zero dispersion wavelength to avoid dispersion and FWM. Yet, transmitting four fibers over 10 km is not cost-effective. Therefore, efforts are exerted to optimize the WDM grid for such high symbol rate systems and possible ways to mitigitate FWM. This is still a question that requires significant joint efforts from both academia and the industry to address.

3.4 Driver-Less SiP Transmitters [90]

Despite the impressive transmission performance achieved with the TFLN MZMs as discussed in the previous sections, SiP MZMs still dominate most of the market because of their rigid supply chain, low fabrication costs, and scalable production with very high yield. In addition, the performance attained with SiP MZMs has proven to be satisfactory for current and previous Ethernet speeds(i.e., 100 Gbps/λ and 200 Gbps/λ). These factors contribute to the continued prevalence and adoption of SiP MZMs in the industry. Moreover, the advancement on the electronics side is pushing the limits of what can be achieved with SiP. Previously, we demonstrated the transmission of net 300 Gbps/λ over 2km in the O-band using a single-segment SiP MZM and conventional electronic equalization [91]. In [92], the authors reported a three-segment SiP MZM with 67 GHz of bandwidth that enable transmitting 120 Gbaud PAM8 with a net rate of 336.4 Gbps; however, they used a coherent receiver for this work rather than a single PD with direct detection.

In this section, we assess the impact of removing the RF driver from the transmitter configuration, following a similar approach as with TFLN-based systems. However, dispensing the power-hungry RF driver from the SiP-based transmission systems is more challenging because of the high driving voltage requirements. In [93], they demonstrate the transmission 45 Gbps PAM4 without RF amplification using silicon dual-drive TW-MZM and 2 V_{pp} driving signals at an energy consumption per bit (E_b) of 611 fJ/bit. Additionally, the back-to-back transmission of 30 Gbps PAM4 is achieved using a dual-ring resonator modulator and two 1 V_{pp} driving signals in a driver-less scenario [94].

In a joint effort, IBM, CMC, AMF, and McGill University worked jointly to include IBM polymer photonic interface into AMF's SiP process flow [95] and to package and characterize a SiP O-band MZM co-designed by McGill and CMC. The description of the packaging methodology is given in [90]; however, here we will focus on the impact of packaging on the transmission performance and the penalty incurred from driver-less transmission.

3.4.1 Modulator characterization and packaging

The SiP chip is fabricated at AMF with a CMOS compatible process flow [96]. A detailed description of the design procedure of the travelling-wave (TW) MZM and the structure schematic are presented in [97]. It has a 4 mm phase-shifter at a fill factor of 85%, and it is terminated on-chip with a 50 Ω highly doped Si resistor. The TW electrodes are designed such that a good velocity matching between the optical signal and the RF signal is established at a characteristic impedance of 50 Ω. The measured DC V_{π} is 5 V at 0 V reverse bias, corresponding to an inverse phase-shifting efficiency ($V_\pi L$) of 2 V.cm. The MZM PN junctions are designed for series push-pull (SPP) driving, which reduces the equivalent capacitance of the two diodes and improves its bandwidth. Moreover, SPP requires a single RF signal to drive the MZM and a single DC signal for reverse biasing, which eases the packaging. The MZM arms are balanced, and a thermo-optic (TO) heater is used to set the bias point of the modulator.

The MZM is optically connected via the IBM adiabatic coupler implemented by AMF [96]. The measured fiber-to-fiber insertion loss (IL) at maximum transmission is 16.5 dB. The IL breakdown is as follows: 0.5 dB from the connectors, 9.2 dB coupling loss (4.6 dB per facet), 2 dB routing losses, and 4.8 dB modulator propagation loss.

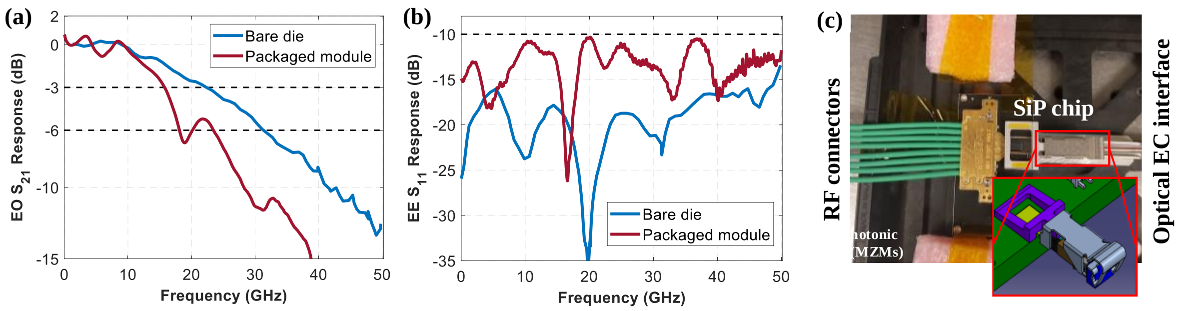

Figure 3.22. (a) The electro-optic S21 response of the module, and (b) its electrical S11 response at 0 V reverse bias. (c) The packaged SiP die onto the test board for high-speed transmission testing.

Figure 3.22(a) shows the electro-optic frequency response of the MZM as a bare die and after packaging at 0 V reverse bias. The packaged module has a 3-dB bandwidth of 16 GHz compared to 22.5 GHz at the die level. Figure 3.22(b) shows the S_{11} electrical response at 0 V reverse bias. The return loss increased by almost 6 dB; however, it is still under -10 dB up to 50 GHz. The deterioration in the frequency response is mainly coming from the RF wirebonding and the PCB routing.

3.4.2 Experimental setup

Figure 3.23 shows the experimental setup and the DSP blocks used at the transmitter and the receiver. In order to align with the low-cost application scenario of SiP MZMs, the

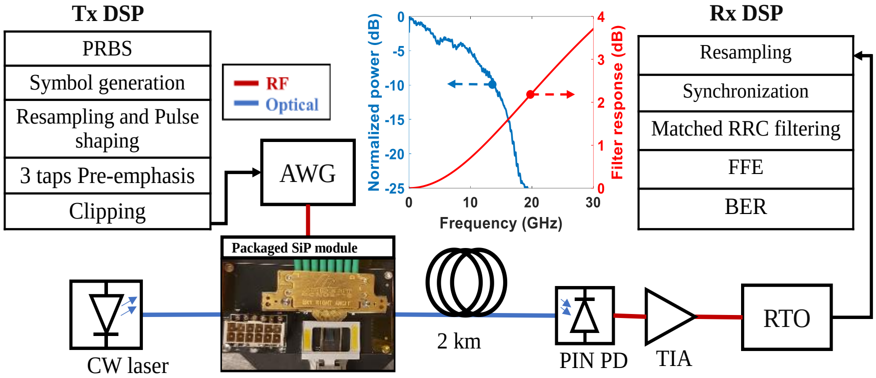

Figure 3.23. (a) Experimental setupand DSP blocks. The inset shows the received RF spectrum (blue) at 28 Gbaud and the 3 taps pre-emphasis filter (red).

experimental setup and the DSP stack are significantly simplified compared to those used in the TFLN experiments. At the transmitter, a pseudorandom binary sequence (PRBS) is mapped to PAM4, then upsampled to 2 samples per symbol for pulse shaping. We employ a root-raised cosine (RRC) filter instead of a raised cosine (RC) filter, as RRC filtering yields lower PAPR. The reduction of PAPR without signal clipping improves the performance because of the signal swing limitations as detailed in the following section. The RRC filter roll-off factor is optimized empirically for each symbol rate to utilize the entire bandwidth of the system. To pre-compensate the frequency response of the packaged module, we employ a 3 taps pre-emphasis digital filter as depicted in the inset of Figure 3.23. The weights of the 3 taps are optimized empirically. The signal is then clipped to further reduce the PAPR before loading it to the Keysight M8199A AWG for driving the module.

Optically, the SiP modulator is fed by a 13 dBm O-band laser at 1310 nm. The MZM is biased near the quadrature point using the thermo-optic phase shifter. It is unnecessary to operate exactly at the quad point because of the small swing of the driving signal that alleviates the linearity constraints; hence, we found that the optimum bias point is -2.5 dB from the max. The modulated optical signal is transmitted through 2 km of SSMF, which is then detected by a PIN photodiode followed by a TIA. Eventually, Keysight real-time oscilloscope captures the

TIA's RF output. The receiver DSP incorporates a matched RRC filter and feed-forward equalizer (FFE). For driver-less operation, we employ a Discovery Semiconductors DSC-R401HG optical receiver module that has a 22 GHz bandwidth and -15 dBm optical sensitivity.

For completeness and comparison, we tested the packaged MZM using the SHF 806 RF driver that has a 26 dB gain and 42 GHz 3-dB bandwidth. Hence, we replaced the 22 GHz PIN/TIA module with the Picometrix PT-40D/8XLMD PIN/TIA module, because it has a higher bandwidth of 33 GHz and -11 dBm optical sensitivity.

3.4.3 Driver-less transmission performance

In this section, we evaluate the performance of the packaged MZM driven directly by the AWG without RF or optical amplification over 2 km of SSMF. The AWG has a maximum output signal swing of 830 mV_{pp}. Thus, the performance reported in this section is limited by the signal swing, not the bandwidth of the electro-optic components. Figure 3.24(a) depicts the BER performance versus symbol rate using 7 and 31 taps FFE. We transmit 28 Gbaud PAM4 over 2 km of SSMF in the O-band using only 7 taps FFE at a BER of 1×10^{-4} far below the KP4-FEC threshold, corresponding to a net data rate of 53 Gbps. The received normalized electrical spectrum at 28 Gbaud is shown in the inset of Figure 3.23. In addition, 31 FFE taps are sufficient to transmit 36 Gbaud (67 Gbps net rate) below the 3.8×10^{-3} HD-FEC BER threshold. We also transmit 50 Gbaud on–off keying (OOK) signal under the HD-FEC threshold.

Due to the driving signal swing limitations, we clipped the transmitted signal extensively to limit the signal PAPR. Lower PAPR leads to a higher average voltage swing driving the MZM; however, clipping increases the nonlinearity in the signal. Figure 3.24 (b) presents a 2D map of the achieved BER at different symbol rates and PAPR levels using 7 taps FFE. The PAPR is swept through varying the clipping ratio. There is an optimum PAPR value that yields the lowest BER at each symbol rate. As the symbol rate increases, more clipping is needed to

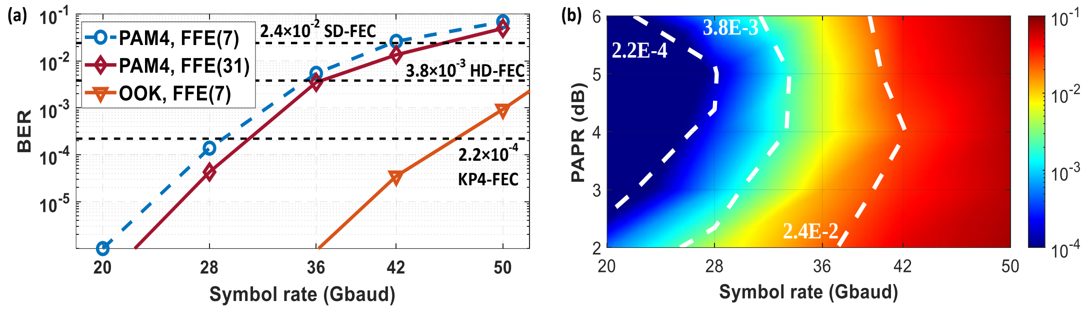

Figure 3.24. The driver-less operation results after 2 km of SSMF: (a) the BER versus symbol rate, (b) the 2D map of the achieved BER using 7 taps FFE as a function of the symbol rate and PAPR (830 mV$_{pp}$ drive signal).

reduce the PAPR and to compensate for the MZM's electro-optic bandwidth.

Figure 3.25(a) shows the BER sensitivity to the AWG driving signal peak-to-peak voltage at 28 Gbaud and PAPR of 4.5 dB. Increasing the swing improves the BER performance; nevertheless, 750 mV$_{pp}$ and 500 mV$_{pp}$ are sufficient for a BER below the KP4-FEC and HD-FEC thresholds. The energy consumption per bit for SPP MZMs, excluding the TO heater, is calculated according to $E_b = V_{rms}^2/(RB)$, where V_{rms} is calculated by integrating the transmitted waveform, R is the termination (50 Ω), and B is the gross bit rate [98]. Thanks to the employed DSP, we achieve the transmission of net 53 Gbps at E_b of 8 fJ/bit. This is the energy consumed by the modulator only, whereas the DSP pushes the power consumption from the modulator to the electronics side.

Figure 3.25(b) shows the BER dependency on the RRC filter roll-off factor at 28 Gbaud; the corresponding signal bandwidth is shown on the top axis. Increasing the roll-off factor is

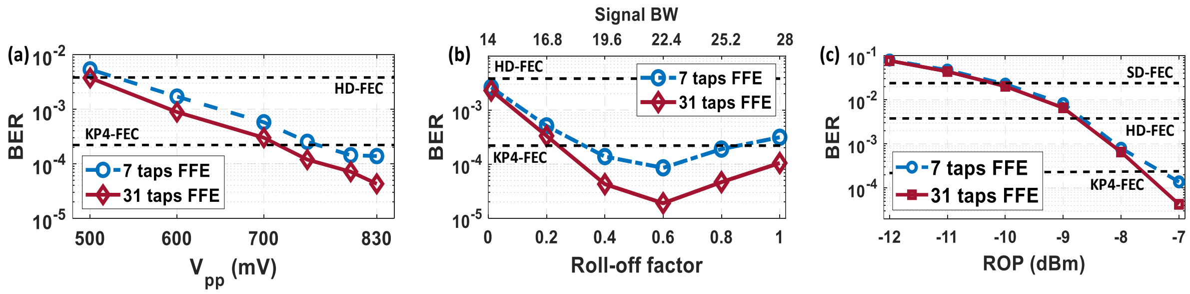

Figure 3.25. (a) the BER for 28 Gbaud PAM4 signal versus the driving voltage, (b) the BER versus the RRC roll-off factor (top X axis: signal bandwidth) at 28 Gbaud, and (c) the BER at 28 Gbaud versus the ROP.

another way of reducing the PAPR and increasing the average signal swing driving the MZM. However, the system bandwidth is limited by the packaged MZM electro-optic bandwidth and the 22 GHz PIN/TIA module. The BER dependency on the received optical power (ROP) is shown in Figure 3.25(c). The maximum realized ROP after 2 km transmission is -7 dBm, which is insufficient to reach the BER floor. The small signal swing and modulation depth (< 0.2) result in low optical modulation amplitude (OMA) and extinction ratio, which limits the SNR at the receiver. This blends with the marginal improvement in BER with the increase in the FFE taps; indicating that the system is limited by the receiver SNR rather than the bandwidth.

3.4.4 Transmission performnace with RF driver

For comparison and to define the attainable performance, we tested the module with an RF amplifier and a higher bandwidth PIN/TIA module (33 GHz). The RF amplifier alleviates the limitations on the signal swing, given the fair V_π of the modulator. Besides, the higher bandwidth of the PIN/TIA extends the operational bandwidth of the system beyond 30 GHz. Figure 3.26 shows the achieved BER for PAM4 signals at different symbol rates. We transmit 56 Gbaud PAM4 (105 Gbps net rate) over 2 km under the 3.8×10^{-3} HD-FEC BER threshold using only 7 taps FFE. Using 51 taps FFE, we report the transmission of 70 Gbaud (131 Gbps net rate) below the HD-FEC threshold and 60 Gbaud (114 Gbps net rate) under the KP4-FEC BER threshold. Since only a 3 taps pre-emphasis filter is employed at the transmitter, the RF chain frequency response is not pre-compensated accurately or adequately. Thus, a large

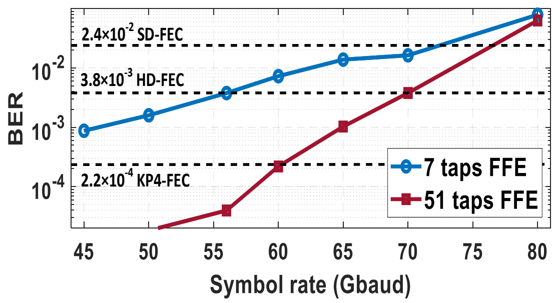

Figure 3.26. The BER versus symbol rate for PAM4 signals using a 38 GHz driver after 2 km transmission.

Table 3.4. Summary of Transmission Rates Achieved with and without RF Driver

FEC	Driver-less		With RF driver		Penalty (%)
	Format	Net (Gbps)	Format	Net (Gbps)	
KP4-FEC	28 Gbaud PAM4	53	60 Gbaud PAM4	114	53 %
HD-FEC	36 Gbaud PAM4	67	70 Gbaud PAM4	131	48 %

number of taps is required by the FFE to compensate for the combined frequency of the RF amplifier, packaged MZM module, and the PIN/TIA module.

Moreover, the transmission of 53 Gbaud PAM4 (net 100 Gbps) over 10 km (with optical amplification) under the KP4-FEC BER threshold is achieved using the bare die modulator, similar DSP routine, and an older generation AWG [97].

Table 3.4 provides a summary of the transmission performance for both scenarios: with and without an RF driver. The results show a significant penalty in performance when the RF driver is eliminated, amounting to approximately 50% at the considered FEC thresholds. This penalty is primarily attributed to the high V_π of the SiP MZMs. It indicates that the RF driver plays a crucial role in achieving higher transmission rates, despite its high power consumption.

3.5 Silicon Photonic Vestigial Sideband Transmitter for Long-Reach C-band IMDD Transmission [99]

So far, this chapter discussed our work on high-speed IMDD transmission systems targetting O-band short-reach applications. In this section, we focus on longer-reach C-band IMDD transmission as we present our design and experimental validation of a cost-effective SiP vestigial sideband transmitter.

Employing the C-band in IMDD transmission is seriously limited by CD-induced power fading. The achievable transmission reach depends on the position of the first spectral null, which is inversely proportional to the square root of the transmission distance, as described in equation 2.7 and shown in Figure 2.2. To address CD-induced power fading in the optical domain, optical dispersion compensating modules (DCMs) or optical filters with sharp roll-off characteristics can be used to create SSB signal [100]. However, these components add substantial expenses to the transceiver cost. Alternatively, CD pre-compensation or SSB signaling can be employed to mitigate power fading, but these approaches require the use of an additional DAC for complex modulation using either IQ or dual-drive modulators. These solutions negate the cost-effectiveness and simplicity of IMDD.

The authors in [101] showed that inducing a time skew between differential arms of the DD-MZM creates a vestigial sideband (VSB) signal. A sinusoidal envelope modulates the DD-MZM output optical signal, creating a VSB signal with the optimal skew. Previous works employed high-bandwidth tunable RF delay lines for VSB transmission [101, 102]; however, incorporating an RF delay line into the IMDD architecture increases cost and complexity.

Building on the proposed principle [101], here we present the design and characterization of a C-band SiP DD-MZM with an optimized passive optical delay line for VSB signal generation. We compare the transmission performance of two SiP DD-MZMs, with and without the optical delay line, to quantify the gain of VSB transmission and the effective mitigation of the power fading. Using a single DAC and the delay-based DD-MZM, we transmit a 56 Gbaud PAM4 signal over 60 km of SSMF under the 3.8×10^{-3} HD-FEC BER threshold, which corresponds to net 105 Gbps. We only considered second-order Volterra nonlinear equalization; neither signal-signal beat interference (SSBI) cancellation nor Kramer–Kronig (KK) field recovery is employed in this work.

3.5.1 Delay-assisted VSB generation principle

A dual drive (DD) MZM driven with differential signal $\pm s(t)$ with a temporal skew τ has an output field that can be written as:

$$E_o(t) = \frac{1}{\sqrt{2}} E_{in}\, e^{(js(t)+j\Phi)} + \frac{1}{\sqrt{2}} E_{in}\, e^{(-js(t-\tau)-j\Phi)} \quad (3.1)$$

Here E_{in} is the input field to the DD-MZM, E_o is the field at the output, and Φ is the constant phase-shift that sets the bias point of the DD-MZM. Using the approximation $e^x \approx 1 + x$, the output field can be rewritten as

$$E_o(t) = \frac{1}{\sqrt{2}} E_{in} e^{j\Phi}\big(1 + js(t)\big) + \frac{1}{\sqrt{2}} E_{in} e^{-j\Phi}\big(1 - js(t-\tau)\big) \quad (3.2)$$

$$E_o(t) = C + \frac{j}{\sqrt{2}} E_{in}\left(e^{j\Phi} s(t) - e^{-j\Phi} s(t-\tau)\right) \quad (3.3)$$

To see the impact of the temporal delay on the signal spectrum, we us the Fourier transform.

$$FT\big(E_o(t)\big) = C + \frac{j}{\sqrt{2}} E_{in}\big(e^{j\Phi} S(f) - e^{-j\Phi} S(f) e^{-j2\pi f\tau}\big) \quad (3.4)$$

$$FT\big(E_o(t)\big) = C - \frac{2j}{\sqrt{2}} E_{in} e^{-j\pi f\tau} sin(\Phi + \pi f\tau)\, S(f) \quad (3.5)$$

Therefore, the signal spectrum $S(f)$ is shaped by the factor $\sin(\Phi + \pi f \tau)$, which is asymmetrical with reference to the zero frequency as illustrated in Figure 3.27. Thus, the delay result in a spectral notch in one of the sidebands; whereas the position of the notch depends on the temporal delay (skew).

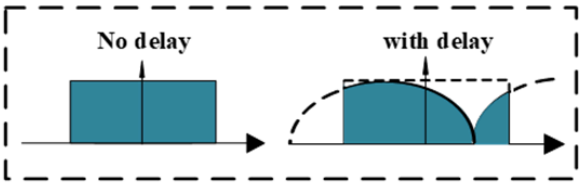

Figure 3.27. Illustration of the impact of the temporal skew on the DD-MZM output signal spectrum.

This approach uses a single DAC with differential outputs and a delay line to generate the VSB signal. The implementation of the delay can be done either in the RF domain or optically. Previous studies utilizing this principle have utilized RF delay lines, which have limitations in terms of bandwidth and cost, thereby undermining their effectiveness. On the other hand, optical delay lines are cost-free as they can be easily integrated into the structure and do not have bandwidth limitations. However, the use of optical delay lines introduces an imbalance in the MZM, leading to a reduction in its extinction ratio and free spectral range (FSR). In this work we adopted the optical delay approach as it does not add any extra hardware overheads.

3.5.2 Implementation

The cross-sectional view and schematic of the DD-MZMs are presented in Figure 3.28(a-b). The chip was fabricated at the Advanced Micro Foundry (AMF) with a standard CMOS-compatible SiP process flow. The DD-MZM is composed of two independent and identical phase shifters connected in parallel. A single differential output DAC drives the two carrier depletion phase shifters, which reduces the driving voltage requirements. Each phase shifter is 4 mm long at a fill factor of 85%. Adding periodic intrinsic regions prevents the flow of electric currents through the optical waveguides. The RF electrodes are designed to match the 50 Ω characteristic impedance of the test equipment and are terminated with an on-chip N^{++} 50 Ω resistor. Grating couplers connect the DD-MZMs optically with 11 dB (overall) coupling loss.

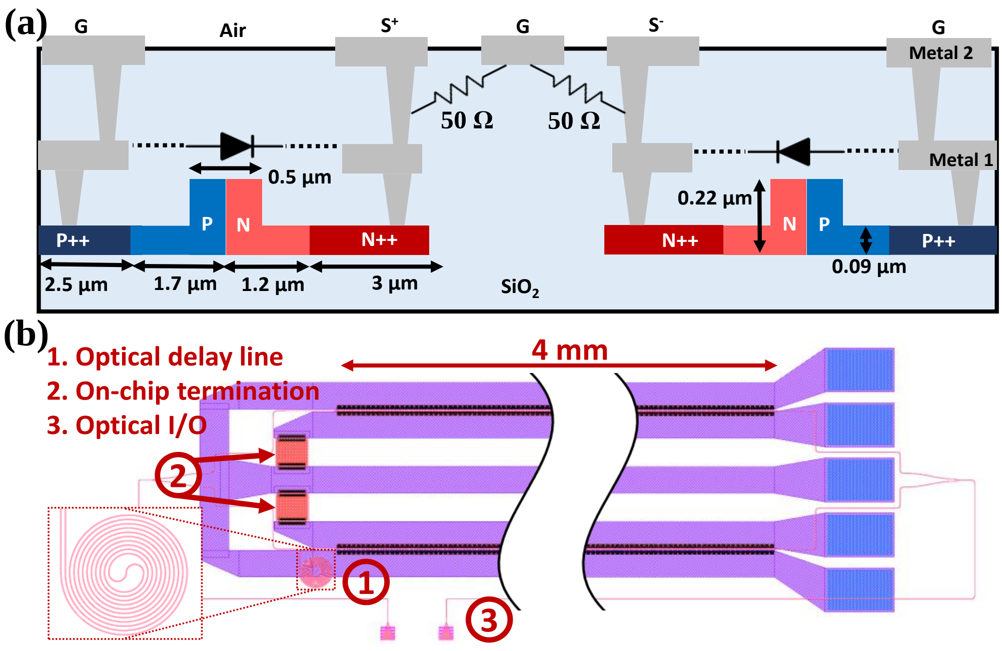

Figure 3.28. (a) DD-MZM cross-section (not to scale). (b)The DD-MZM layout.

The base DD-MZM (without delay) and a DD-MZM with a 10 ps optical delay are fabricated on the same chip; thus, they share the same RF characteristics as shown in Figure 3.29. Under 3 V reverse bias, the DD-MZM propagation loss and DC extinction ratio are 5 and 25 dB, respectively. The measured DC V_π of the individual phase shifter is 6.5 V. Figure 3.29(b) shows the frequency response of the base DD-MZM design. The DD-MZM has a 3- (6-) dB bandwidth of 18 (26) GHz at 3 V reverse bias. The modest electro-optic bandwidth of DD-MZMs is attributed to the parallelly connected PN junction capacitances. Yet, the frequency response has a slow roll-off factor enabling operating beyond the 3-dB point.

The passive optical delay line is composed of a single spiral waveguide with a total length (d) of 720 μm, which corresponds to a delay (τ) of 10 ps for a group index (n_g) of 4.18 according to this relationship.

$$d = {}^{c\tau}\!/_{n_g} \tag{3.6}$$

Where c is the speed of light in free space. Figure 3.30(a) shows the simulated group index and corresponding delay for a 720 μm spiral waveguide with a width of 500 nm as a function of the wavelength across the C-band. In addition, Figure 3.30(b) presents the delay sensitivity to the temperature at 1550 nm. The simulated delay deviates by less than 2% across the entire C-

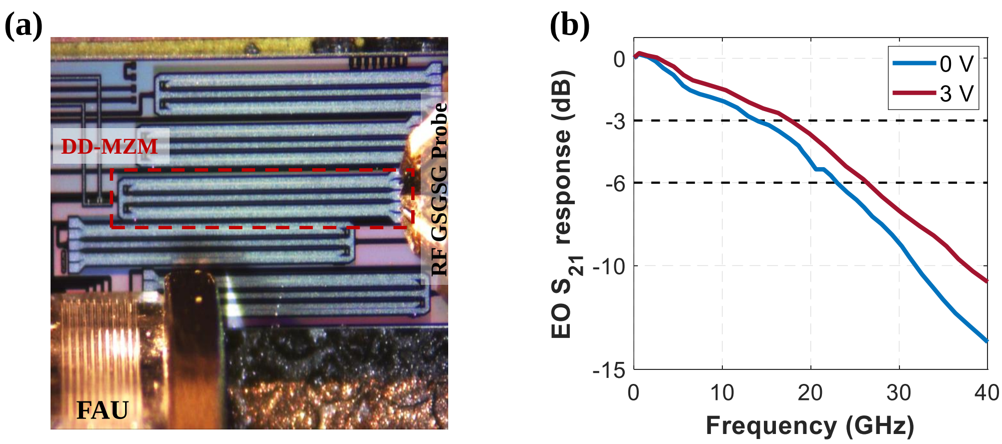

Figure 3.29. (a) The fabricated chip showing the optical fiber array unit (FAU) and RF probe (GSGSG). (b) The electro-optic (EO) S21 response normalized at 1.5 GHz.

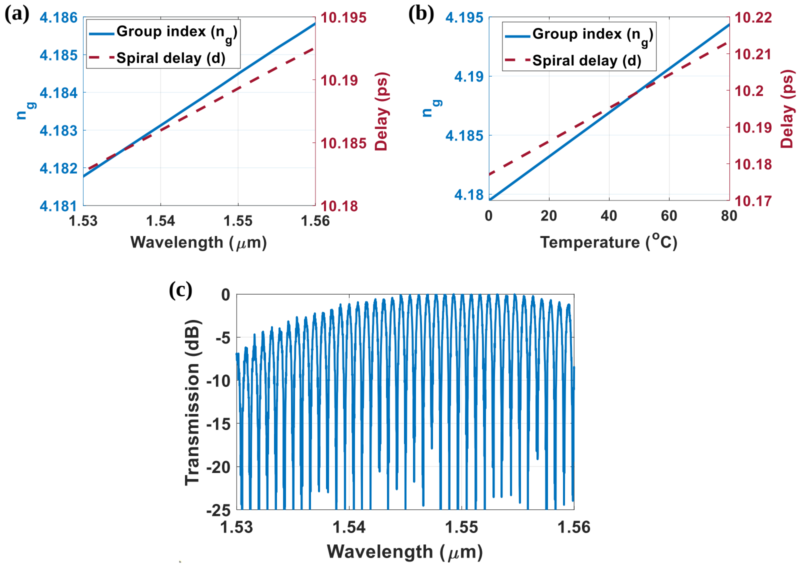

Figure 3.30. (a) The delay dependency on the wavelength. (b) The delay sensitivity to temperature. (c) The measured optical transfer function of the DD-MZM with 10 ps skew.

band and from 0 to 80 ^{0}C. One drawback of implementation is that it will result in narrow FSR, which is actually comparable with the RF signal bandwidth. The FSR for an imbalanced MZM is given by:

$$FSR_{MZM}(Hz) = \frac{c}{n_g d} \tag{3.6}$$

For a 10 ps skew at 1550 nm, the FSR is 100 GHz, which sets a limit on the symbol rate that can be transmitted using this DD-MZM. Another drawback is that the imbalance reduces the extinction ratio of the MZM; however, the simulated optical loss due to the 720 µm is less than 1 dB as the radius of all the spiral rounds is larger than 10 µm. Having a 1 dB imbalance in propagation loss yields a theoretical extinction ratio of more than 30 dB [103]. We measured only 25 dB of extinction ratio, which is attributed to the MZM imperfect Y-branch splitter.

In our design process, we carefully considered the FSR and the expected bandwidth of the DD-MZM. Based on these considerations, we selected a delay of 10 ps to best support 56 Gbaud operation. It is worth noting that in a previous study [101], the optimal delay was found to be dependent on the symbol rate and transmission reach. However, in our methodology, we intentionally fixed the delay at 10 ps, which falls within the optimal range for 56 Gbaud transmission. With this configuration, our objective was to determine the maximum achievable transmission reach.

3.5.3 Transmission experiment

The experimental setup is shown in Figure 3.31. The transmitter DSP follows the description of the DSP stacks presented in the previous sections. The RF signal is loaded to a differential output DAC followed by a matched pair of SHF 807c RF drivers (55 GHz bandwidth, 23 dB gain) that drive the DD-MZM via a 50 GHz GSGSG probe. Optically, an ECL operating at 1550 nm with 15 dBm output power feeds the DD-MZM. We test the two DD-MZM, with and without the optical delay line, with the same testbed configuration for fair comparison. After the chip, the optical signal is amplified by an EDFA to compensate for the grating couplers' loss and then transmitted over various distances of dispersion-uncompensated SSMF. Another EDFA is used after fiber transmission to compensate for the fiber loss, as the receiver does not employ a TIA.

The receiver DSP is carried out at 2 sps. For comparison, we considered both linear FFE and Volterra nonlinear equalizer (VNLE). After equalization, we apply blind geometric distortion to subdue equalization-enhanced noise [65], we discuss this technique in more details in Chapter 6. Eventually, the recovered symbols are used for BER calculations.

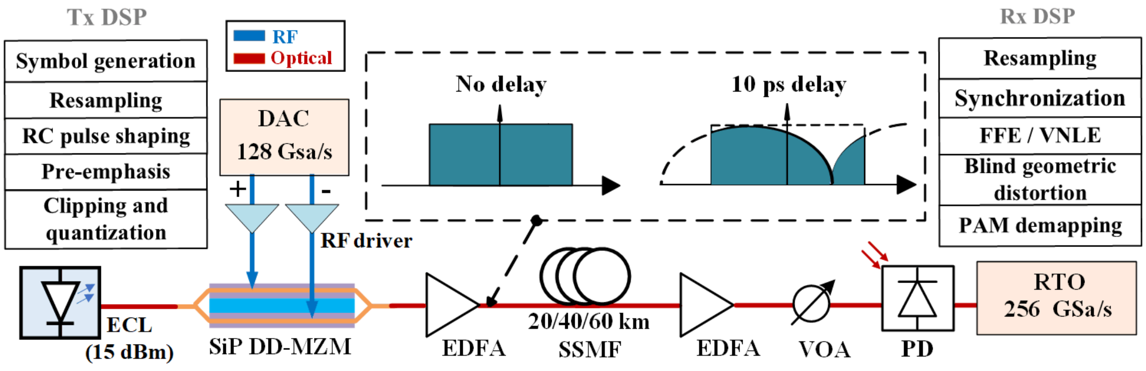

Figure 3.31. (a) The experimental setup. The inset illustrates the output optical spectrum for the two DD-MZMs under test.

The generated optical spectra of 56 Gbaud PAM4 signals for both DD-MZM structures are shown in Figure 3.32(a). The skew induced by the 10 ps optical delay line filters out one sideband, creating a VSB signal. VSB reception reduces the strength of CD-induced power fading and enables longer-reach IMDD transmission in the C-band. Figure 3.32(b-d) show the received electrical spectra of 56 Gbaud PAM4 for both DD-MZMs after different fiber lengths. At B2B, the skew induced by the optical delay line effectively filters the high-frequency components of the signal as illustrated in Figure 3.27 and Figure 3.32(b). After fiber transmission, the received electrical spectra have strong dips because of the image band and the CD-induced power fading, as shown in Figure 3.32(c-d). The DD-MZM with the 10 ps delay has shallower dips because of the VSB nature of the transmitted optical signal, which improves the transmission performance considerably. But due to the sinusoidal filtering nature, the higher frequency components at the image band are not attenuated strongly. This causes

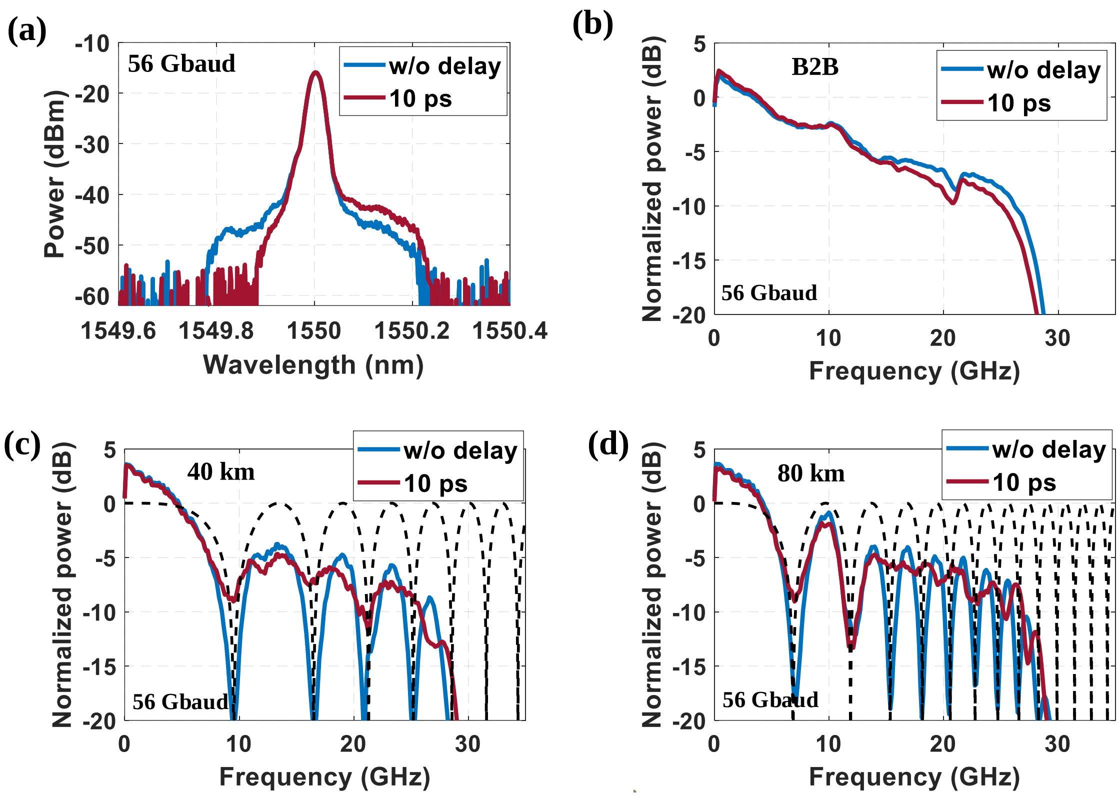

Figure 3.32. (a) Optical spectra of the DD-MZM without (w/o) delay and the DD-MZM with 10 ps optical delay line. (b-d) Electrical spectra of the received waveform after transmission in SSMF at B2B, 40 km, and 80 km (dashed line shows the theoretical transfer function of dispersive chirp-free IMDD channel).

stronger notches at those frequencies. However, this can be easily filtered with a slow roll-off optical filter or offsetting the Mux-Demux filter [102]. Yet, we do not employ any SSBI mitigation or CD compensation and rely solely on the nonlinear equalization at the receiver.

For optimal transmission performance, we first optimize the launch optical power (LOP) into the fiber for the different transmission distances, as shown in Figure 3.33(a). Then, we optimize the carrier-to-signal power ratio (CSPR) by adjusting the driving swing into the SiP DD-MZM. We observe that the optimum CSPR is 16 dB. Given that we are not using any SSBI cancellation technique, the optimal CSPR is relatively high so that the impact of the contribution of signal-signal beating diminishes.

Figure 3.33(b) shows the calculated BER versus the symbol rate for both DD-MZM structures at B2B and after 40 km transmission. In the absence of CD (B2B transmission), the

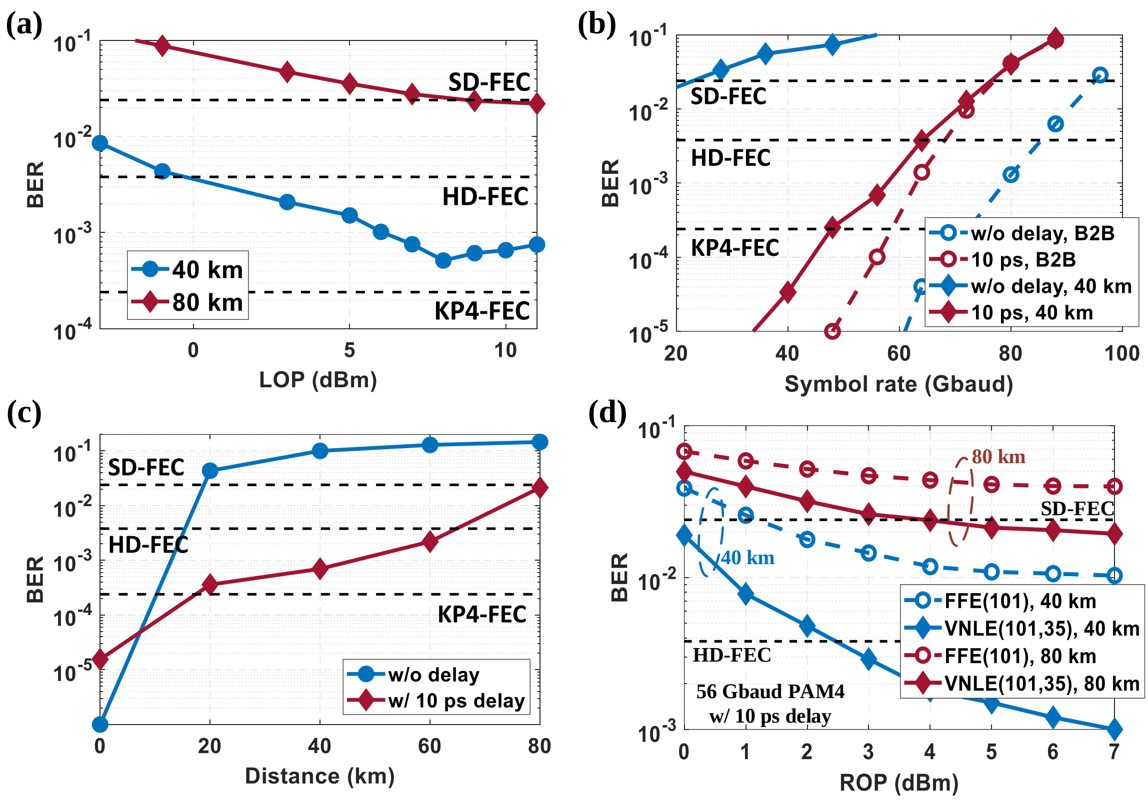

Figure 3.33. (a) The BER versus the launch optical power into the fiber at 56 Gbaud PAM4. (b) BER versus symbol rate at B2B and 40 km transmission using both DD-MZMs with VNLE. (c) The BER versus transmission distance. (d) BER versus ROP for the DD-MZM with 10 ps delay after 40 and 80 km transmission.

skew induced by the optical delay line results in a modest performance penalty because of high-frequency suppression. This penalty increases with the signal bandwidth (symbol rate). After 40 km transmission, CD-induced power fading significantly deteriorates the transmission performance of the base DD-MZM design (without delay, DSB transmission). The DD-MZM with 10 ps delay results in a VSB optical signal that results in acceptable performance, allowing the transmission of 56 Gbaud PAM at a BER of 1.5×10^{-3}, which corresponds to net 105 Gbps assuming the 6.7% overhead HD-FEC threshold.

Figure 3.33(c) depicts the BER versus the transmission distance for both DD-MZMs with either FFE or VNLE. By optimizing the LOP and CSPR, we successfully transmit net 100 Gbps over 60 km with the HD-FEC. Even after 80 km, the added delay improves the performance and enables the transmission of 56 Gbaud PAM4 under the 2.4×10^{-2} SD-FEC threshold. The BER sensitivity to the ROP after 40 and 80 km transmission using the DD-MZM with the 10 ps delay is shown in Figure 3.33(d). Second-order VNLE with 101 first-order and 35 second-order kernels improves the performance considerably compared to linear FFE because of the ripply distorted spectrum of the signal. The gain of employing VNLE is less pronounced after 80 km because of the increase in the number of frequency dips, as shown in Figure 3.32(b-d).

In summary, the presented DD-MZM with a passive optical delay line adds neither complexity nor cost to the transmission system. Compared to inducing the delay in the RF domain, the proposed structure is advantageous as optical delay lines are compact, costless, and not limited by RF signal bandwidth. Moreover, the demonstrated optical VSB transmitter uses a single DAC without optical filtering. This work employs conventional DSP, which signifies the impact of the added passive optical delay line and achieved transmission performance. It is important to note that nonlinear equalization was required in this work, shifting the processing load from hardware to the ASIC engines. This approach is advantageous, as advancements in ASIC fabrication and shrinking process nodes allow for the integration of more functionalities with minimal increase in footprint, cost, and power consumption.

Chapter 4

Unamplified Coherent Transmission for High-Speed Intra-Datacenter Interconnects

4.1 Overview

To address the surging traffic demand in intra-datacenter communications, particularly over distances of 2 to 10 km, dispersion-tolerant coherent transmission systems are being considered as an alternative to IMDD systems. While IMDD systems currently serve as the standard for applications up to 2 km at 200 Gbps/λ [33], their capacity scaling is severely limited by chromatic dispersion, even when operating in O-band. In IMDD systems, increasing the symbol rate or transmission reach is challenging due to the accumulated dispersion on the edge channels of the CWDM grid (i.e., 1270 nm and 1330 nm). On the other hand, coherent transmission is resilient to dispersion and scales better with symbol rate, making it more suited to accommodate the escalating data traffic demand. Despite initial concerns regarding the added complexity and power consumption of coherent systems, the continued scaling of CMOS technology from 7 to 3 nm suggests that the ASIC power consumption envelope for both IMDD and coherent transceivers will potentially converge [41, 42]. Moreover, the IEEE 802.3 Ethernet Task Forces are currently investigating 800 G and 1.6 T capacity systems for intra-DCIs based on both IMDD and coherent transceiver architectures [104]. It is yet debatable whether to employ the O-band or the C-band in these short-reach coherent systems, we discuss further on this topic in the following sections.

Although coherent receivers offer higher detection sensitivity because of the mixing of the signal with local oscillator (LO), operating without optical amplification mandates reducing the link overall optical loss. A low loss electro-optic modulator with a low V_π (for low modulation loss) is necessary to dispense the need for optical amplification in this short-reach scenario. TFLN modulators stand as a promising candidate for unamplified coherent systems because of their very low optical propagation loss (< 0.7 dB/cm), enabling long devices with low V_π, while maintaining high bandwidths due to the low RF loss [15, 16]. Accordingly, this chapter focuses on employing TFLN-based coherent transmission systems in intra-DCIs operating under 10 km.

4.2 C-band Unamplified Coherent Transmission of Net 500 Gbps/Polarization/λ for Intra-Datacenter Interconnects [105]

This work evaluates the transmission performance of a C-band coherent transmission system employing a high bandwidth TFLN IQM and TIA-free PIN photodiodes over short distances (2 to 10 km). We analyze the driving voltage and DSP requirements for optimum performance in the absence of optical amplification and receiver TIA; highlighting the relaxed optical power budget. We experimentally demonstrate the transmission of 124 Gbaud 32QAM on a single polarization over 10 km of SMF with 2.5 V_{pp} drive signals below the 2.4×10^{-2} SD-FEC BER threshold, corresponding to a net rate of 516 Gbps on a single polarization. Moreover, we transmit 124 Gbaud 16QAM over 10 km below the 3.8×10^{-3} hard-decision (HD)-FEC BER threshold, which corresponds to 465 Gbps net rate and is aligned with the envisioned 800G LR1 standard [48]. These results support the promise of practical unamplified coherent systems with data rates beyond 1 Tbps/λ over the intra-DCI reach with standard polarization division multiplexing and currently available electronics analog bandwidths.

4.2.1 IQM characterization and experimental setup

The experimental setup and DSP routines employed in this work are presented in Figure 4.1. At the transmitter, we generate the QAM symbols from a random binary sequence. Due to the higher number of levels and sensitivity to nonlinearity, we apply nonlinear pre-distortion (NLPD) on the 32QAM symbols using a 3-symbol nonlinear lookup table (NLLUT) [61]. The complex signal is up-sampled and shaped with RRC filter. Then, the I (real) and Q (imaginary) components of the signal are filtered with the pre-compensation filters depicted in the inset of Figure 4.1. These digital filters pre-compensate the frequency response of the AWG channel and the RF amplifier up to 70 GHz. The 10 dB point is around 60 GHz; thus, the RRC filter roll-off factor (α) is set to limit the signal bandwidth to 60 GHz for symbol rates under 120 Gbaud. The I and Q signals are clipped to limit their PAPR before loading the signals to the AWG running at 256 GSa/s but externally interleaving two 128 GSa/s DAC outputs. The

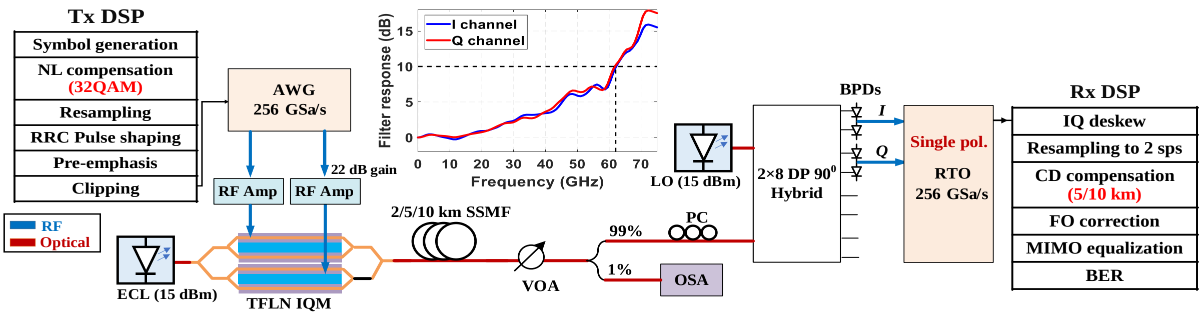

Figure 4.1. The experimental setup and DSP blocks applied at the transmitter (Tx) and receiver (Rx). The inset shows the pre-compensation filters response.

observed optimum PAPR of the digital signal is ~ 9 dB. The AWG output is amplified using a matched pair of 60 GHz 22-dB gain RF amplifiers (SHF804b), which drives the TFLN IQM using a GSG-GSG 67 GHz RF probe, as shown in the inset of Figure 4.2(a).

The IQM is optically connected through vertical grating couplers that have peak transmission around 1563 nm and back-to-back insertion loss of 11 dB (5.5 dB/facet). This work uses external cavity lasers with 100 kHz linewidth and 15 dBm optical power. The output of the IQM is transmitted over different lengths of SSMF and followed by a VOA for sweeping the received optical power (ROP), which is the input optical power to the coherent receiver (hybrid).

The receiver employs a 2×8 dual-polarization (DP) optical hybrid that mixes the signal with the local oscillator (LO). Therefore, only 12 dBm of the LO power is actively coupled to our single-polarization signal and a polarization controller (PC) is used to align the signal polarization state with the LO. The hybrid outputs are detected by a pair of 70 GHz balanced photodiodes (BPD) and digitalized by the 256 GSa/s RTO. The offline receiver DSP deskew the received signals as the employed BPDs are not matched, then Gram-Schmidt orthogonalization compensates for the hybrid imperfections and the fixed impairments of the system. The signals are resampled to 2 sps for chromatic dispersion (CD) compensation and frequency offset (FO) correction. Then, a 51-tap T/2-spaced 2×2 multiple-input-multiple-output (MIMO) equalizer with real-valued coefficients and interleaved with a second-order phase-locked loop (PLL) is employed to track the phase noise and compensate for the frequency response of the RF probes, IQM, and BPDs. The real-valued MIMO equalizer filters each quadrature independently and can correct the power imbalance and timing skew between the I and Q quadratures [75]. Finally, the BER is calculated based on the demapped bit sequence of the received symbols.

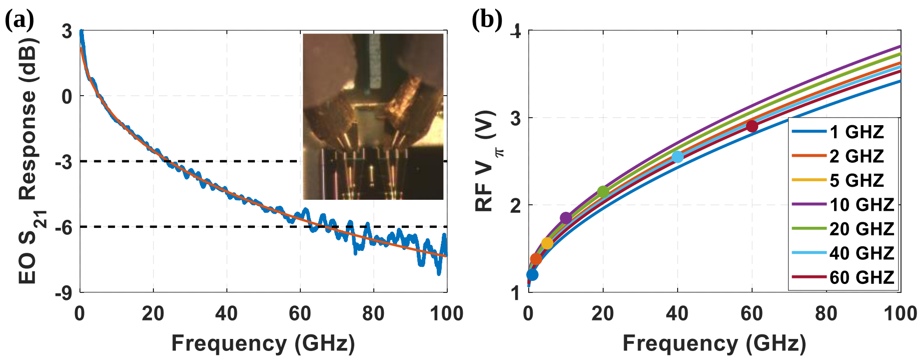

Figure 4.2. (a) The frequency response of the TFLN IQM normalized to 5 GHz. (b) The measured and extrapolated RF V_π.

The TFLN IQM is composed of nested MZMs with 23 mm coplanar waveguide electrodes and on-chip termination close to 50 Ω. The bias points are set with thermal phase shifters, to minimum transmission (null) for the children MZMs and to quadrature for the parent MZM. The measured small-signal electro-optic frequency response (S_{21}) of a MZM identical to those used in the IQM is shown in Figure 4.2(a). The characteristic slow roll-off response of TFLN MZMs is observed with a 3-dB bandwidth of 24 GHz and 6-dB bandwidth of 65 GHz. Figure 4.2(b) shows the measured RF V_π at different frequencies. Each data point is extrapolated from DC to 100 GHz using the measured EO S_{21} response. The measured low-MHz V_π is 1.25 V that increases to ~ 3 V at 60 GHz.

4.2.2 Transmission results

The summary of the transmission experiment results is presented in Figure 4.3(a). On a single polarization, we transmit 128 (124) Gbaud 16QAM over 2 (10) km under the 6.7% overhead HD-FEC BER threshold of 3.8×10^{-3}, which represents a net rate of 480 (465) Gbps. Adopting a higher FEC threshold, we demonstrate the transmission of 128 (124) Gbaud 32QAM over 2 (10) km at a BER below the 2.4×10^{-2} threshold of the 20% overhead SD-FEC, corresponding to a net rate of 533 (516) Gbps.

Figure 4.3(b) shows the BER dependency on the driving voltage for 128 Gbaud signals

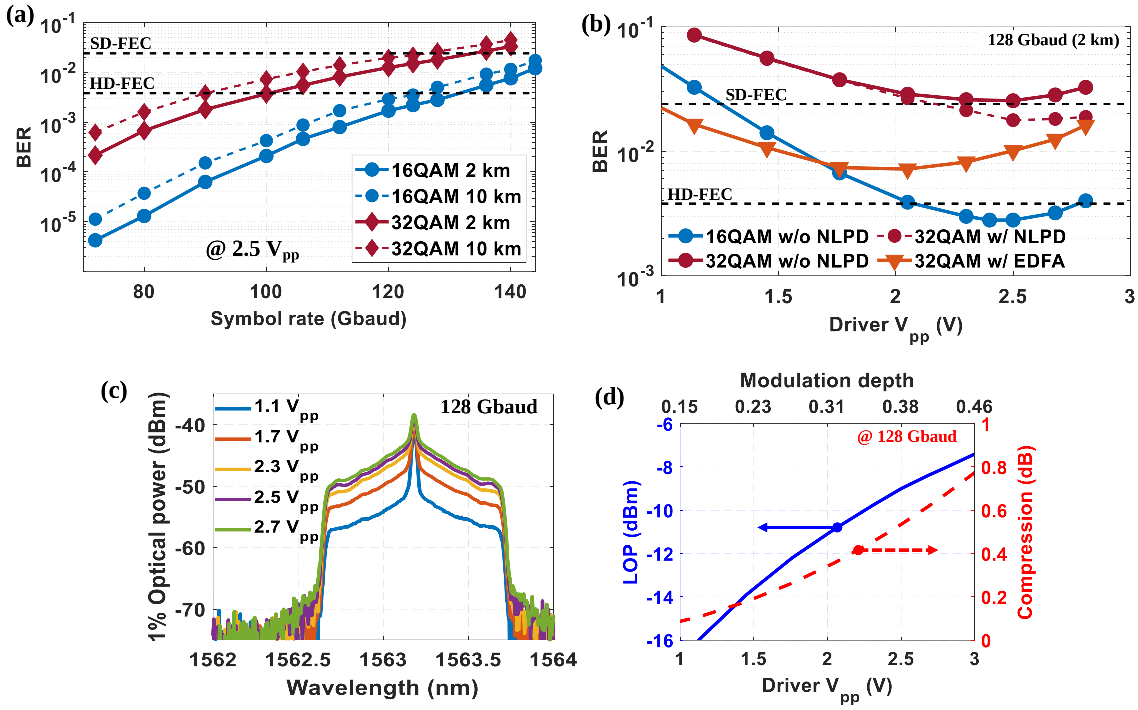

Figure 4.3. (a) The BER versus the symbol rate. (b) The BER sensitivity to the drive voltage. (c) The optical spectra of 128 Gbaud 32QAM at different drive voltages at 0.03 nm. (d) The measured launch optical power (LOP) into the fiber (solid, blue) and the calculated IQM nonlinear compression (dashed, red) versus the driving voltage with the modulation depth on the top axis.

transmitted over 2 km of SSMF. The observed optimum drive voltage is 2.5 V_{pp}. The nonlinearity stemming from the RF amplifier and IQM transfer function dominates the ADC noise beyond 2.5 V_{pp}, which degrades the BER performance. Figure 4.3(c) plots the optical spectra of 128 Gbaud for different driving levels, the increase in signal power saturates beyond 2.3 V_{pp}. The considerable carrier leakage comes from the modest extinction ratio of the child MZMs (~ 20 dB).

Figure 4.3(d) shows the output optical power of the IQM launched into the fiber versus the driving voltage and the modulation depth ($\mathrm{M_D} = \mathrm{V_{pp}}/2\mathrm{V_\pi}$), assuming an RF V_π of 3.25 V (64 GHz), besides the calculated nonlinear compression arising from only the IQM transfer function ($C_{IQM} = -20\log_{10}(\mathrm{sinc}\,(\pi \mathrm{M_D}/2))$, as defined in [106]. Considering only the IQM nonlinear transfer function, the optimum modulation depth is between 0.5 and 0.6, which addresses the trade-off between modulation loss and nonlinear compression [106]. However, the employed RF amplifier 1 dB compression point is 2.5 V_{pp}, which increases the transmitted signal nonlinearity and dedicates operating at a lower modulation depth. At 2.5 V_{pp}, the launch optical power (LOP) into the fiber is -9 dBm. The optical spectra of 128 Gbaud 32QAM signals as a function of the drive voltage are shown in Figure 4.3(c) at 0.03 nm resolution.

The BER versus the transmission distance of 112/128 Gbaud 16QAM and 32QAM signals is given in Figure 4.4(a). After compensating the CD, the degradation in transmission performance from 2 km to 10 km arises from the ~1.5 dB extra fiber loss, which reduces the ROP in the absence of optical amplification.

The BER sensitivity to the ROP at 128 Gbaud after 2 km fiber transmission is depicted in Figure 4.4(b), the BER degrades rapidly with the ROP as the system is limited by the receiver sensitivity and the ADC noise. Replacing the vertical grating couplers (5.5 dB/facet) with edge couplers (2.5 dB/facet) shall increase the ROP by 6 dB, which will increase the SNR and

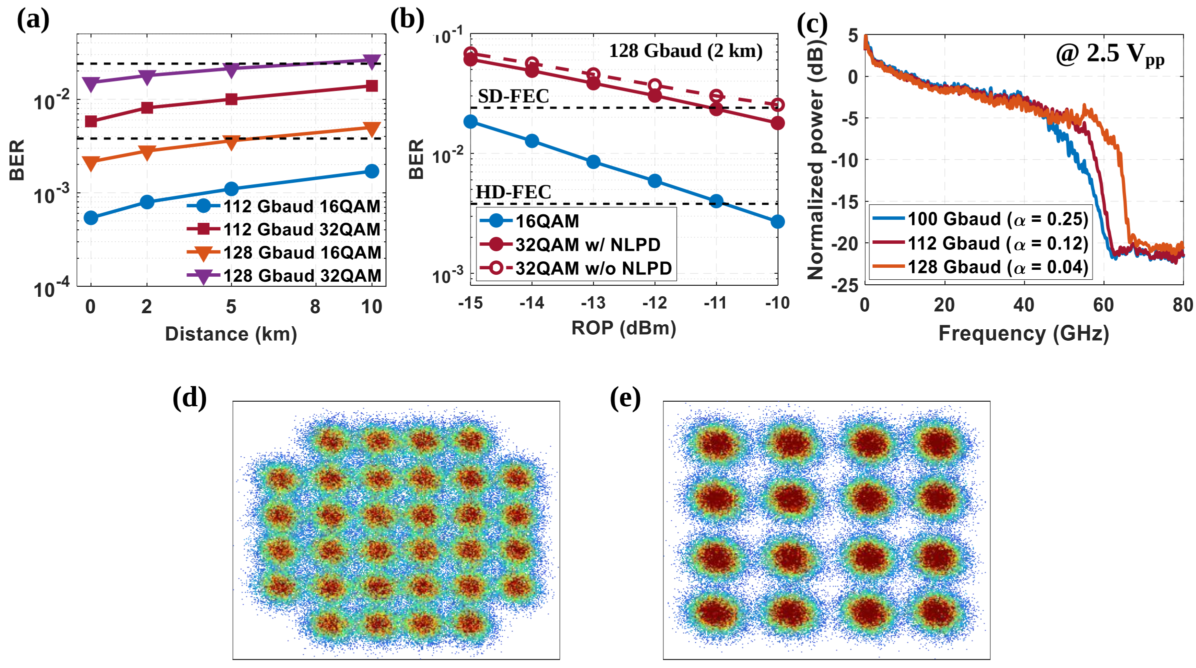

Figure 4.4. (a) The BER versus the transmission distance. (b) The BER versus ROP at 128 Gbaud after 2 km transmission. (c) The received RF spectra at different symbol rates of 32QAM. The received constellations of 124 Gbaud 32QAM (d) and 16QAM (e) after 10 km.

improve the transmission performance considerably. Considering the 128 Gbaud 32QAM signal, a 1 dB ROP gain is observed at the SD-FEC threshold when NLPD is employed. Although our experimental setup does not include TIAs after the BPDs, it detects signals below -10 dBm owing to mixing with the LO and the higher detection sensitivity of coherent receivers.

Figure 4.4(c) plots the received RF spectra at different symbol rates. The 128 Gbaud signal experiences ~7 dB drop at 60 GHz, which corresponds to the combined frequency response of the RF probes, TFLN IQM, and BPDs, and requires large number of MIMO taps for proper equalization. Figure 4.4(d-e) show the constellations of 124 Gbaud 16QAM and 32QAM after 10 km transmission, which respectively correspond to net rates of 465 and 516 Gbps.

It is yet debatable whether to employ O-band or C-band lasers in such short-reach unamplified coherent systems. The primary drawback of operating in the C-band is the need to digitally compensate for the CD, which increases the ASIC power consumption [8, 9]. For 2 km reach, the accumulated CD is adequately low that it does not require a dedicated DSP block for compensation [5, 8]. In this work, we adopted the conventional time-domain finite impulse response (FIR) CD compensation filter [73].

Figure 4.5(a) shows the BER sensitivity to the length of the MIMO filters for 128 Gbaud signals after 2 km transmission with and without CD compensation. It is observed that 51 taps are sufficient to reach the BER floor. Interestingly, when sufficient MIMO filter taps are employed, the performance with and without CD compensation converge to the same BER. This confirms that up to 2 km (~34 ps/nm), the MIMO adaptive filtering effectively equalizes the frequency response and compensates for the chromatic dispersion simultaneously; dispensing the need to have a dedicated CD compensation step. Considering 10 km transmission (~170 ps/nm), Figure 4.5(b) shows the BER dependency on the length of the CD

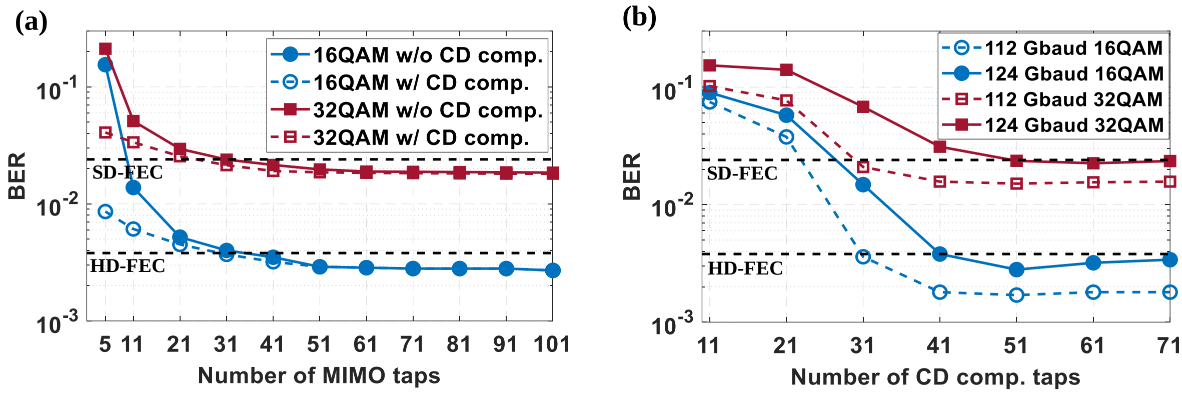

Figure 4.5. (a) The BER performance versus the number of MIMO taps for 128 Gbaud signals after 2 km. (b) The BER sensitivity to the CD compensation filter length after 10 km transmission.

compensation FIR filter. The required filter length is independent of the QAM order and is proportional to the square of the symbol rate (B^2); thus, we reach the BER floor for 112 Gbaud signals with 41 taps, while 51 taps are needed for the 124 Gbaud signals. With the advancements in ASIC performance and progression towards smaller technology nodes, the constraints on ASIC power consumption are relaxed and compensating the CD digitally adds modest overhead [107].

In this work, we operated a C-band TFLN-based coherent transmission system for 2 to 10 km transmission without optical amplification in the absence of TIAs, which burdens the optical power budget considerably. Yet, we discussed the transmission characteristics in detail, focusing on C-band operation. The next section considers the other potential architecture, which operates in the O-band with DFB lasers rather than costly ECLs.

4.3 Next-Generation O-band Coherent Transmission for 1.6 Tbps 10 km Intra-Datacenter Interconnects [108]

This section discusses our proposal of employing O-band coherent transmission systems inside the dataceneter for short-reach communications. We demonstrate the first O-band single-fiber transmission system supporting net 1.6 Tbps operation over 10 km while employing cost-effective DFB lasers. We empirically evaluate the transmission performance using the different transmitter configurations and analyze the penalty associated with employing DFB lasers compared to narrow linewidth ECLs. In addition, we provide a power consumption comparison of various candidate architectures for 1.6 Tbps transceivers based on the published literature, which further supports our proposal for deploying single-carrier O-band coherent transceivers within datacenters.

Operating in the O-band and employing coherent transmission techniques optimally fulfills several system objectives, as outlined below:

1) The capacity can be scaled by increasing the symbol rate as it is not limited by chromatic dispersion.
2) Optical amplification is unnecessary for distances up to 10 km, thereby reducing system complexity.
3) Digital dispersion compensation is not required in the receiver's DSP stack, simplifying the DSP architecture.
4) In the absence of dispersion, equalization-enhanced phase noise (EEPN) diminishes.
5) Feasibility of utilizing cost-effective DFB lasers with relaxed linewidth requirements.
6) Datacenter operators can take advantage of the mature O-band component market, offering a wider range of readily available and reliable components.

Figure 4.6 provides a summary of the recently reported high-speed demonstrations for O-band IMDD and coherent transmission systems. Here we present the first O-band link operating over 10 km with a net rate exceeding 1 Tbps. The system utilizes a TFLN IQ modulator and two DFB lasers, and compares two generations of DACs. Specifically, we achieve (a) a net rate of 1.2 Tbps using a single DAC per quadrature (128 GSa/s) at 120 Gbaud DP-64QAM with the 2.4×10^{-2} 20% SD-FEC BER threshold, and (b) a net rate of 1.6 Tbps using two interleaved

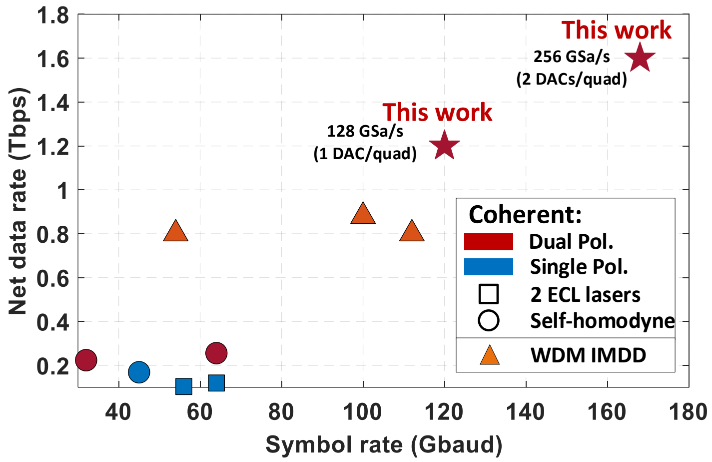

Figure 4.6. Review of recent O-band transmission system demonstrations.

DACs per quadrature (256 GSa/s) at 167 Gbaud DP-64QAM with the $4{\times}10^{-2}$ 25% SD-FEC threshold.

4.3.1 Experimental setup

Figure 4.7 illustrates the experimental setup and the DSP routine employed in the transmission experiment. Similar to the previous section, we generate a random sequence of QAM symbols using a Mersenne twister. To mitigate pattern-dependent nonlinearities in the received signal, we pre-distort the symbols using two lookup tables with a memory length of three. The signal is then filtered using a RRC filter at 2 sps and subsequently resampled to match the AWG

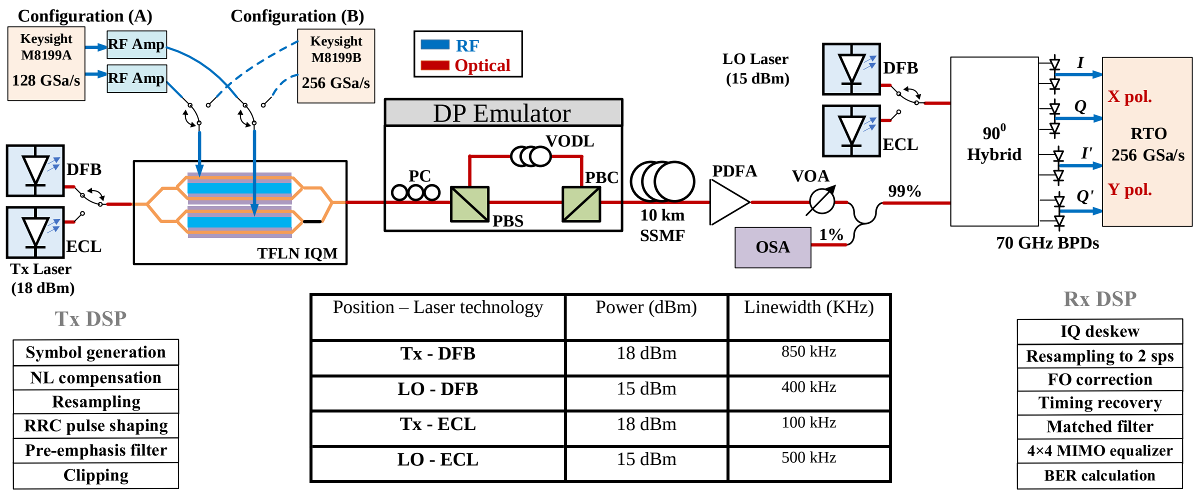

Position – Laser technology	Power (dBm)	Linewidth (KHz)
Tx - DFB	18 dBm	850 kHz
LO - DFB	15 dBm	400 kHz
Tx - ECL	18 dBm	100 kHz
LO - ECL	15 dBm	500 kHz

Figure 4.7. The experimental setup and DSP stacks employed. The inset shows the specifications of the two laser sets used in the experiments.

sampling rate. We pre-compensate the frequency response of the transmitter RF chain (up to the RF probe input) using the digital filters depicted in Figure 4.8(a). The impact of the pre-emphasis filter is observed on the received RF spectrum as depicted in Figure 4.8(b) for 120 Gbaud 64QAM signal transmitted using the 128 GSa/s transmitter configuration. Finally, we clip the signal to limit its PAPR to 9 dB and load it onto the AWG.

As shown in Figure 4.7, we evaluate the performance using two different transmitter configurations. Configuration (A) consists of a Keysight M8199A AWG (128 GSa/s) without interleaver, followed by an SHF 804 amplifier (22 dB gain and 60 GHz bandwidth), and connected with a 15 cm RF cable (1.85 mm connectors). Configuration (B) utilizes a Keysight M8199B AWG (256 GSa/s) with its internal RF driver, along with a 20 cm RF cable (1.0 mm connectors).

The pre-emphasis digital filters shown in Figure 4.8(a) are generated using a Keysight N1046A-11F 100 GHz digital communication analyzer (DCA), which indicates the inverse of the frequency response of each configuration. The rippled response observed for configuration (A) originates from the RF amplifier and the back reflections caused by cascading connectors. These ripples impose a burden on the receiver equalizer and necessitate the use of a larger number of filter taps to be properly compensated. On the other hand, configuration (B) benefits

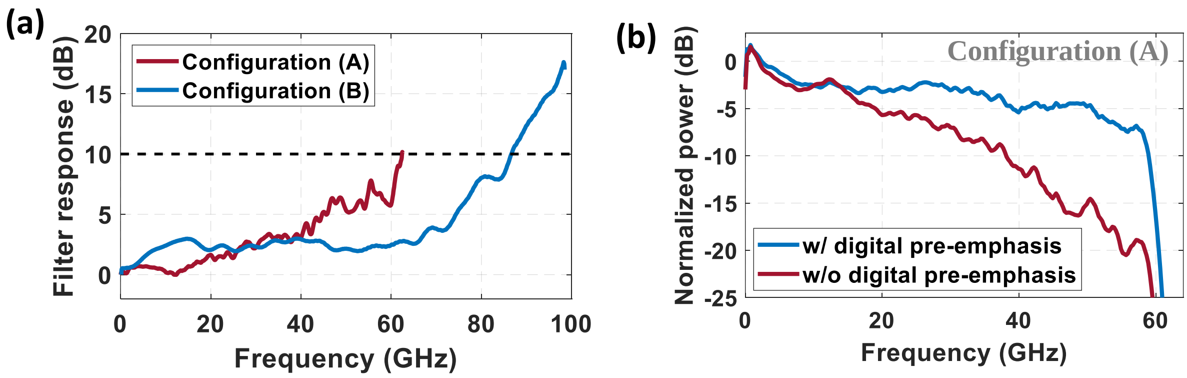

Figure 4.8. (a) The digital pre-emphasis filter used with each transmitter configuration (generated from the correction of their frequency response); and (b) the received RF spectra of a 120 Gbaud 64QAM signal.

from the integration of the driver with the DAC, resulting in a smoother response with a slower roll-off. To apply the RF signal to the TFLN IQ modulator, we use a 100 GHz GSG-GSG RF probe. Notably, the I and Q signals on the chip are separated by approximately 625 μm to minimize the RF crosstalk.

The transmitter uses a 1310 nm DFB laser with an output power of 18 dBm, a linewidth (Δv) of 850 kHz measured using the delayed self-homodyne method [109], and a side mode suppression ratio (SMSR) of 49 dB. The single-polarization TFLN IQ modulator has 18 mm coplanar electrodes, resulting in a fiber-to-fiber insertion loss of 10.5 dB, a 6-dB bandwidth of approximately 100 GHz, extinction ratio of 26 dB, and a low-MHz V_π of 1.7 V, as shown in Figure 4.9.

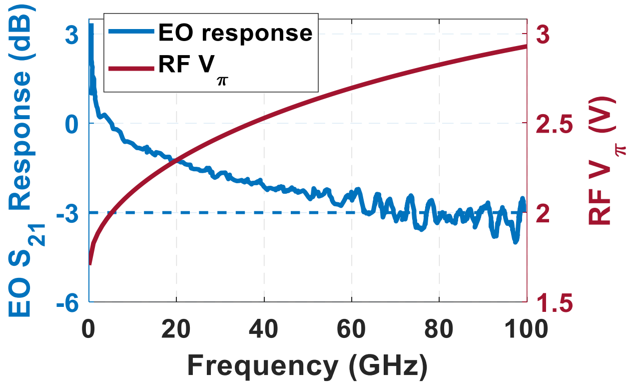

Figure 4.9. The electro-optic response of the TFLN modulator (normalized to 5 GHz) and RF V_π.

For dual-polarization (DP) transmission, a DP emulator is employed, consisting of a polarization controller and a polarization beam splitter (PBS) that split the optical signal into two orthogonal polarizations. One of the polarizations is then delayed by 9.2 ns using a variable optical delay line (VODL) to decorrelate both polarizations during receiver processing. The DP signal is subsequently transmitted over 10 km of SMF. To compensate for the lack of a TIA in our receiver, a PDFA is utilized. However, the optical link budget of the system supports operating without optical amplification if a TIA is used as in commercial transceivers. The ROP is controlled by a VOA located just before the DP optical hybrid. The other input of the hybrid is connected to another 1310 nm DFB laser, serving as LO, with an output power of 15 dBm, a linewidth of 400 kHz, and an SMSR of 54 dB, as shown in Figure 4.10(a-b). The outputs of the hybrid are connected to four balanced photodiodes with a bandwidth of 70 GHz, which is the main limitation of the system's bandwidth when configuration (B) is employed.

At the receiver, we initially deskew the signals for each polarization and then correct the frequency offset using the 4th-order method at 2 sps [110]. It is important to note that each DFB laser is equipped with its own thermoelectric cooler (TEC) controller, and they were very stable in the lab environment. Since we operate in the O-band with minimal chromatic dispersion, we do not require a dedicated DSP block for dispersion compensation. The receiver equalizer consists of a T/2-spaced 81-tap 4×4 MIMO equalizer with real coefficients, interleaved with a first-order PLL. We use the same Rx DSP for both transmitter configurations. The use of a real-valued MIMO equalizer provides significant benefits as it independently handles each quadrature of the signal. This approach effectively mitigates power imbalances and any remaining timing skew. Finally, the equalized symbols are mapped back to bits for BER calculations.

As shown in Figure 4.7, our experimental setup includes an additional set of ECLs with equivalent output power. These lasers are used to evaluate the penalty associated with employing DFB lasers, as discussed in the next section.

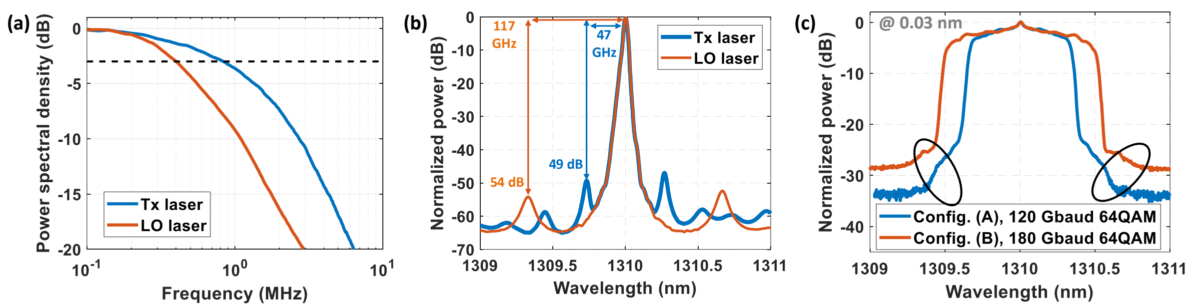

Figure 4.10. (a) The power spectral density of the two DFB lasers based on the self-homodyne measurement; (b) the optical spectra of each DFB laser without signal; and (c) the optical spectra at the input of optical hybrid of a 120 Gbaud and 180 Gbaud DP-64QAM.

4.3.2 Transmission experiment results

4.3.2.1 Configuration A: (128 GSa/s)

Here, we present the achieved transmission performance using configuration (A) of the transmitter, consisting of a 128 GSa/s DAC followed by a 22 dB RF amplifier. Figure 4.11(a) plots the BER versus symbol rate for different QAM formats after 10 km transmission. With this configuration, we successfully transmit 120 Gbaud DP-64QAM, achieving a BER below the 2.4×10^{-2} 20% overhead SF-FEC threshold, corresponding to a net capacity of 1.2 Tbps. A summary of the performance at the different FEC thresholds is provided in Table 4.1. In this configuration, the primary bandwidth limitation stems from the transmitter.

Figure 4.11(b) demonstrates the BER sensitivity to the ROP at the input of the optical hybrid for 120 Gbaud DP-64QAM. We compare the achieved BER using the DFB laser set with the ECL set to evaluate the penalty resulting from the linewidth (phase noise) difference. The transmitter ECL has 100 kHz linewidth, while the LO laser has 500 kHz linewidth; thus, the total linewidth of this configuration is 0.6 MHz compared to 1.25 MHz for the DFB set. Both sets exhibit similar behavior, with the BER limited by the analog-to-digital converter (ADC) noise below -4 dBm. However, as the ROP increases, the BER approaches a floor due to the dominance of PDFA ASE noise. At the 20% SD-FEC threshold, the gain of using ECLs is less

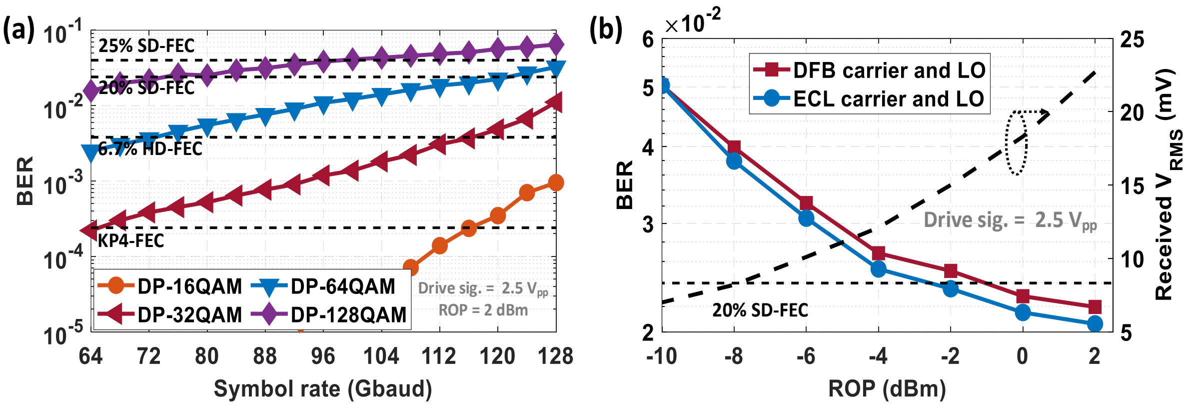

Figure 4.11. (a) BER versus the symbol rate after 10 km of SSMF using DFB lasers for both the carrier and the LO. (b) The BER sensitivity to the ROP as a function of laser type and the corresponding received RMS level.

than 1 dB, aligning with industry estimates and supporting the adoption of high-quality DFB lasers in short-reach coherent transponders [104].

Figure 4.12(a) shows the BER sensitivity to the driving voltage swing at the input of the RF probe, with and without nonlinear pre-compensation. The observed optimal driving swing is 2.5 V_{pp}, which is the 1 dB compression point of the SHF 804 RF amplifier. Owing to the low V_π (half-wave voltage) of TFLN, there is no need to drive the amplifier beyond its 1 dB point, resulting in improved linearity of the transmitted signal. We observe a marginal gain when employing nonlinear pre-compensation, as demonstrated in the constellations presented in Figure 4.12(b). The constellations for the X-pol of 120 Gbaud DP-64QAM and DP-32QAM appear linear and symmetric, indicating that the real-valued MIMO effectively mitigates any power imbalances between the I and Q quadratures.

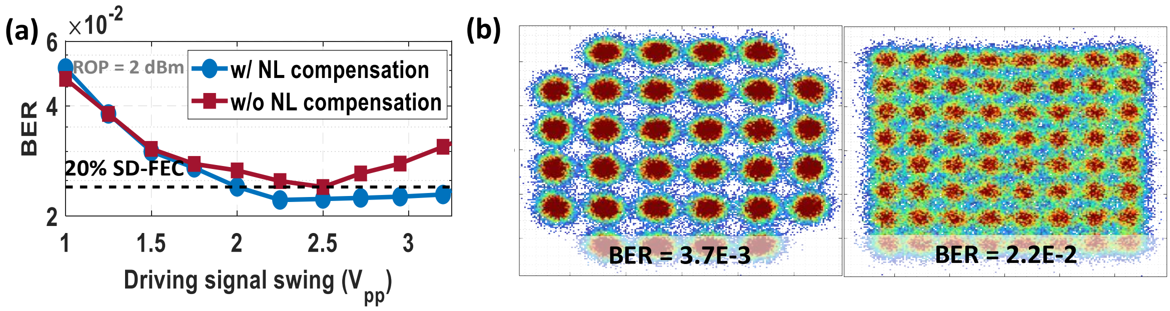

Figure 4.12. (a) BER of a 120 Gbuad DP-64QAM signal versus the IQM driving swing with and without nonlinear compensation. (b) The received constellations of one polarization of a 120 Gbaud DP-64QAM and a DP-32QAM signal.

Table 4.1. Summary of Net Bitrate Achieved After 10 km Transmission Using DFB Lasers

		Keysight M8199A (128 GSa/s) 1 DAC/quadrature		Keysight M8199B (256 GSa/s) 2 DACs/quadrature		
FEC threshold	**FEC overhead**	**Modulation format**	**Net (Tbps)**	**Modulation format**	**Net (Tbps)**	**Gain (%)**
2.4×10^{-4}	5%	116 Gbaud DP-16QAM	0.88	148 Gbaud DP-16QAM	1.12	27
3.8×10^{-3}	6.7%	116 Gbaud DP-32QAM	1.09	144 Gbaud DP-32QAM	1.35	24
2.4×10^{-2}	20%	120 Gbaud DP-64QAM	1.2	180 Gbaud DP-32QAM	1.5	25
4×10^{-2}	25%	128 Gbaud DP-64QAM	1.23	167 Gbaud DP-64QAM	1.6	30

4.2.2.2 Configuration B: (256 GSa/s)

To explore higher capacity limits and assess the advantages of next-generation DACs, we present the transmission performance achieved using configuration (B) of the transmitter. This configuration utilizes a 256 GSa/s DAC with a 6 dB bandwidth of 85 GHz and an output single-ended swing of 2.5 V_{pp}. In this setup, we only use DFB lasers. Figure 4.13 and Table 4.1 provide a summary of the BER performance for various QAM formats. We successfully transmit 167 Gbaud DP-64QAM over 10 km, achieving a BER below the 4×10^{-2} SD-FEC threshold. This demonstrates the first O-band transmission system capable of supporting a net capacity of 1.6 Tbps over a single fiber. Additionally, we transmit 180 Gbaud DP-32QAM below the 2.4×10^{-2} SD-FEC threshold, corresponding to net capacity 1.5 Tbps. This represents a 25% performance gain compared to configuration (A) at the same FEC threshold. The last column of Table 4.1 reports the net transmission rate gain achieved when this configuration is utilized compared to configuration (A) at the different FEC thresholds. It is fair to say that ~ 25% improvement is observed for this configuration. However, the actual gain is even higher, as configuration (B) is limited by the 70 GHz balanced photodiodes.

Figure 4.14(a) plots the received RF spectra with and without digital pre-emphasis for the 180 Gbaud 32QAM signal. This work solely relies on electronic equalization techniques,

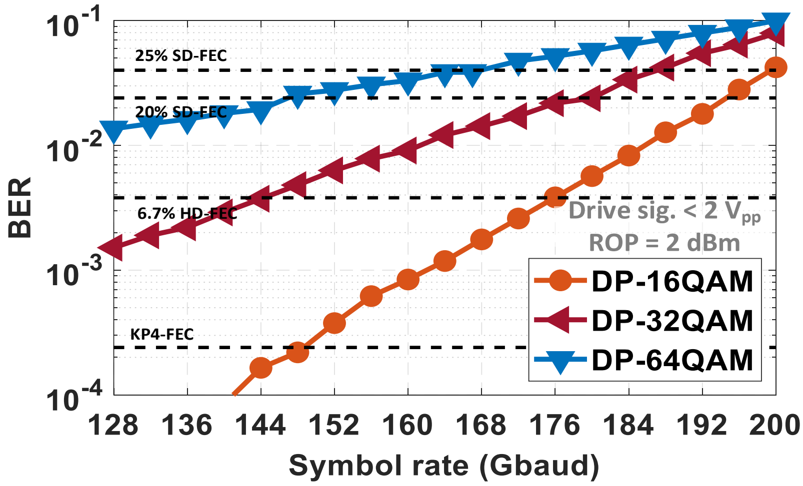

Figure 4.13. BER versus the symbol rate after 10 km of SSMF using DFB lasers for both the carrier and the

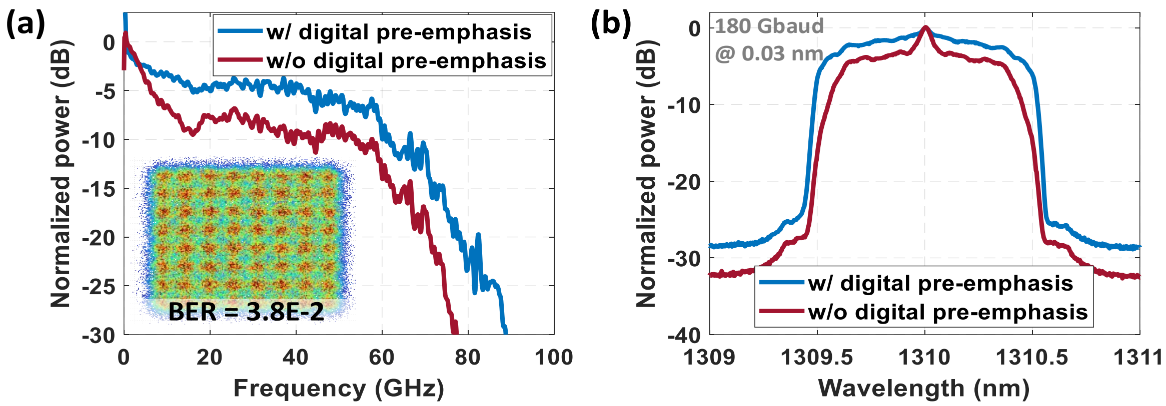

Figure 4.14. (a) The received RF spectra of 180 Gbaud 32QAM with and without digital pre-emphasis, with the inset showing the constellation of the X-pol of 167 Gbaud DP-64QAM. (b) The optical spectra of 180 Gbaud DP-32QAM signal after fiber transmission.

similar to those employed in practical networks, without the inclusion of optical shaping or optical equalization methods. The pre-emphasis filter compensates for the frequency response of the transmitter RF chain. Therefore, the uncompensated chain includes the 100 GHz RF probe, the TFLN modulator, the 70 GHz BPDs, and the 100 GHz ADCs. A ~20 dB drop at 80 GHz is observed, primarily attributed to the limited bandwidth of the BPDs. In alignment with this observation, the optical spectra of the 180 Gbaud DP-32QAM signals depicted in Figure 4.14(b) exhibit a flatter response up to the signal bandwidth. This suggests that the TFLN IQ modulator has the potential to support higher data rates if higher bandwidth photodiodes are used in the system.

4.4 Power Consumption Analysis

This section presents an analysis of the power consumption envelope for the key candidate architectures capable of achieving 1.6 Tbps transmission. The system architectures considered are as follows:

1) 8λ×200 Gbps WDM IMDD: This configuration utilizes silicon photonic (SiP) modulators, which are commonly utilized at these data rates [111].

2) 4λ×400 Gbps WDM IMDD: Compared to the 8×200 Gbps configuration, this configuration requires higher bandwidth modulators. In our analysis, we assume the use of TFLN technology to meet these requirements [85].

3) 2λ×800 Gbps WDM coherent transmission: This configuration utilizes SiP IQ modulators, as it is equivalent to 200 Gbps per quadrature [50].

4) 1λ×1.6 Tbps single-carrier coherent transmission: Based on the transmission performance demonstrated in the previous section, we assume it is realized using TFLN platform [12].

Each of these configurations presents its own set of technical challenges and hardware requirements. The power consumption analysis aims to provide insights into the relative energy efficiency of these options, allowing for a more comprehensive evaluation of their performance. Our analysis is based on publicly reported data from the literature on the power consumption of discrete components. However, it is important to note that power consumption can vary among different vendors due to variations in product features and characteristics. Therefore, we aim to provide a fair and objective comparison between the different architectures, without referring to a specific vendor or product.

Here is the common assumptions that we apply to all the configurations:

1) Operating Band and Distance: We assume that all configurations operate in the O-band and are evaluated for a transmission distance of 10 km.

2) DSP Engine: The DSP engine is assumed to support a fixed modulation format and symbol rate without employing geometric or probabilistic constellation shaping techniques.

3) RF Componentry Bandwidth: It is assumed that the performance of the RF componentry, such as RF drivers and TIAs, does not limit the overall system performance and evolves naturally with advancements in technology.

4) ASIC Process Node: The DSP engine is realized using the 5 nm process node.

These assumptions serve as the basis for the power consumption analysis and facilitate a fair comparison among the different architectures. The details of the calculations used to generate in Table 4.2.

Table 4.2. The Detailed Calculations and Assumptions Used in the Power Consumption Analysis

<table>
<tr><td>Arch.</td><td>8λ×200 Gbps WDM IMDD</td><td>4λ×400 Gbps WDM IMDD</td><td>2λ×800 Gbps WDM coherent transmission</td><td>1λ×1.6 Tbps single-carrier coherent transmission</td></tr>
<tr><td rowspan="2">Format</td><td>120 Gbaud PAM4</td><td>192 Gbaud PAM6</td><td>120 Gbaud DP-16QAM</td><td>192 Gbaud DP-32QAM</td></tr>
<tr><td colspan="4">• The assumed symbol rate and modulation formats leaves 20% margin for the FEC and switching overheads</td></tr>
<tr><td rowspan="3">FEC</td><td colspan="4">• It is envisioned that a stronger FEC like the C-FEC (14.8% overhead) will be used in the next-generation applications, which consumes 420 mW (7 nm process node) for 400 Gbps transceivers [112]. This corresponds to 420 mW for 60 Gbaud DP-16QAM.
• We assume that the power consumption of the FEC (digital circuit) module scales linearly with symbol rate.
• We assume a 20% power reduction when scaling from 7 nm to 5 nm process node.</td></tr>
<tr><td>420×(8/4)×(120/60)×0.8</td><td>420×(4/4)×(192/60)×0.8</td><td>420×(8/4)×(120/60)×0.8</td><td>420×(4/4)×(192/60)×0.8</td></tr>
<tr><td>P_{FEC} = 1.344 W</td><td>P_{FEC} = 1.075 W</td><td>P_{FEC} = 1.344 W</td><td>P_{FEC} = 1.075 W</td></tr>
<tr><td rowspan="3">Tx DSP including DAC</td><td colspan="4">• Ref. [113] demonstrated a CMOS (10 nm process node) DAC operating at 112 GSa/s with 8-tap feed-forward equalizer (FFE). That DAC has an output swing of 1 V_{pp} and consumes 432 mW.
• We assume the DAC power consumption scales linearly with the sampling rate as in [114].
• For calculations, we assume that the overall power consumption of this transmitter to be 600 mW, where the digital DSP blocks consumes 170 mW, and the analog part consumes the remaining 430 mW.
• Then we scale only the digital part by 20%×20% for moving from 10 nm to 5 nm process node.
• This is power consumption per lane or quadrature; thus, we scale it accordingly. The transmitter DSP for IMDD and coherent transmission are very similar; hence, we use the same calculations for both schemes.</td></tr>
<tr><td>(170×0.8×0.8+430)×(120/112) ×8</td><td>(170×0.8×0.8+430) ×(192/112) ×4</td><td>(170×0.8×0.8+430)×(120/112) ×8</td><td>(170×0.8×0.8+430)×(192/112) ×4</td></tr>
<tr><td>P_{Tx_ASIC} = 4.618 W</td><td>P_{Tx_ASIC} = 3.694 W</td><td>P_{Tx_ASIC} = 4.618 W</td><td>P_{Tx_ASIC} = 3.694 W</td></tr>
</table>

<table>
<tr>
<td rowspan="3">RF Driver</td>
<td colspan="4">

- For TFLN, the typical V_π of the MZM is 1.5 V; thus, operating without RF driver is feasible [115]. Yet, driving the TFLN IQM requires ~ 2 V_{pp} and an RF driver with 6-10 dB gain.
- The SiP MZMs has a typical V_π of 6 V [116], which requires 10-16 dB RF driver. For coherent transmission, we assume a 20 dB gain RF driver.
- Ref. [117] reported a 4-channel linear driver with 48 GHz bandwidth and 13-22.5 dB tuneable gain, which consumes 225 mW per channel and is realized with a 65 nm CMOS process.

</td>
</tr>
<tr>
<td>225×8</td>
<td>-</td>
<td>225×8</td>
<td>225×4</td>
</tr>
<tr>
<td>P_{Tx_driver} = 1.8 W</td>
<td>P_{Tx_driver} = 0 W</td>
<td>P_{Tx_driver} = 1.8 W</td>
<td>P_{Tx_driver} = 0.9 W</td>
</tr>
<tr>
<td rowspan="4">Laser</td>
<td colspan="4">

- Following [41],we calculate the optical power budget for each configuration and offset it relative to each other.
- The power consumption of a laser diode is given by $P_{LD} = V_{LD,f} I_{LD,driv}$; and $I_{LD,driv} = P_{LD,opt}/\gamma_{LD} + I_{LD,th}$. Where $V_{LD,f}$ is the diode bias voltage, $I_{LD,driv}$ is the diode current, $P_{LD,opt}$ is the optical power of the laser, γ_{LD} is the slope efficiency, and $I_{LD,th}$ is the threshold current.
- These parameters differ among vendors. A typical set of values are $V_{LD,f} = 1.6\,V, I_{LD,th} = 15\,mA, and\ \gamma_{LD} = 0.29\,mW/mA$ [118].

</td>
</tr>
<tr>
<td>Link budget:
• SiP chip IL = 8.5 dB (4 dB coupling and 4.5 dB MZM IL)
• Modulation loss = 3 dB
• Optical Mux/Demux IL = 4 dB
• 10 km fiber = 3.5 dB
• 8-channel implementation = -9 dB (It is a gain in the link budget as we calculate the power required per laser)</td>
<td>Link budget:
• TFLN chip IL = 6 dB (4 dB coupling and 2 dB MZM IL)
• Modulation loss = 3 dB
• Optical Mux/Demux IL = 4 dB
• 10 km fiber = 3.5 dB
• Rx chip IL = 2 dB
• The OSNR penalty (Relative to 120 Gbaud PAM4) = 8.2 dB
• 4-channel implementation = -6 dB</td>
<td>Link budget:
• SiP chip IL = 12 dB (4 dB coupling, 6 dB DP IQM, and 2 dB for the optical hybrid)
• Modulation loss = 12 dB (because of the high V_π)
• Optical Mux/Demux IL = 4 dB
• 10 km fiber = 3.5 dB
• 2-channel implementation = -3 dB</td>
<td>Link budget:
• TFLN chip IL = 7.5 dB (4 dB coupling and 3.5 dB DP IQM)
• Modulation loss = 8 dB (for linear performance)
• 10 km fiber = 3.5 dB
• Rx chip IL = 4 dB (including the hybrid)
• The OSNR penalty (Relative to 120 Gbaud PAM4) = 8.2 dB</td>
</tr>
<tr>
<td>Total link budget = 10 dB</td>
<td>Total link budget = 20.7 dB</td>
<td>Total link budget = 28.5 dB</td>
<td>Total link budget = 31.2 dB</td>
</tr>
<tr>
<td colspan="4">

- Based on the total link budget, we assume that the 1×1.6 Tbps configuration will use a 23 dBm laser source and scale the other configurations according to the number of lasers needed and their projected optical power.

</td>
</tr>
</table>

<table>
<tr><td rowspan="2"></td><td>Laser power = 1.8 dBm
$P_{LD} = 32.5\ mW$</td><td>Laser power =12.5 dBm
$P_{LD} = 122\ mW$</td><td>Laser power =20.3 dBm
$P_{LD} = 615\ mW$</td><td>Laser power = 23 dBm
$P_{LD} = 1127\ mW$</td></tr>
<tr><td>P_{laser} = 0.0325×8 = 0.26 W</td><td>P_{laser} = 0.122×4 = 0.49 W</td><td>P_{laser} = 0.615×2 = 1.23 W</td><td>P_{laser} = 1.127 W</td></tr>
<tr><td rowspan="3">TEC controller</td><td colspan="4">• IMDD systems do not necessarily require the use of a thermoelectric cooler (TEC) when a wide-spacing WDM grid is adopted. However, the edge channels may experience severe chromatic dispersion, especially in the 4×400 Gbps configuration. Thus, the 4×400 Gbps requires smaller spacing in the WDM grid and more accurate control over their wavelengths. Accordingly, we assume that the 4×400 Gbps IMDD solution employs a TEC similar to coherent architectures.
• Based on [119], the TEC consumes ~ 1200 mW.</td></tr>
<tr><td>-</td><td>1200×4</td><td>1200×2</td><td>1200×1</td></tr>
<tr><td>P_{TEC} = 0 W</td><td>P_{TEC} = 4.8 W</td><td>P_{TEC} = 2.4 W</td><td>P_{TEC} = 1.2 W</td></tr>
<tr><td rowspan="3">Modulator</td><td colspan="4">• We assume that a series push pull (SPP) MZM / IQM is used, and the driving swing depends on the architecture and modulator platform.
• For IMDD, the power consumption in the modulator is given by $P_{modulator} = P_{MZM} + P_{\pi,TPS}/2$, where P_{MZM} is the power consumed in the RF termination and equals $P_{MZM} = V_{rms}^2/R$ with R typically 50 Ω. $P_{\pi,TPS}$ is the power consumed by the thermal phase shifter to induce a phase-shift of π.
• For coherent transmission, there are 4 MZMs in the DP IQM. Thus, it consumes $P_{total} = 4 \times P_{MZM} + 5 \times P_{\pi,TPS}$
• $P_{\pi,TPS} =$ 30 mW</td></tr>
<tr><td>• For SiP IMDD [116],
V_{rms} = 1 V
(1^2/50 +0.015)×8</td><td>• For TFLN IMDD [115],
V_{rms} = 0.35 V
(0.35^2/50 +0.015)×4</td><td>• For SiP coherent [116],
V_{rms} = 2.12 V
(4× (2.12^2/50) +5×0.03)×2</td><td>• For TFLN coherent [12],
V_{rms} = 0.7 V
(4× (0.7^2/50) +5×0.03)</td></tr>
<tr><td>$P_{modulator}$ = 0.28 W</td><td>$P_{modulator}$ = 0.07 W</td><td>$P_{modulator}$ = 1 W</td><td>$P_{modulator}$ = 0.19 W</td></tr>
<tr><td rowspan="2">PD</td><td colspan="4">• PDs consume negligible power under reverse bias, typically 2 mW per PD.</td></tr>
<tr><td>P_{PD} = 0.016 W</td><td>P_{PD} = 0.008 W</td><td>P_{PD} = 0.032 W</td><td>P_{PD} = 0.016 W</td></tr>
<tr><td rowspan="3">TIA</td><td colspan="4">• In [120], the authors demonstrated a 60 GHz single-ended TIA that consumes 107 mW and is realized with 28 nm CMOS process.
• The TIA power consumption does not depend on the architecture. It depends on the receiver sensitivity and required gain, which are assumed to be the same for the different configurations.</td></tr>
<tr><td>(107)×8</td><td>(107)×4</td><td>(107)×8</td><td>(107)×4</td></tr>
<tr><td>P_{TIA}= 0.856 W</td><td>P_{TIA}= 0.428 W</td><td>P_{TIA}= 0.856 W</td><td>P_{TIA}= 0.428 W</td></tr>
</table>

<table>
<tr><td rowspan="3">Rx DSP including ADC</td><td colspan="4">

- The receiver DSP for IMDD and coherent transmission are different. Based on [41], the power consumption of the coherent DSP is 1.6× (60% higher) that of IMDD at the same symbol rate. This included the power consumption of the chromatic dispersion compensation module, which is actually not needed since we operate in the O-band.
- Ref. [121] reported a CMOS (5 nm process node) SerDes receiver, which is composed of a 112 GSa/s ADC and 16 tap FFE. The analog circuit consumes 315 mW and we assume that the digital part consumes additional 185 mW.
- We assume that the power consumption of the ADC and DSP scales linearly with symbol rate.

</td></tr>
<tr><td>500×(120/112)×8</td><td>500×(192/112)×4</td><td>(185×1.6+315)×(120/112)×8</td><td>(185×1.6+315)×(192/112)×4</td></tr>
<tr><td>P_{Rx_ASIC} = 4.285 W</td><td>P_{Rx_ASIC} = 3.428 W</td><td>P_{Rx_ASIC} = 5.237 W</td><td>P_{Rx_ASIC} = 4.19 W</td></tr>
<tr><td rowspan="2">Total power</td><td colspan="4">

- The calculated power is not the power of the entire optical transceiver pluggable module, as we do not include the central processing unit (CPU) power consumption, Ethernet framer and mapper, and the microcontroller for interfacing. In addition, we did not include the DC/DC power conversion efficiency. The power consumption of these units is almost independent of the optical transceiver architecture; hence, we exclude it from the discussion.
- There should be some resource sharing between modules if multiples components are integrated together; however, this value is hard to estimate from the public literature. Hence, resource sharing is not accounted for in the analysis.
- It is worth noting that this is a best-case (conservative) estimate, which cannot be directly compared with what vendors report.

</td></tr>
<tr><td>P_{total} = 13.5 W</td><td>P_{total} = 14 W</td><td>P_{total} = 18.5 W</td><td>P_{total} = 12.82 W</td></tr>
</table>

Table 4.3. The Hardware Requirements for the Different Architectures

Architecture	8λ×200 Gbps WDM IMDD	4λ×400 Gbps WDM IMDD	2λ×800 Gbps WDM coherent transmission	1λ×1.6 Tbps single-carrier coherent transmission
Lasers	8	4	2	1
TECs	-	4	2	1
MZMs	8	4	8 (2 DP IQMs)	4 (1 DP IQMs)
Optical Mux/Demux	1	1	1	-

RF Drivers	8	-	8	4
DACs	8	4	8	4
ADCs	8	4	8	4
PDs	8	4	8	4
TIAs	8	4	8	4
ASIC DSP	1	1	1	1
Optical hybrid	-	-	2	1
Total hardware count (#)	58	30	56	28

As detailed in the Table 4.2, Figure 4.15(a) provides the breakdown of power consumption for the various architectures, along with the overall consumption given in Figure 4.15(b). It is worth noting that this is not the total power of the entire pluggable optical transceiver module. This is because we are specifically referring to the power consumed by the optical and RF components and not taking into account other components present in the module, which have similar power requirements regardless of the architecture. These additional components include the central processing unit (CPU), Ethernet framer and mapper, and the microcontroller used for interfacing. Furthermore, the analysis presented here does not consider the finite DC/DC power conversion efficiency as it does not depend on the transceiver architecture.

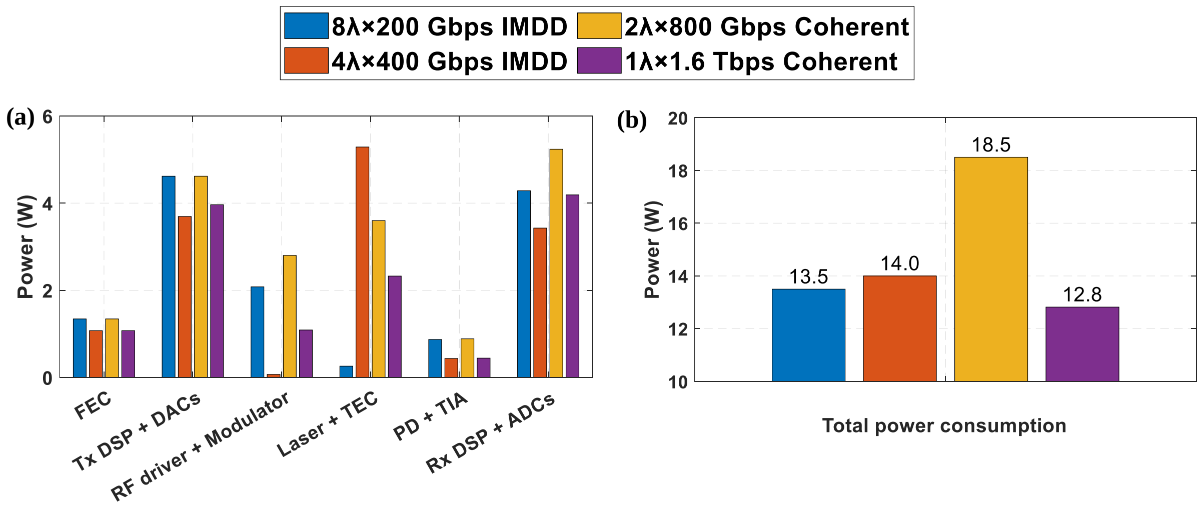

Figure 4.15. (a) The power consumption breakdown and (b) the calculated total power (excluding the common central processing unit) for the candidate architectures for 1.6 Tbps operation.

In all four architectures, the main consumption comes from the DSP and DAC/ADCs with over 50% of the total power consumption, with the 4λ×400 Gbps IMDD proposal exhibiting the lowest power consumption in this respect as shown in Figure 4.16. This same architecture is, notwithstanding, the least efficient in terms of the power required to operate the TECs, resulting in a total power consumption of 14 W. By operating at a lower symbol rate and doubling the optical channel count, it becomes possible to mitigate the impairments caused by chromatic dispersion and eliminate the requirement for precise wavelength control using TECs. As a result, the 8λ×200 Gbps IMDD architecture becomes more power-efficient when compared to the 4λ×400 Gbps architecture. Considering the implementation challenges associated with the 4λ×400 Gbps IMDD architecture, as discussed in Chapter 3, and its higher power consumption, the 8λ×200 Gbps architecture seems to be a more sensible solution within the IMDD realm.

The 2λ×800 Gbps coherent architecture consumes 40% more power compared to the single carrier 1.6 Tbps architecture. This increased power consumption can be attributed to the higher driving voltage requirements for SiP technology and the doubling of hardware components, as demonstrated in Table 4.3. On the other hand, our analysis reveals that the 1λ×1.6 Tbps TFLN-based coherent solution exhibits the lowest power consumption, requiring less than 13 W. This low power consumption envelope is attributed to the simpler architecture and inherent disparities between SiP and TFLN platforms, which makes it highly competitive, even when compared to IMDD architectures. Furthermore, this architecture has the lowest hardware requirements, as indicated in Table 4.3, which directly translates to a smaller transceiver footprint.

The low power consumption and small footprint suggest that the 1λ×1.6 Tbps TFLN-based coherent architecture can be realized with the current state-of-the-art small form-factor

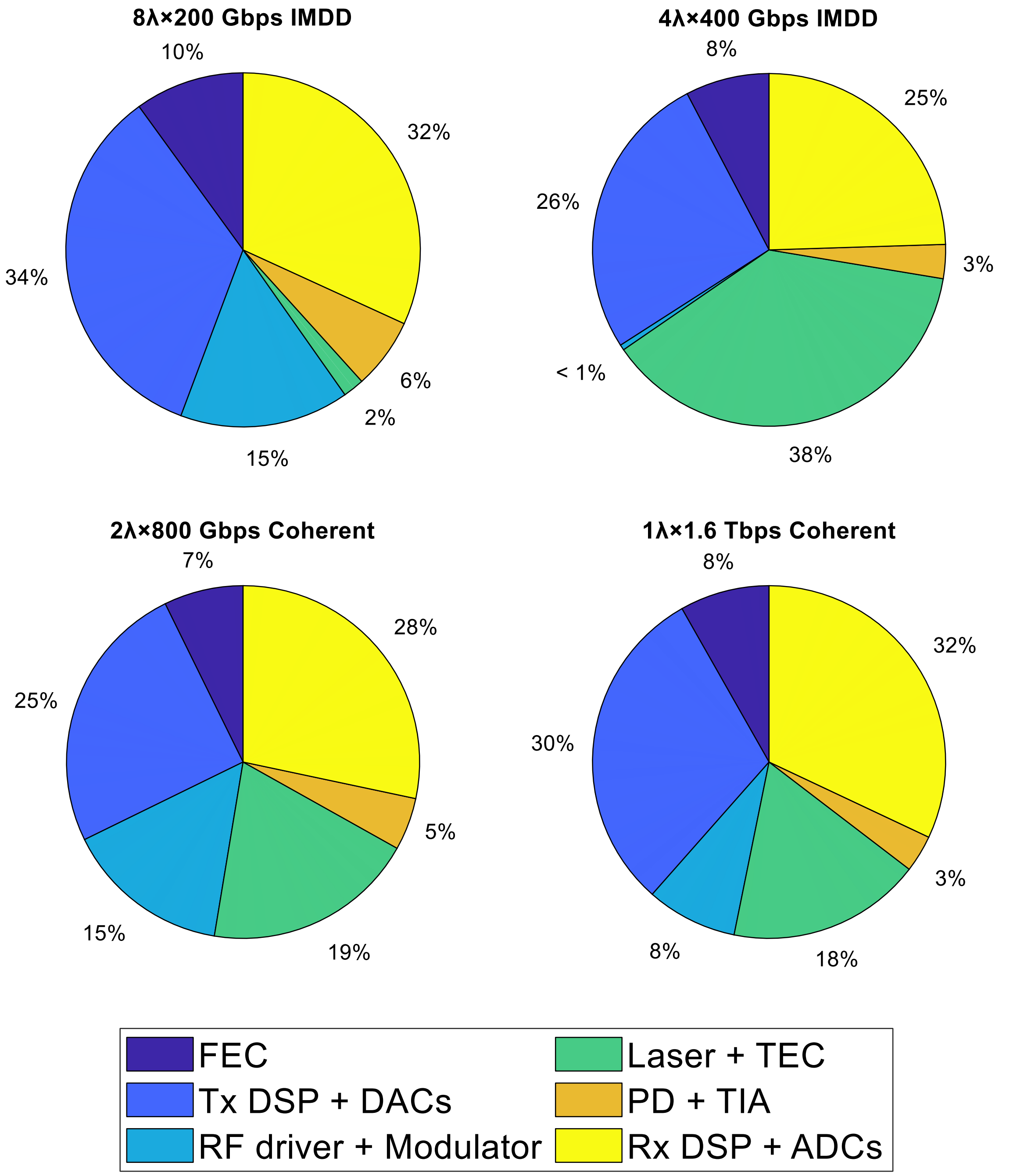

Figure 4.16. The power consumption distribution for each configuration.

pluggable (SSFP) modules. This result, together with its feasibility (demonstrated in the previous section), strongly supports our proposition to consider TFLN-based single-carrier coherent transmission as the main contender for the deployment of next-generation 1.6 Tbps intra-datacenter interconnects.

Chapter 5

SiP Coherent Transmitters for 800 Gbps/λ Inter-Datacenter and Long-Haul Networks

5.1 Overview

The growing data traffic demand is mandating the increase in optical communication networks' capacity. Therefore, the Optical Internetworking Forum (OIF) has defined the specifications of the 800 Gbps coherent optical communication interfaces [48]. Currently, 400ZR coherent interfaces are based on 60 Gbaud dual-polarization (DP) 16 QAM format. However, realizing 800 Gbps using 16QAM requires operating at 120 Gbaud, which challenges the bandwidth the electro-optic components. Thus, 96 Gbaud DP-32QAM and probabilistically shaped (PS) 100 Gbaud DP-64QAM are also potential candidates for the 800 Gbps networks as they relax the bandwidth restrictions [40, 63]. Yet, the majority of vendors prefers 120 Gbaud 16QAM due to the lower SNR requirements. Increasing the QAM order needs driving electronics with higher effective number of bits (ENoB) and higher driving swings, and PS adds considerable load on the ASIC power consumption. Therefore, these different candidate modulation formats are being researched extensively to address these trade-offs.

5.2 Silicon photonic single-segment IQ modulator for net 1 Tbps/λ transmission using all-electronic equalization [122]

The SiP platform has numerous advantages such as low fabrication costs, CMOS compatibility, high yield, and the small form factor. However, it poses challenges in terms of the relatively limited electro-optic bandwidth and the high driving voltage requirements. The continuous increase in the bandwidth of the DACs and the RF componentry is progressively pushing the limits of what can be achieved using SiP modulators.

Recent years have witnessed several high-speed demonstrations using SiP IQ modulators. The transmission of 116 Gbaud 64QAM at a BER of 5×10^{-2} below the 25% overhead SD-FEC threshold on a single polarization using a dual equal-length segmented SiP has been reported, corresponding to a net rate of 556.8 Gbps [123]. Using adaptive iterative nonlinear pre-distortion, joint electrical-optical pre-compensation, and DP emulation, the authors extended their results and transmit 116 Gbaud DP-64QAM under the 5×10^{-2} SD-FEC threshold using the segmented IQ modulator, which corresponds to a net rate of 1.07 Tbps [124]. To realize higher-bandwidth operation, segmented electrode designs are employed instead of the conventional single-segment traveling-wave (TW) MZM electrodes as it reduces the microwave losses and improves the electro-optic bandwidth [125, 126]. However, the number of transmitter RF components scales with the number of electrode segments, which increases cost, power consumption, and packaging complexity. For instance, matching the timing and power of two RF signals is a lot easier than matching four signals. Besides, the optical pre-compensation requires optical filtering with waveshapers, band-pass filters, and additional

EDFAs to compensate for their losses; which is impractical. Practically, single-segment IQMs and all-electronic pre-compensation are desired, as they do not alter or introduce extra overheads to the fiber-optic transmission network.

This work presents the design and characterization of two SiP IQ modulators with different phase-shifter lengths. Both devices are tested in the C-band at B2B and after 80 km of SSMF. We examine the IQMs performance considering different QAM orders and at high symbol rates using the current generation of 128 GSa/s AWGs. Additionally, we highlight the design trade-offs and analyze the difference in the performance of the two IQMs. Furthermore, we demonstrate the transmission of 105 Gbaud DP-64QAM using the longer IQ modulator and all-electronic equalization over 80 km of SSMF under the 5×10^{-2} BER threshold of the 25% overhead SD-FEC; featuring the first net 1 Tbps (line rate of 1.26 Tbps) demonstration using a single-segment SiP IQ modulator.

5.2.1 Modulators design and characterization

This section presents the design and characterization of the fabricated IQMs. The SiP modulators were fabricated through CMC Microsystem in a multi-project wafer (MPW) run at the Advanced Micro Foundry (AMF), which uses a conventional CMOS-compatible process flow. As depicted in Figure 5.1(a), AMF's silicon-on-insulator (SOI) process employs a 220 nm thick silicon layer with 2 μm buried oxide. The IQM is composed of two parallelly connected child TW-MZMs. Each of the child MZMs requires a single RF signal; as it is a single segment MZM with the PN junctions designed for series push-pull (SPP) driving configuration [127]. The traveling-wave electrodes of each MZM are terminated with an on-chip 50 Ω termination (OCT) for optimal power transfer and ease of testing. The arms of the parent MZM are 305 μm apart, which minimizes the crosstalk between the I and Q quadratures. Both the child and parent MZMs are balanced, such that both arms of each MZM have the

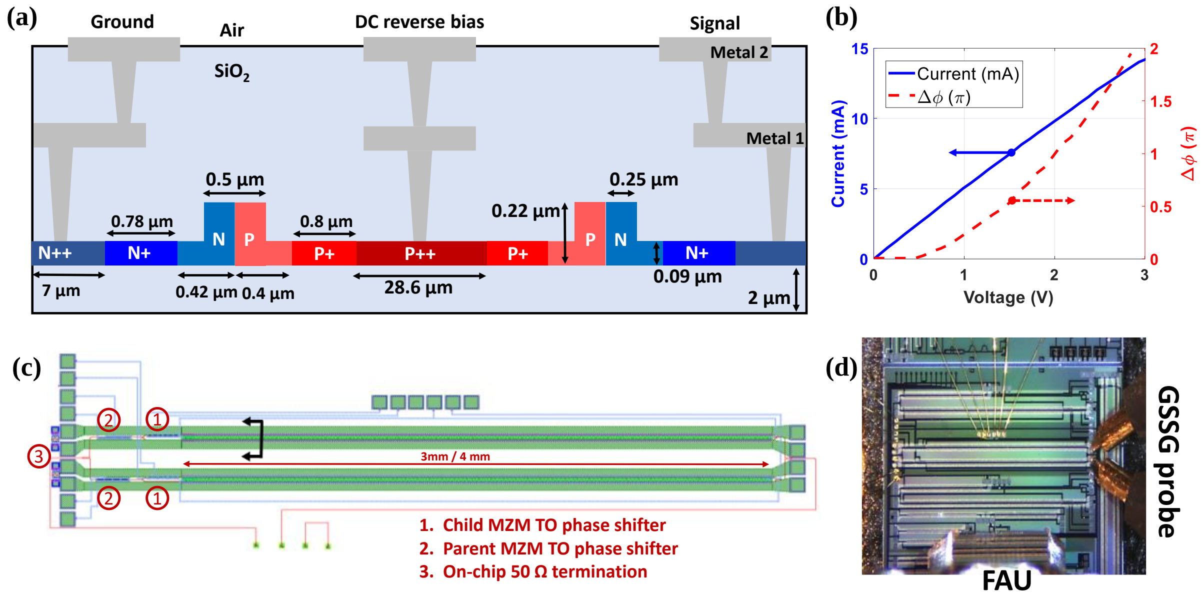

Figure 5.1. Cross-sectional illustration of the child MZM structure (not to scale). (b) The IV and the phase-change (ΔΦ) versus voltage curves of the MZM's thermo-optic tuners. (c) The schematic of the IQM. (d) Top view of the wirebonded chip showing the position of the fiber array unit (FAU) and the RF probe.

same length. Thus, the structure employs 4 thermo-optic (TO) heaters for biasing the IQM. The child MZMs' TO phase shifters set both MZMs at null and one of the parent TO phase shifters is used to induce 90^0 phase shift between the outputs of the child MZMs. The last TO phase shifter is left unbiased and only added to the design so that the propagation loss of the I and Q paths are matched; hence, maximize the extinction ratio [44].

As aforementioned, this work evaluates the performance of two IQMs that have the same structure but differ only in the phase shifter length and filling factor: (1) short IQM with 3 mm phase shifters at 90% fill factor, and (2) long IQM with 4 mm phase shifters at 85% fill factor. The added undoped (intrinsic) sections reduce the effective phase shifter length; however, it prevents the flow of electric currents through the optical waveguides. The cross-sectional view of one of the child MZMs is depicted in Figure 5.1(a). The rib waveguide width is 0.5 µm for nearly single-mode propagation across the C-band, and the width of the P, P+, P++, N, N+, and N++ regions are optimized through simulations to address the trade-off between minimizing the optical propagation loss and increasing the junction capacitance. The SPP configuration connects the two PN junctions in series, which halves the junction capacitance and increases the series resistance. The lower junction capacitance reduces the microwave losses and effectively improves the IQM bandwidth. The reverse DC bias is applied through a high-inductance line so that the RF and DC are separated. The complete design procedure of the employed TW-MZM coplanar strip electrodes is presented in [127]. The foundry process flow uses a 2 μm thick aluminum layer for metallization. As in [127], the width and separation between MZM electrodes are set to 36 μm and 60 μm, respectively. These values ensure that each of the electrodes has a 50 Ω characteristic impedance, besides ensuring a good velocity matching between the optical and RF signal. The OCTs are designed based on highly doped N++ silicon that results in 50 Ω resistances. The IQM layout and an image of the wire-bonded chip marking the position of the fiber array unit (FAU) and the RF GSSG probe are shown in Figure 5.1(c-d). The employed TO phase shifter is described in [128], which is composed of parallelly connected resistors for power-efficient operation. These resistors are highly doped N++ silicon slabs surrounding the undoped optical rib waveguide. The measured IV characteristics and the phase-change (ΔΦ) versus voltage of one of the phase shifters are given in Figure 5.1(b). The IV curve is not perfectly linear as its slope decreases at high voltage. The TO phase shifter requires 2 V to induce a π phase shift.

The measured DC V_π at 0 V reverse bias for the short and long designs are 12 V and 8.5 V, and the corresponding phase-shifting ($V_\pi L$) inverse efficiencies are 3.6 V.cm and 3.4 V.cm, respectively. The V_π of the IQMs can be almost halved if dual-drive IQM structure is adopted; however, it would require differential driving with four RF amplifiers. Alternatively, employing an L-shaped PN junction instead of the lateral junction can improve the phase-shifting efficiency and reduce the V_π. Figure 5.2 show the small-signal response of both IQMs for one of the child MZMs. Figure 5.2(a) shows that the short modulator has a 3-dB bandwidth of 27.5 GHz without reverse biasing and increases to 38 GHz at 3 V reverse bias, while the 6-dB bandwidth at 3 V is more than 50 GHz. Figure 5.2(b) shows that the longer design has a lower 3-dB bandwidth of 20 GHz at 0 V reverse bias that reaches 28 GHz at 3 V. Both IQMs have a slow roll-off frequency response, which allows operating at high symbol rates as shown in the next sections. For both IQMs, the electrical S_{11} is below -10 dB up to 50 GHz; highlighting the good design of the traveling wave electrodes and the good impedance matching between the fabricated electrodes and the OCTs. Optically, the IQMs are connected to vertical grating couplers (VGCs) for light coupling. The back-to-back coupling loss is 11 dB (5.5 dB/GC); employing edge couplers (1.5 dB/facet) can reduce the losses and lead to better transmission performance. Excluding GCs and routing losses, the measured insertion loss for the short and long IQMs is 3.5 dB and 4.5 dB, respectively.

Increasing the IQM reverse bias decreases its optical propagation losses and increases its EO bandwidth; however, it increases its V_π resulting in higher modulation loss [129]. The measured DC V_π and EO bandwidth at different reverse bias levels of the long IQM are shown in Figure 5.3. There is a trade-off between increasing IQM bandwidth and reducing its V_π. In our case, the performance is limited by the IQMs high V_π; thus, low reverse bias voltages yielded the optimum performance for both IQMs.

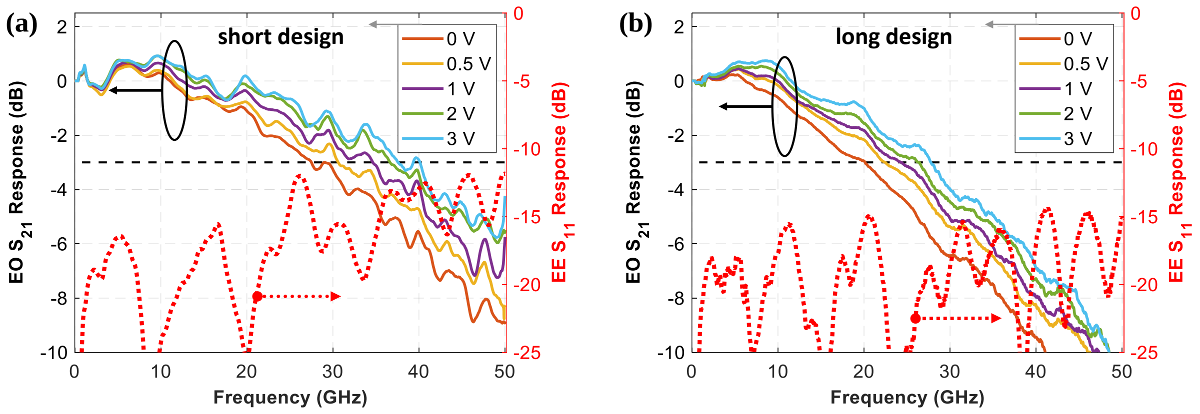

Figure 5.2. The electro-optic S21 and electrical S11 (0 V) measurements for (a) the 3 mm (short) IQM and (b) the 4 mm (long) IQM.

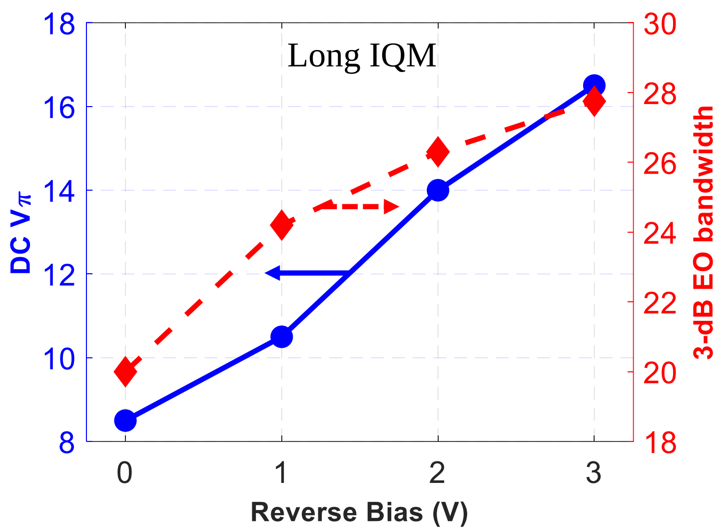

Figure 5.3. Measured DC V_π and 3-dB EO bandwidth versus reverse bias voltage for the long IQM.

5.2.2 Experimental setup and digital signal processing

Figure 5.4 shows the experimental setup and the DSP routine employed for testing the IQMs. The description follows the previous Chapter. The inset of Figure 5.4 shows the frequency response of the pre-emphasis digital filters, which pre-compensate the RF chain including the AWG (DAC) operating at 128 GSa/s and 26 dB gain 42-GHz RF amplifier (SHF 806e). The 10-dB point is around 51 GHz. We used a higher swing from AWG for the I channel to match the SNR and driving voltage after the RF amplifier; which can be attributed to the slightly different frequency response of the RF amplifiers and the pre-compensation filters. The precise pre-compensation of the frequency response of the transmitter RF chain alleviate all the bandwidth limitations in the system except for the SiP IQM, which is equalized at the receiver.

Optically, an ECL operating at 1550 nm with 15.5 dBm optical power and less than 100 kHz linewidth feeds the IQM. A tunable-gain EDFA is used to compensate for the GCs losses and boost the signal before the coherent receiver. Both IQMs are tested at B2B and after 80 km transmission. For the 80 km case, another EDFA is used to compensate for the 16 dB fiber loss. The transmitted signal is then coupled with an amplified spontaneous emission (ASE) noise signal using a 3-dB coupler. The ASE noise source is followed by a VOA to control the OSNR

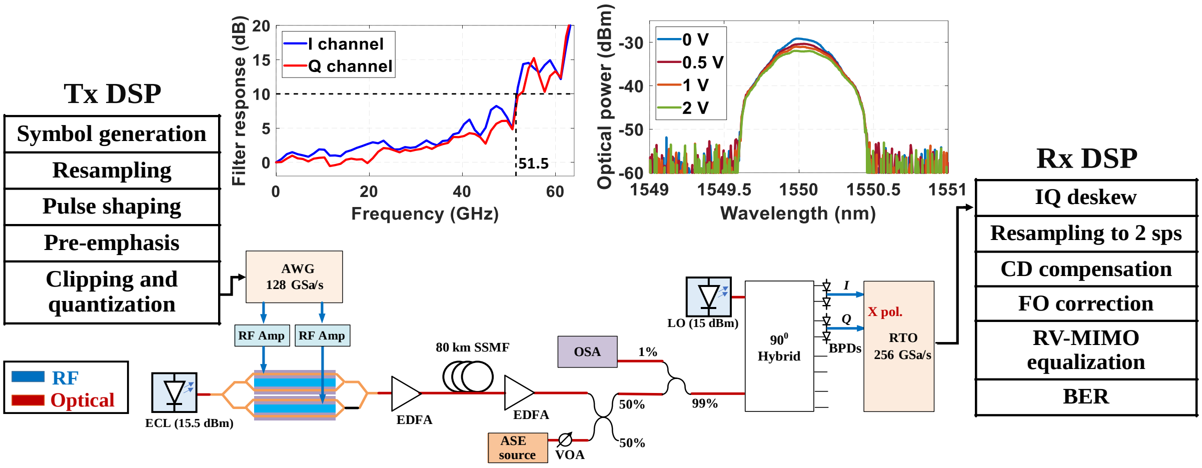

Figure 5.4. The experimental setup and the DSP routine employed. The insets show the pre-compensation filter response for both I and Q channels (Left), and the optical spectra of 100 Gbaud 32QAM signals at different reverse bias levels using the long IQM at 0.05 nm resolution (Right).

of the signal fed to the coherent receiver for OSNR sensitivity measurements. We used a 2×8 dual-polarization optical hybrid for both single and DP measurements. Another ECL operating at 1550 nm with 15 dBm power is used as LO; with effectively 12 dBm mixed with each polarization. The outputs of the optical hybrid are detected by 70 GHz balanced photodiodes followed by a 256 GSa/s RTO with a 64 GHz brick-wall filter. The received signals are then processed offline.

The inset of Figure 5.4 shows the optical spectrum measured at 0.05 nm resolution of 100 Gbaud 32QAM signals using the long IQM at different reverse bias levels. The increase in reverse bias increases V_π and decreases the modulation depth ($V_{modulation}/2V_\pi$), leading to higher modulation loss and lower OSNR.

5.2.3 Transmission experiment results

The performance of the short and long IQMs is investigated by transmitting different QAM orders at different symbol rates at B2B and 80 km of SSMF. The AWG output voltage, pulse shaping roll-off factor, and transmitter clipping ratio are optimized simultaneously at each symbol rate to achieve the lowest BER. In the subsequent sections, the single-polarization transmission experiment results are reported separately for each IQM. Then, we employ a DP emulator to determine the attainable transmission rate on a single optical carrier.

5.2.3.1 Short IQM (Single Polarization)

This section summarizes the transmission experiment results obtained using the short (3 mm) IQM. The IQM is reverse biased at 0.5 V, which corresponds to 30.5 GHz 3-dB bandwidth and minimizes the BER. The BER performance after 80 km of SSMF is shown in Figure 5.5(a) for different QAM orders. At line rates below 430 Gbps, 16QAM outperforms the other modulation formats because of its lower OSNR requirements. However, 32QAM performs better than 16QAM for the higher line rates due to the bandwidth limitations primarily from the SiP IQM and the RF amplifiers. Although the transmitter pre-emphasis filters pre-compensate the signal spectrum up to 64 GHz, the strong equalization after 50 GHz diminishes the AWG output signal swing; resulting in worse RF signal quality, smaller driving swing, higher modulation loss, and lower OSNR [106]. The summary of the achieved transmission rates is tabulated in Table 5.1, considering different FEC thresholds. We considered 4 FEC

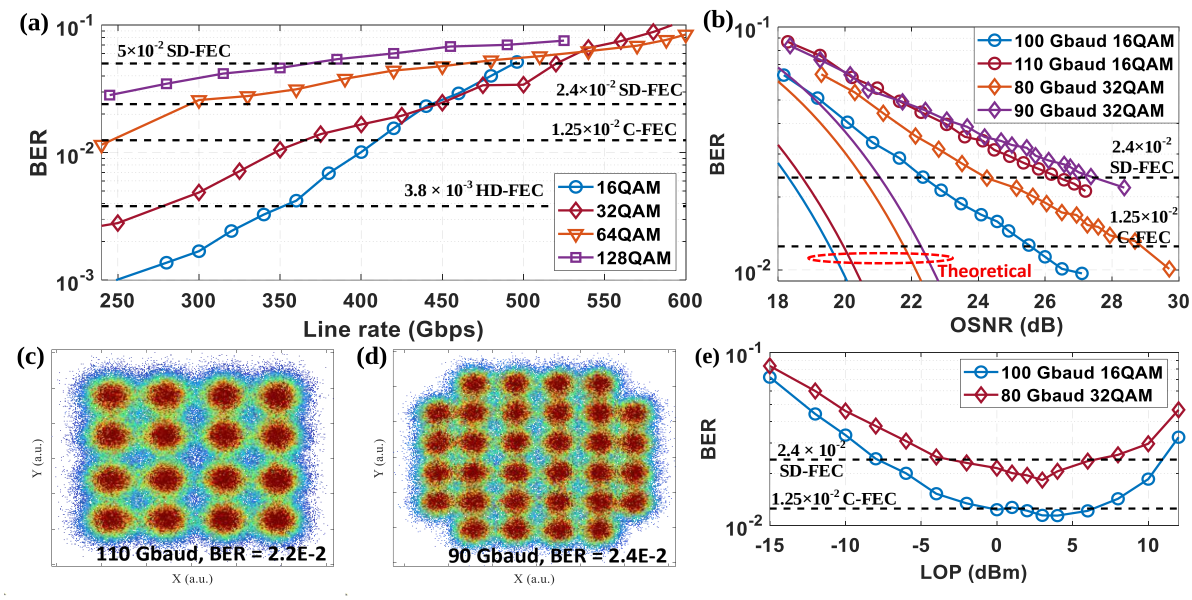

Figure 5.5. (a) BER versus line rate for different QAM orders after 80 km transmission using the short IQM. (b) The OSNR performance at 0.1 nm. Recovered constellation for (c) 110 Gbaud 16QAM and (d) 90 Gbaud 32QAM. (e) BER versus LOP for 80 km transmission.

thresholds based on the literature: (1) the 6.7% HD- FEC with a BER threshold of 3.8×10^{-3}, (2) the 14.8% concatenated FEC (C-FEC) standardized for 400ZR with a BER threshold of 1.25×10^{-2} [18], (3) the 20% SD-FEC at a threshold BER of 2.4×10^{-2} [130], and (4) the 25% SD-FEC with a BER threshold of 5×10^{-2} [124].

Figure 5.5(b) shows the OSNR performance of 16QAM and 32QAM at selected symbol rates after 80 km transmission. Compared to the theoretical OSNR performance and at the 2.4×10^{-2} SD-FEC threshold, the OSNR implementation penalty increases from 4 dB at 100 Gbaud 16QAM to 7.8 dB at 110 Gbaud 16QAM; a similar trend is observed for 32QAM. This increase in OSNR penalty with symbol rate is due to the lower ENoB of the AWG at higher symbol rates and the reduced signal fidelity with the stronger pre-emphasis, which adds more electrical noise from the transmitter side. Besides, the equalization-enhanced in-band noise increases with symbol rate, which degrades the BER further at the same OSNR. However, the highest attained OSNR is limited by the modulation loss, which increases with the symbol rate because of the stronger pre-emphasis. Thus, we expect a higher OSNR implementation penalty and lower achievable OSNR with increasing the symbol rate. The processed constellations of 110 Gbaud 16QAM and 90 Gbaud 32QAM after 80 km of SSMF are shown in Figure 5.5(c-d). For 80 km transmission, the optimum launch optical power (LOP) into the fiber is 3 to 4 dBm as illustrated in Figure 5.5(e), which is limited by the fiber nonlinearities.

Table 5.1. Summary of Net Bitrate Achieved After 80 km Transmission on a Single Polarization

		Short (3 mm) IQM		Long (4 mm) IQM	
BER threshold	FEC OH	Modulation format	Net bitrate (Gbps)	Modulation format	Net bitrate (Gbps)
3.8×10^{-3}	6.7%	85 Gbaud 16QAM	318	80 Gbaud 32QAM	375
1.25×10^{-2}	14.8%	100 Gbaud 16QAM	348	95 Gbaud 32QAM	413
2.4×10^{-2}	20%	90 Gbaud 32QAM	375	104 Gbaud 32QAM	433
5×10^{-2}	25%	104 Gbaud 32QAM	416	100 Gbaud 64QAM	480

5.2.3.2 Long IQM (Single Polarization)

Likewise, the long (4 mm) modulator transmission results are presented in this section. The optimum reverse bias for minimum BER is 1V and corresponds to a 3-dB EO bandwidth of 25 GHz. Figure 5.6(a) shows the measured BER at different line rates for different formats after 80 km with the summary presented in Table 5.1. Below the 6.7% HD-FEC BER threshold, QAM16 stands as the optimum modulation format. Yet, we transmit 80 Gbaud 32QAM below the 6.7% HD-FEC BER threshold, corresponding to a line rate of 400 Gbps.

The OSNR performance is given in Figure 5.6(b), the maximum realized OSNR at 100 Gbaud 32QAM is 30.3 dB. At the 2.4×10^{-2} SD-FEC threshold, 100 Gbaud 16QAM exhibits an 8.5 dB OSNR implementation penalty compared to 10.5 dB at 110 Gbaud 16QAM. The inset of Figure 5.6(a) shows the BER sensitivity of 116 Gbaud 16QAM and 100 Gbaud 32QAM after 80 km transmission to the number of employed equalizer taps. It is observed that 51 taps are sufficient for a BER below the 20% SD-FEC threshold; increasing the number of taps further

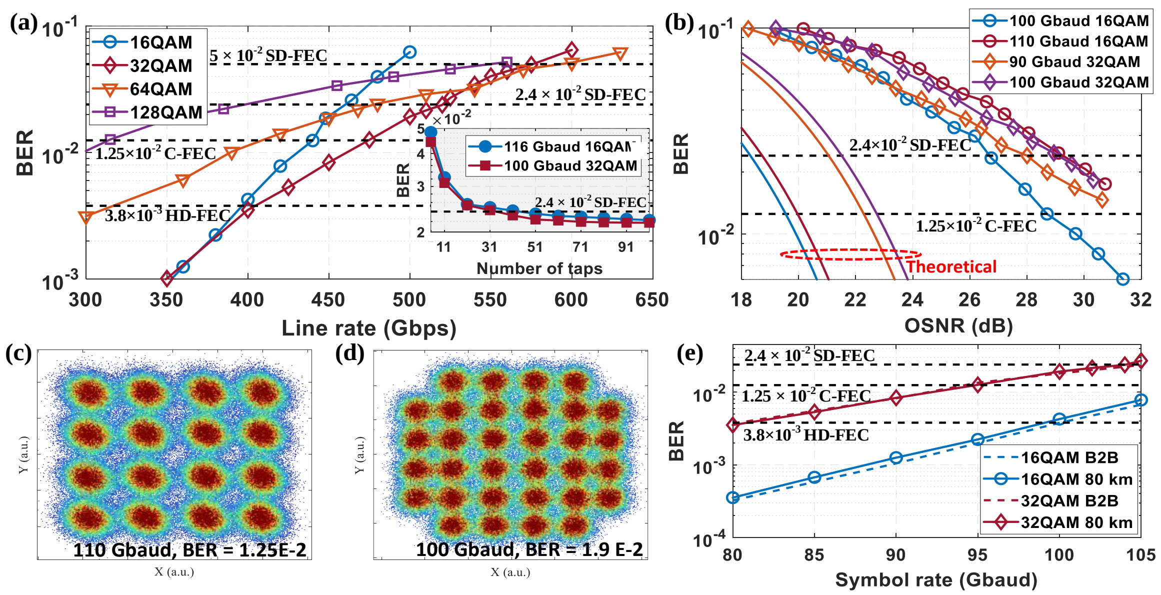

Figure 5.6. (a) The achieved BER versus the line rate for different QAM orders after 80 km transmission using the long IQM. The inset shows BER sensitivity to the number of MIMO filter taps. (b) The OSNR performance at 0.1 nm resolution. The recovered constellations for (c) 110 Gbaud 16QAM and (d) 100 Gbaud 32QAM. (e) The BER versus symbol rate at B2B and after 80 km.

improves the BER negligibly.

Figure 5.6(c-d) show the processed constellation of 110 Gbaud 16QAM and 100 Gbaud 32QAM, respectively. For 32QAM, the outer constellation clusters experience more errors, which implies that nonlinear pre-distortion of the transmitted symbols can improve the results considerably. The BER versus symbol rate at B2B and after 80 km for 16QAM and 32 QAM are depicted in Figure 5.6(e). The degradation of the BER due to the fiber transmission is negligible. Since the modulator is driven by only a fraction of the $2V_\pi$ swing, the optical extinction ratio is limited; leading to high modulation loss. Thus, the optical power just after the SiP chip is around -20 dBm due to the coupling and modulation loss. Therefore, the first EDFA is the dominant source of the noise in the system, and the noise added by the second EDFA leads to minor degradation in the BER performance.

Although the long IQM has lower bandwidth and induces a higher OSNR penalty compared to the short IQM, the long IQM yields better transmission performance. The higher OSNR penalty with the long IQM results from the higher equalization-enhanced noise because of its lower EO bandwidth. The employed RF amplifier has a slow roll-off frequency response up to 45 GHz and a saturation power of 20 dBm corresponding to 6 V_{pp} which is small compared to the IQMs V_π. Consequently, we experienced more limitations from the RF signal swing compared to the bandwidth limitations. This justifies the low reverse biases applied to both IQMs as the RF V_π increases with reverse bias voltage.

Figure 5.7 shows the measured OSNR as a function of symbol rate for 32QAM at B2B and after 80 km. The realized OSNR is approximately 2 dB higher for the long IQM; which results in better BER performance. We observe a ~1 dB degradation in the OSNR after the 80 km transmission, which comes from the second EDFA noise. The higher OSNR in case of the long IQM is due to the higher modulation depth and lower modulation loss.

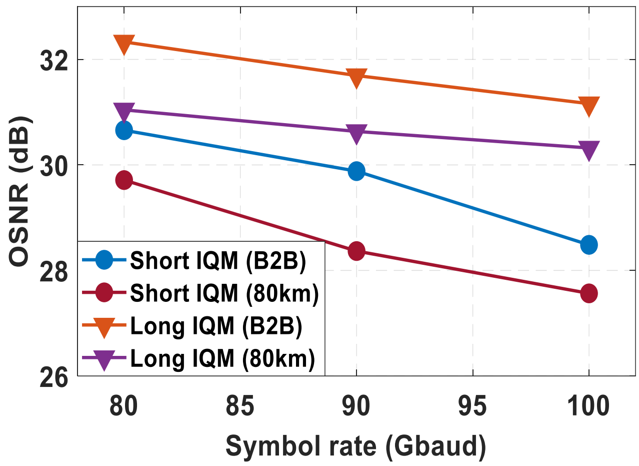

Figure 5.7. The maximum achieved OSNR at 0.1 nm (12.5 GHz) for 32QAM signals at different symbol rates.

5.2.3.3 Long IQM (Dual Polarization)

Further, we employ DP emulation and nonlinear pre-distortion (NLPD) of the transmitted symbols to improve the achieved performance using the long IQM. We retain the DSP routine presented in Figure 5.4; however, we employ a 1D nonlinear lookup table for each quadrature with a 3-symbol memory length to pre-distort the generated symbols at the transmitter. The DP emulator used is composed of a polarization controller followed by a polarization beam splitter to divide the power equally on both orthogonal polarizations. A variable optical delay line is used to decorrelate both polarizations by inducing a delay of 9.2 ns for one polarization. Then, the decorrelated orthogonal signals are combined by a polarization beam combiner (PBC) before transmission. The observed optimum launch optical power is 8 dBm, which is more than twice the value measured in the single polarization experiments as the transmitter-induced nonlinearities are tackled by the NLPD. Aside from these 2 additions, the same experimental setup and DSP blocks are used.

Figure 5.8(a) shows the 80 km transmission results, where the reported BER is the average BER of both polarizations. We demonstrate the transmission of 105 Gbaud DP-64QAM below the 25% SD-FEC threshold, corresponding to a line rate of 1.26 Tbps and a net rate of 1 Tbps.

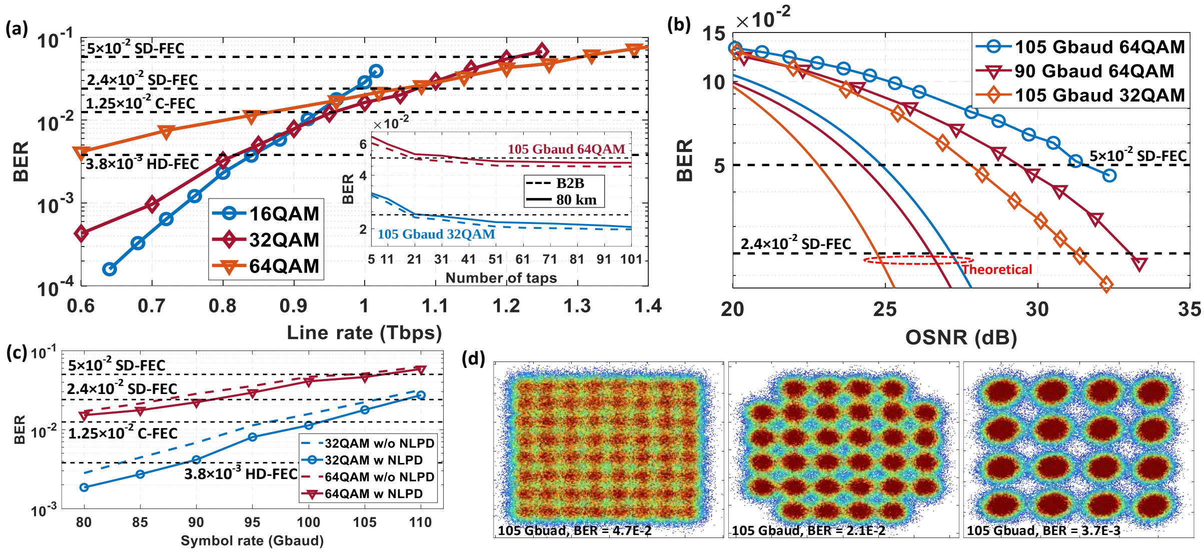

Figure 5.8. (a) BER versus the line-rate for different QAM orders after 80 km, the inset shows the BER performances versus number of MIMO taps. (b) OSNR performance at 0.1 nm at B2B. (c) BER versus symbol rate with and without NLPD. (d) Received constellation of the X polarization for of 105 Gbaud 64QAM, 32QAM, and 16QAM after 80 km transmission.

The achieved performance at the different FEC thresholds is summarized in Table 5.2.

Figure 5.8(b) depicts the OSNR performance at B2B, a 7 dB OSNR penalty is observed. The lower OSNR penalty compared to the single polarization results is coming from the BER improvement because of NLPD. At the highest measured OSNR, the BER noise floor is not reached, suggesting that better coupling and a higher driving signal swing can further improve the BER performance.

Given the swing limitations, we operated the RF amplifiers beyond their 1 dB compression point, which degrades the linearity of the drive signal. Additionally, SiP IQMs have a nonlinear transfer function that considerably affects the higher QAM orders. Figure 5.8(c) shows the BER versus symbol rate with and without NLPD for 32QAM and 64QAM. NLPD results in considerable BER improvement and reduces the OSNR implementation penalty, effectively improving the transmission performance.

The inset of Figure 5.8(a) shows the BER sensitivity to the MIMO filter length; 51 taps are

Table 5.2. Summary of Net Bitrate Achieved After 80 km Transmission and DP Emulation

BER threshold	FEC OH	Modulation format	Net bitrate (Gbps)
3.8×10^{-3}	6.7%	105 Gbaud DP-16QAM	787
		80 Gbaud DP-32QAM	750
1.25×10^{-2}	14.8%	95 Gbaud DP-32QAM	827
		115 Gbaud DP-16QAM	800
2.4×10^{-2}	20%	105 Gbaud DP-32QAM	875
		85 Gbaud DP-64QAM	850
5×10^{-2}	25%	**105 Gbaud DP-64QAM**	**1008**
		115 Gbaud DP-32QAM	920

adequate to reach the error floor similar to the single polarization results. Figure 5.8(d) depicts the received constellation of the 105 Gbaud 16QAM, 32QAM, and 64QAM.

The power consumption of the SPP IQM excluding the TO heaters is given by $P = V_{rms}^2/R$, where V_{rms} is calculated by integrating the Tx waveform, and R is the termination resistance [98]. Thus, the energy consumption per bit considering the transmission of 105 Gbaud 64QAM (Line rate of 630 Gbps) on a single polarization is 190 fJ/bit.

In this experiment, we relied on all-electronic equalization, which preserves the experimental architecture to that of conventional coherent transceivers and networks; however, it requires applying severe pre-emphasis for transmitting high symbol rates. Finally, we infer from our results that the advancements in DACs and ASICs can enable a low bandwidth (25 GHz) SiP IQM to operate beyond 100 Gbaud and meet the 800G requirements, owing to the SiP IQM's slow roll-off frequency response.

5.3 Summary

This work presents the design and compares the transmission performance of two single-segment SiP C-band IQMs with 3 mm and 4 mm phase shifter lengths. The B2B and 80 km single-polarization transmission results along with the OSNR performance of both IQMs are reported. The long IQM outperforms the short one despite its inferior electro-optic bandwidth due to its higher phase-shifting efficiency (lower V_π). The OSNR measurements show that the long IQM exhibits a higher OSNR penalty; however, a higher OSNR is attainable compared to the short IQM, resulting in better BER performance. Using the long IQM, we transmit 95 Gbaud 32QAM over 80 km of SSMF at a BER below the 1.25×10^{-2} C-FEC threshold; corresponding to a net rate of 413 Gbps on a single polarization.

Using nonlinear pre-distortion and dual-polarization emulation, we transmit 95 Gbaud DP-32QAM and 115 Gbaud DP-16QAM over 80 km under the 1.25×10^{-2} C-FEC threshold, which respectively represent net rates of 827 Gbps and 800 Gbps. Moreover, we demonstrate the transmission of 105 Gbaud DP-64QAM over 80 km below the 5×10^{-2} SD-FEC BER threshold using all-electronic equalization in a conventional coherent setup, featuring a net rate of 1 Tbps. Our results support single-segment SiP IQMs as a candidate technology for next-generation 800G coherent networks.

Chapter 6

Equalization-Enhanced Noise Reduction in Bandwidth-Limited Transmission Systems

6.1 Overview

In response to the exponential surge in data traffic, the imperative to improve the capacity of fiber optic communication systems remains constant, for both IMDD and coherent transmission systems. However, increasing the capacity can be achieved by increasing either the symbol rate or the modulation order. Increasing the symbol rate requires higher bandwidth RF and electro-optic componentry. In contrast, employing higher modulation order does not incur any increase in bandwidth, but it requires considerably higher SNR with stringent requirements on the bit resolution of DACs and ADCs. Both approaches are practical; we witnessed the move from OOK to PAM4 and from 23 Gbaud to 112 Gbaud. Yet, the industry always prioritize increasing the symbol rate because of the advancements on the electronics side following Moore's law. 1.6 Tbps coherent modems that operate at 200 Gbaud and fabricated by the 3 nm process are expected to be commercially available in 2024 [51].

High symbol rate transmission challenges the bandwidth of the transmission components and requires equalization DSP to compensate for the intersymbol interference (ISI). However, the powerful equalization amplifies the high-frequency noise within the signal bandwidth and reduces the SNR, which has been reported by several studies and is referred to as equalizer-enhanced in-band noise [64, 67]. This colored correlated noise is handled by adding a post-filter after the equalizer that whitens the noise spectral density at the expense of increasing the ISI. The added ISI is tackled by the maximum likelihood sequence detection (MLSD) algorithm, which adds considerable complexity to the receiver [67, 131].

This Chapter proposes a multiplication-free geometric approach that effectively lessens the impacts of the equalizer-enhanced in-band noise and reduces the BER. The proposed approach distorts the two-dimensional (2D) constellation created from the received signal using a predefined 2D map retrieved from a look-up table (LUT). The effectiveness of the proposed approach is assessed in both IMDD and coherent transmission systems, and is compared to practical equalization schemes.

6.2 Geometric Distortion for Subduing Equalization-Enhanced Noise in Bandwidth-Limited Systems [65]

6.2.1 Equalizer-enhanced in-band noise

Bandwidth-limited transmission systems require strong equalization at the receiver to reduce the ISI and compensate for the degradation of the received signal bandwidth; however, this converts the additive white Gaussian noise (AWGN) into colored noise. Assuming a transmitted signal $s(t)$ through a bandwidth-limited system with channel response $h(t)$, the received signal $q(t)$ can be described by:

$$q(t) = s(t) * h(t) + n(t) \tag{6.1}$$

where $n(t)$ is AWGN, $(*)$ denotes the convolution operation, and $h(t)$ acts as a low-pass filter due to the bandwidth-limited components. Thus, equalizing the signal is essential to recover the high-frequency components of the transmitted signal and remove the ISI. The output of an equalizer with transfer function $e(t)$ can be expressed as:

$$q_e(t) = q(t) * e(t) = s(t) * h(t) * e(t) + n(t) * e(t) \tag{6.2}$$

Given that $e(t)$ is ideally the inverse of $h(t)$ assuming zero ISI as in zero-forcing equalization, $q_e(t)$ can be rewritten as:

$$q_e(t) = s(t) + n(t) * e(t) \tag{6.3}$$

Therefore, the received signal after ideal equalization is the transmitted signal in addition to colored noise because of the high-pass filtering effect of $e(t)$, which is commonly referred to as equalizer-enhanced in-band noise. The colored noise induces a non-Gaussian distribution of the noise at the receiver.

In order to visualize the correlation of noise under bandwidth limitations, we simulate the transmission of 112 Gbaud PAM4 signal with different channel responses, as depicted in Figure 6.1(a). The noise is added after filtering with the simulated channel responses at a fixed

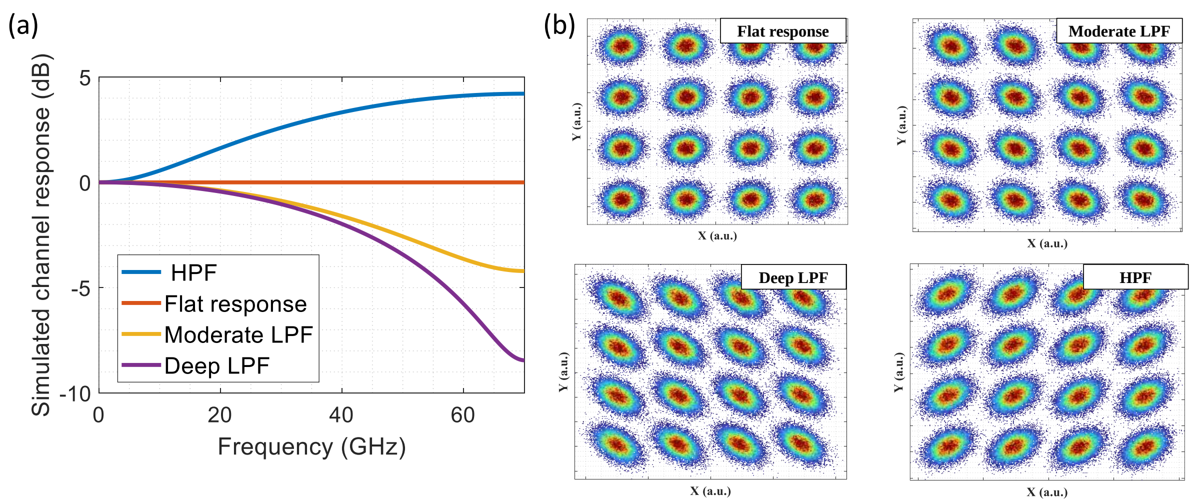

Figure 6.1. (a) The simulated channel response for 112 Gbaud PAM4 signal transmission. (b)The corresponding 2D constellation for each channel response created by time-interleaving the PAM4 symbols.

SNR. At the receiver, we use FFE for equalization and ISI removal. The correlation between noise samples is best observed in a higher-dimensional space. Hence, we time-interleave the equalized PAM4 symbols, treating the PAM4 signal as if it is a 16QAM signal. Subsequently, we plot the resulting 2D constellation diagram, which is illustrated in Figure 6.1(b). This representation provides insights into the noise correlation characteristics in the transmission system.

At the same SNR, we observe that the channel response is imprinted on the noise samples as a correlation. In the 2D noise distribution, we find that it deviates from a circular shape and instead takes on an elliptical form when the channel response is non-flat. The degree of ellipticity, or the correlation coefficient, is directly related to the magnitude of the channel's frequency response. A deeper frequency response corresponds to a higher level of correlation between the noise samples, further shaping the elliptical distribution in the 2D constellation.

Therefore, assuming that the conventional hard decision boundaries are employed, the noise correlation or ellipticity will result in higher BER at the same SNR compared to a flat channel. This is the impact of equalization-enhanced in-band noise. By examining Figure 6.2, we notice that this ellipticity can be corrected geometrically to improve the BER. At the center of the constellation point, the noise samples are minimal and fall within the correct boundaries; hence,

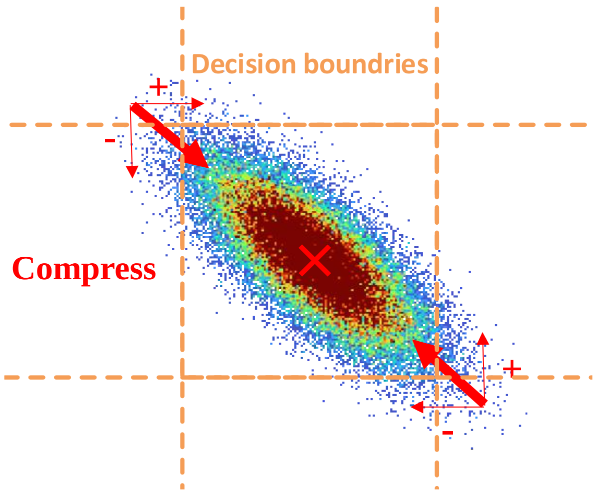

Figure 6.2. Illustration of the colored correlated noise with the conventional HD threshold boundaries.

they do not require modification. At each edge, we notice that the real (X) and imaginary (Y) parts require offsetting with opposite signs to converge to the right transmitted symbol. Furthermore, the two edges need to be compressed in different directions or effectively offsetting the X and Y components with opposite signs. By applying these geometric corrections, we can effectively reduce the impact of noise correlation and improve the BER performance of the system.

In this context, we propose a 2D constellation distortion method that reshapes the constellation to minimize the impact of the colored noise, resulting in considerable reduction in the BER. The proposed method uses a 2D function to correct the time-interleaved 2D constellation without rotating or changing the decision thresholds. We utilized a pre-defined 2D function $F(x, y)$ that can be described as follows:

$$F(x,y) = \sum_{i=1}^{M} Ae^{-\frac{\left((x-\mu_{x_i}-\sigma_x^2)sin\Theta_i\ -\left(y-\mu_{y_i}+\sigma_y^2\right)cos\Theta_i\right)^2}{2\ \sigma_y^2}} e^{-\frac{\left(\left(y-\mu_{y_i}+\sigma_y^2\right)sin\Theta_i + (x-\mu_{x_i}-\sigma_x^2)cos\Theta_i\right)^2}{2\ \sigma_x^2}} - Ae^{-\frac{\left((x-\mu_{x_i}+\sigma_x^2)sin\Theta_i\ -\left(y-\mu_{y_i}-\sigma_y^2\right)cos\Theta_i\right)^2}{2\ \sigma_y^2}} e^{-\frac{\left(\left(y-\mu_{y_i}-\sigma_y^2\right)sin\Theta_i + (x-\mu_{x_i}+\sigma_x^2)cos\Theta_i\right)^2}{2\ \sigma_x^2}} \quad (6.4)$$

where *M* is the number of constellation points in 2D (i.e., 16 for PAM4). *A* denotes the amplitude of each of the 2D Gaussian distributions, μ_{x_i} and μ_{y_i} are the real and imaginary parts of the i^{th} constellation point, respectively. σ_x^2 and σ_y^2 are the variances of the Gaussian distributions along the real and imaginary axes, respectively. Θ_i is the inclination angle of the i^{th} cluster of the received signal with respect to the real axis of the IQ plane, and is approximated by $\Theta_i \approx \tan^{-1}(\sigma_{y_i}^2/\sigma_{x_i}^2)$. For simplicity, we set the amplitude of all the Gaussian distributions to *A*, which is optimized empirically for minimum BER.

$F(x,y)$ is a sum of rotated Gaussians with asymmetric variances, which matches the nature of the received 2D constellation. Each constellation point is enveloped by two 2D Gaussian distributions with opposite amplitude signs and displaced in different directions as illustrated in Figure 6.3. For a received symbol after time-interleaving $R[n] = x_n + y_n j$ such that $x_n = x[2n-1]$ and $y_n = x[2n]$, the output after the 2D constellation distortion is given by:

$$R'[n] = R[n] \mp F(x_n, y_n) \pm F(x_n, y_n) \cdot j \tag{6.5}$$

The $\pm$ sign depends on the direction of inclination or the nature of the channel response. $F(x,y)$ can be created blindly with $\Theta = 45^0$, $\sigma_x^2 = \sigma_y^2 = 0.5$. However, better results are obtained through using a short sequence of the received signal for extracting the signal statistics in terms of the inclination of each cluster Θ_i, and the mean and variance along the real (μ_{x_i}, σ_{xi}^2) and imaginary (μ_{y_i}, σ_{yi}^2) axes; so that the 2D distortion can efficiently correct any nonlinearity in the signal. This approach is multiplication-free and requires a single addition operation and memory access per received symbol, where the 2D distortion map is predefined in a look-up table.

The proposed approach is illustrated in Figure 6.4. We use a 135 Gbaud PAM4 signal transmitted over 2 km in the O-band with a 47 GHz SiP MZM based on [91]. Figure 6.4(a) shows the received eye diagram of a 135 Gbaud PAM4 signal. It is worth noting that the colored

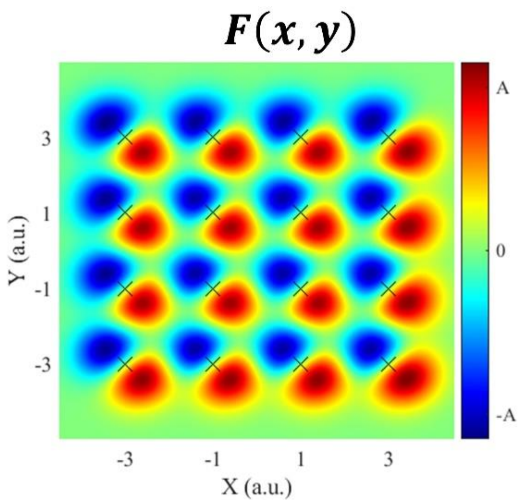

Figure 6.3. The proposed 2D distortion function F(x,y).

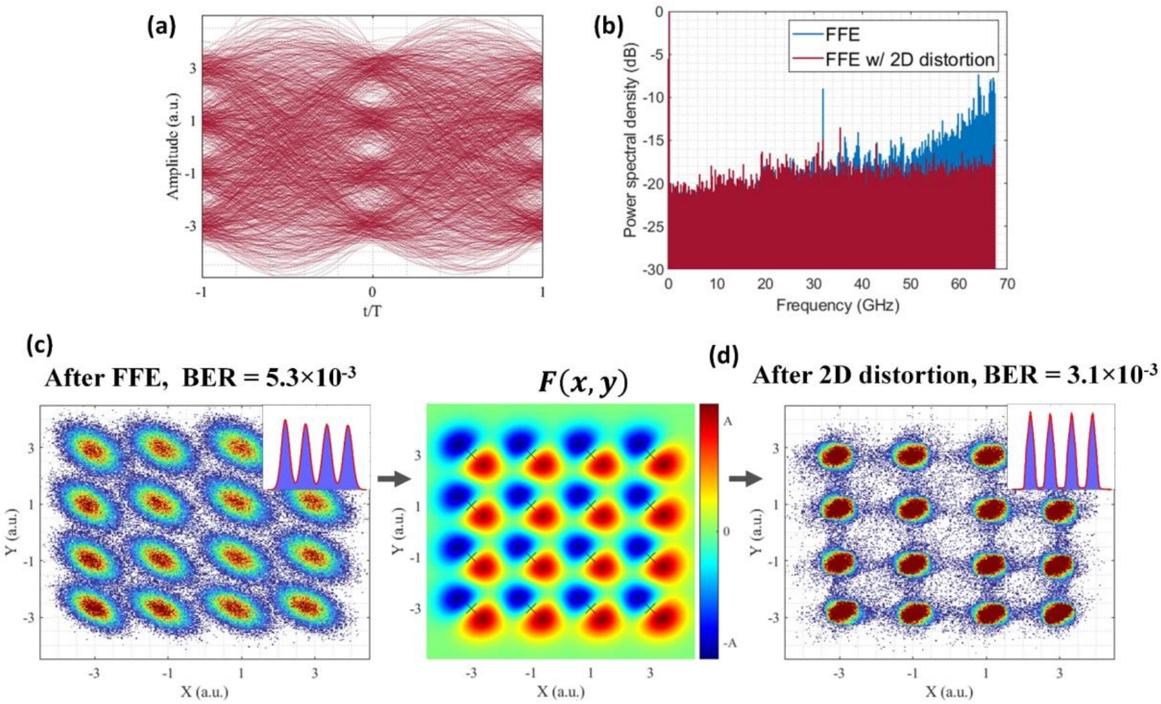

Figure 6.4. (a) The received electrical eye diagram of 135 Gbaud PAM4 signal. (b) The noise power spectral density before and after the 2D constellation distortion. (c) The 2D constellation generated from the same PAM4 signal after FFE, (d) the 2D constellation after distortion, and the inset histograms display the 1D distribution of the signal before thresholding after FFE and after 2D distortion.

noise and the AWGN noise are indistinguishable in 1D representation; hence, this impairment might be overlooked in IMDD systems. Figure 6.4(b) plots the noise power spectral density (PSD) before and after the proposed 2D distortion; the noise PSD is effectively whitened after 2D distortion. Figure 6.4(c) depicts the time-interleaved PAM4 signal represented in 2D after FFE (BER = 5.3×10^{-3}), and the ellipticity of the distributions indicates the existence of colored correlated noise, which blends with Figure 6.4(b). Finally, the distorted constellation (BER = 3.1×10^{-3}) is shown in Figure 6.4(d), which shows how each cluster is distorted to reduce the correlation between the noise samples and whitens the noise PSD, as shown in Figure 6.4(b).

To quantify the gain of employing the proposed for reducing the equalizer-enhanced in-band noise in the absence of other impairments, we simulate a 112 Gbaud PAM4 signal transmitted over different channels at different SNR levels, and we compare the BER

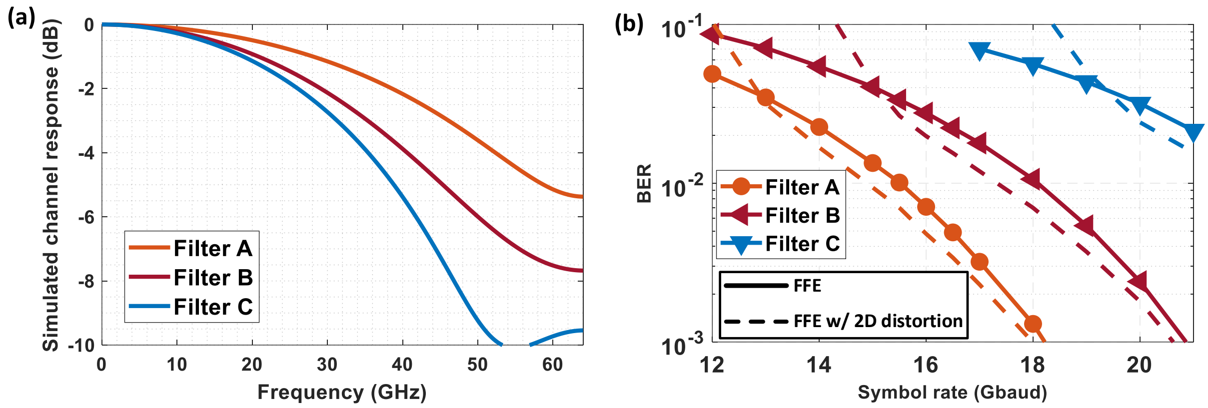

Figure 6.5. (a) The simulated channel response. (b) The BER performance versus SNR for the different channels.

performance if only FFE is used versus if we followed it with the proposed method. Figure 6.5 shows the simulated channel response and corresponding BER versus SNR curves. We observe a gain of more than 0.5 dB for the three cases; however, this occurs for a specific range of BER. If the BER is extremely low, it means that a negligible number of symbols have crossed the thresholding boundaries; hence, the proposed method does not add any gain in that scenario. In contrast, when the BER is very high, it suggests that the two clusters have already blended because of their ellipticity (noise correlation). In that situation, the proposed method blindly distorts the constellations and results in a considerable penalty; however, this is not an issue as this regime occurs for very high BER values that are impractical for FEC correction. Hence, our method is effective when there is correlated noise, but the clusters in 2D are still separable. A 0.5 dB gain in SNR can result in significant power savings considering WDM implementation with multiple channels.

6.2.2 Implementation in IMDD system

In IMDD, the output of the equalizer is a vector of real values. Hence, we time-interleave this real-valued vector to create a complex-valued (2D) vector to apply the $F(x, y)$ distortion. After the 2D distortion, we remap the 2D or complex signal into a real-valued vector for conventional

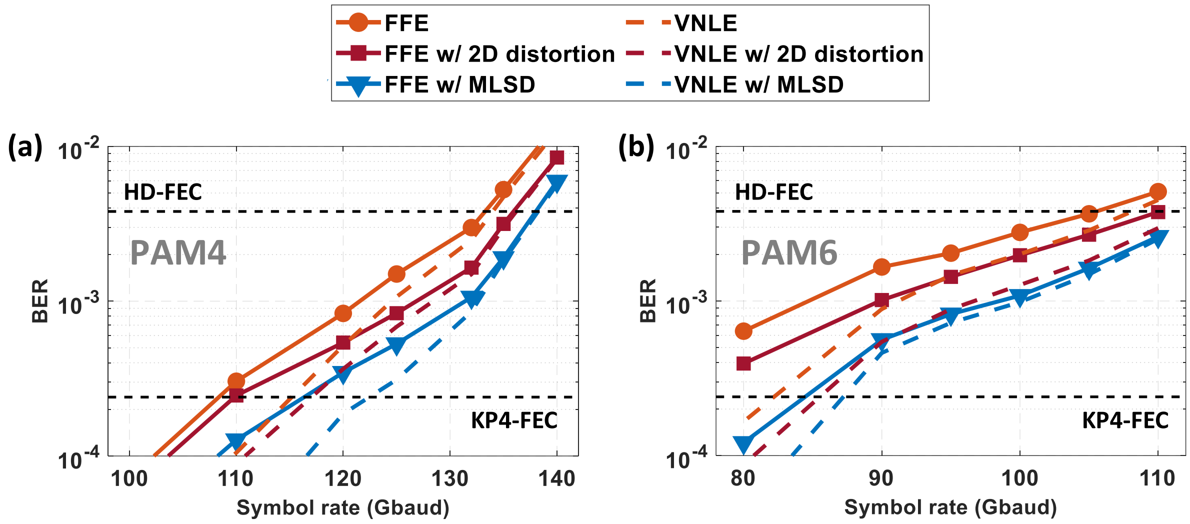

Figure 6.6. The BER versus symbol rate for (a) PAM4 and (b) PAM6 for different receiver DSP routines.

thresholding. This process requires extra two delay taps, one before and one after applying the 2D distortion.

We assess the gain of employing the proposed approach using experimental data of a typical bandwidth-limited IMDD system. The experimental setup is described in more detail in [91]; it employs a 47 GHz SiP O-band MZM while it operates beyond 120 Gbaud (~60 GHz). Figure 6.6(a-b) show the achieved BER at different symbol rates for PAM4 and PAM6, respectively. The performance of linear FFE (solid lines) and VNLE (dashed lines) is compared with and without the proposed 2D constellation distortion and MLSD. The VNLE outperforms the linear FFE due to the nonlinearity induced by the RF amplifier, SiP modulator and the square-law detection. This improvement is more pronounced at lower symbol rates because of the higher signal swing driving the RF amplifier and the SiP modulator. The proposed 2D constellation distortion improves the performance in both cases compared to using the equalizer only case; with more pronounced improvement at higher symbol rates because of the stronger equalization and lower SNR. This indicates the effectiveness of the proposed approach in reducing the equalizer-enhanced colored noise, which results in BER reduction of more than 40% at the HD-FEC thresholds. However, MLSD stands as the best option considering only the BER performance. Computationally, the proposed approach requires a single LUT access every 2 symbols and 2 adders that is incomparably simpler than MLSD, considering its different simplified implementations [132]. Therefore, considering both BER performance and computational complexity, the proposed 2D distortion compromises both metrics and considerably improve the transmission performance.

6.2.3 Implementation in coherent transmission system [133]

In IMDD systems, the received equalized symbols are time-interleaved to generate a 2D constellation that is distorted by the 2D map. The same methodology applies to coherent systems despite starting with complex-valued (2D) equalized symbols. Figure 6.7 shows the evolution of the received symbols throughout the proposed procedure. Initially, the complex-valued equalized symbols are divided into 2 separate real-valued quadratures I and Q. Each quadrature is time-interleaved to generate a 2D constellation that is then distorted with the 2D map. Eventually, the time-interleaving is reversed, yielding two real-valued quadratures. The new quadratures are used to generate the complex-valued symbols before de-mapping and BER calculations. As evidence of the equalization-enhanced colored noise, the 2D constellations generated from the undistorted I and Q quadratures show clustered symbols with asymmetric Gaussian distributions because of the correlated noise as shown in Figure 6.7. For dual-

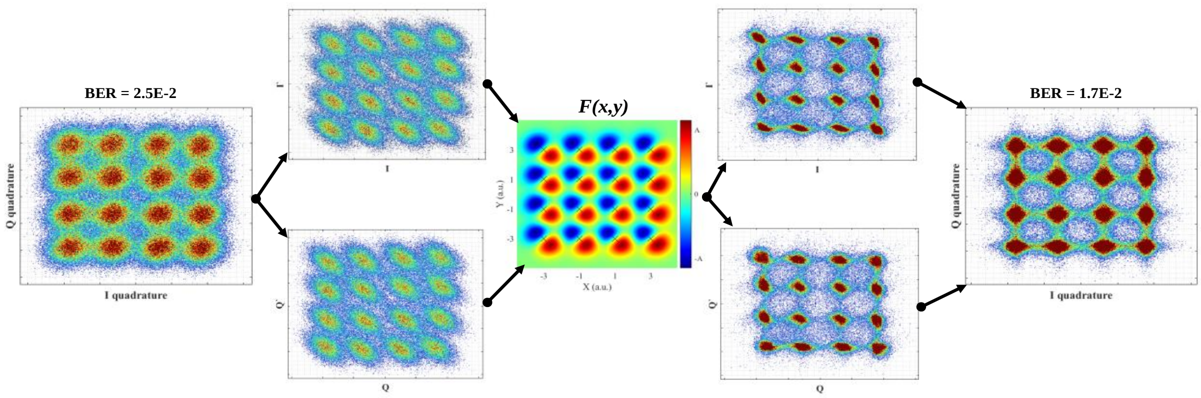

Figure 6.7. Illustration of the 2D constellation distortion approach for a 120 Gbaud 16QAM signal (Only one polarization is shown).

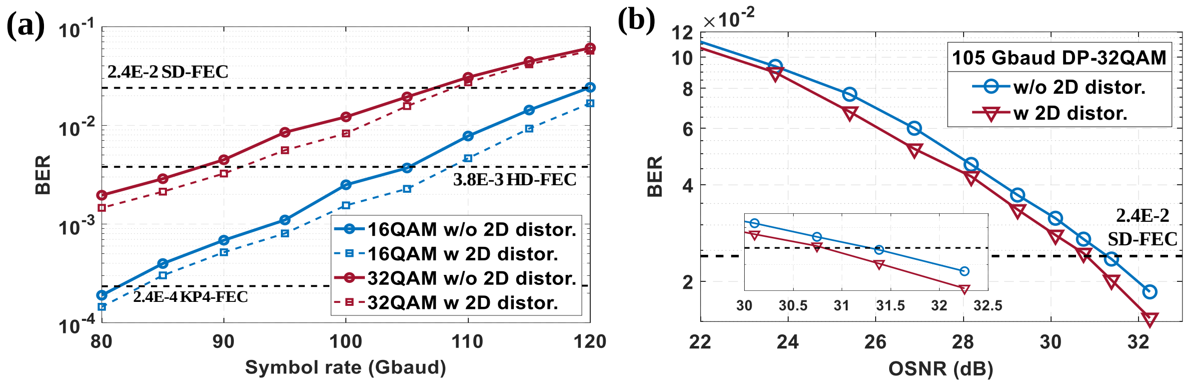

Figure 6.8. (a) BER vs symbol rate for DP-16QAM and DP-32QAM signals with and without constellation distortion. (b) The OSNR performance at 105 Gbaud DP-32QAM in B2B.

polarization systems, the two polarizations with their four quadratures can utilize the same 2D distortion map retrieved from a single LUT, which reduces the complexity given that the procedure does not require any multiplications.

To verify the proposed approach's effectiveness in coherent transmission, we use experimental data from Chapter 5, which uses a 30 GHz SiP IQM for transmitting data beyond 100 Gbaud (~ 50 GHz). Figure 6.8(a) shows the results for DP-16QAM and DP-32QAM in B2B with and without the proposed 2D distortion. These results employ a T/2-spaced real-valued 4×4 multiple-input-multiple-output (MIMO) equalizer. There is an improvement in the BER across the considered symbol rates and FEC thresholds. The OSNR performance at 105 Gbaud DP-32QAM is depicted in Figure 6.8(b), a 0.5 dB OSNR improvement is achieved at the SD-FEC BER threshold. It is worth noting that in the experiment we exhibited a ~7 dB OSNR implementation penalty compared to the theoretical OSNR performance. The observed 0.5 dB gain in OSNR agrees with our simulation results and highlights the potential power consumption reduction accompanied with employing the proposed technique.

6.3 Summary

This work proposes a geometric approach to subdue equalization-enhanced colored (correlated) noise in both IMDD and coherent transmission systems. The proposed scheme uses a predefined 2D map retrieved from a look-up table to distort the 2D constellation generated from the received signal, which lessens the noise variance before thresholding and results in a considerable BER reduction. Computationally, this is a multiplication-free approach; it only requires a single addition and memory access per symbol. In addition, it operates sequentially on the equalized symbols without introducing latency. We verified our proposal with simulations and experimental data from SiP-based IMDD and coherent systems. We observe an SNR gain of more than 0.5 dB in both simulations and with experimental data, which can relax the power requirements in IMDD and coherent systems, highlighting the practical benefits of the proposed approach.

Chapter 7

Discussion and Conclusion

7.1 Discussion

7.1.1 Discussion on IMDD Systems

In Chapter 3, we conducted transmission experiments using a C-band TFLN MZM with various transmitter configurations. This ensures a fair analysis when comparing the following transmitter architectures: (1) the proposed DSP-free transmitter utilizing a single DAC operating at 1 sps without RF amplification [85]; (2) employing an external interleaver to multiplex two DAC outputs without an RF driver [82]; (3) utilizing the external interleaver and amplifying the output RF signal with an external driver [84]; and (4) utilizing the next-generation (prototype) DAC with an integrated interleaver and RF driver, achieving superior bandwidth [31]. Table 7.1 presents a summarized comparison of the transmission performance for the different configurations. It is important to acknowledge that there may be slight variations in the experimental setups used for these experiments; however, these differences do not invalidate the insights gained from this comparison.

Table 7.1. Comparative Summary of our TFLN IMDD Works with the Different Transmitter Configurations.

Transmitter Config.	**DSP-free driver-less transmitter[85]**		**Driver-less transmitter[82]**		**Employing external RF driver[84]**		**Next-gen DAC with internal driver[31]**	
DAC	Keysight M8199A (128 GSa/s)		Keysight M8199A (256 GSa/s)		Keysight M8199A (256 GSa/s)		Keysight M8199B (256 GSa/s)	
Interleaver	No		Yes (external)		Yes (external)		Yes (integrated)	
Description	1 sps DAC (DSP-free) without RF driver		No RF driver		Using SHF 804 RF driver		Keysight integrated RF driver	
Tx RF 10-dB BW	64 GHz (Nyquist criterion)		74 GHz		70 GHz		84 GHz	
RF Swing at 10-dB	800 mV_{pp}		500 mV_{pp}		1.2 V_{pp}		1.2 V_{pp}	
FEC (overhead)	Format	Net (Gbps)	Format	Net (Gbps)	Format	Net (Gbps)	Format	Net (Gbps)
HD-FEC (6.7%)	128 Gbaud PAM8	360	132 Gbaud PAM6	310	132 Gbaud PAM6	310	172 Gbaud PAM6	402
SD-FEC (20%)	128 Gbaud PS-PAM16	400*	136 Gbaud PAM8	342	140 Gbaud PAM8	352	180 Gbaud PAM8	450
Tx DSP	*Probabilistic shaping		Pre-emphasis Pulse shaping		Pre-emphasis Pulse shaping NL compensation		Pre-emphasis Pulse shaping NL compensation	
Rx DSP	NL equalizer (3^{rd} order PNLE)		Linear equalizer (FFE)		NL equalizer (2^{nd} order PNLE)		NL equalizer (2^{nd} order PNLE)	

This comparison strongly supports the deployment of the next-generation 256 GSa/s DAC transmitter configuration, as it achieves the highest data rate considering the different FEC thresholds. The key advantage of this transmitter configuration is its ability to trade off RF signal SNR and bandwidth, enabling the transmission of PAM8 signals at an impressive rate of 180 Gbaud (90 GHz). It is important to note that the first configuration, while capable of transmitting PAM16 signals due to its superior SNR performance in the absence of an interleaver, driver, and digital pre-emphasis, was ultimately limited by the Nyquist criterion, resulting in a maximum symbol rate of 128 Gbaud. This highlights the fact that the first configuration offers very coarse granularity in terms of transmission rate, as further increasing the transmission rate would require the adoption of impractical and irrelevant modulation formats such as PAM24 or PAM32. On the other hand, the next-generation DAC transmitter has the potential to achieve higher performance by improving the bandwidth of the modulator and photodetector to accommodate higher symbol rates. In fact, the industry is already migrating towards 200 Gbaud operation, which demonstrates the ongoing progress in this direction [51].

Furthermore, this comparison strongly indicates that the transmission performance achieved using the first three configurations was primarily limited by the bandwidth and SNR of the RF transmitter, rather than the bandwidth of the TFLN modulator. This is evident from the significant performance improvement observed when combining the same TFLN MZM with the next-generation DAC and its internal driver. The results highlight the advantages of integration, as the co-integration of the DAC, interleaver, and RF driver on the same board significantly enhances the bandwidth without degrading the SNR of the RF transmitter. This, in turn, enables higher data rates and overall improved performance of the transmission system.

Comparing the first two configurations, the utilization of an external interleaver leads to a significant reduction of more than 30% in the output driving swing, accompanied by an alleged increase in bandwidth by approximately 15%. However, it is important to note that the presence of the external interleaver actually degrades the frequency response of the RF transmitter due to the inherent response of the interleaver module itself. While the external interleaver enables operation beyond 64 GHz based on the Nyquist criterion, this is primarily achieved by leveraging the higher sampling rate. Hence, the use of an external interleaver introduces limitations on the overall frequency response of the RF transmitter.

Considering the two middle configurations that both employ an external interleaver, the only difference lies in the utilization of an RF driver. However, due to the low V_π of the TFLN MZM, the benefits of employing an RF driver are rather limited. Moreover, the introduction of an RF driver comes with certain drawbacks, namely a reduction in bandwidth and transmitter SNR. In addition, it dictates adding nonlinear compensation in the transmitter's DSP stack and the utilization of a nonlinear equalizer at the receiver. These nonlinearities are primarily caused by the transfer function of the MZM and the nonlinear input-output relationship of the RF driver. Consequently, the marginal increase in transmission rate, which is less than 3%, comes at the expense of employing nonlinear DSP processing both at the transmitter and receiver. This trade-off undermines the intended benefits of the RF driver, making it less favorable in practice for TFLN-based IMDD systems.

In summary, the assessment of an RF transmitter configuration relies on four main parameters: bandwidth, SNR, linearity, and output driving swing. These parameters must be considered together, acknowledging the inherent trade-offs that exist between them. It is essential to strike a balance among these specifications, as an extremely high bandwidth system with poor SNR or exceptional SNR with limited bandwidth proves impractical for fiber-optic transmission systems. Furthermore, the optimal configuration is contingent upon the modulator platform employed. For example, TFLN modulators can be driven with sub 1 V_{pp} without significant penalties. In contrast, SiP modulators require a higher driving swing, and operating them below 1 V_{pp} incurs a detrimental performance penalty. Hence, optimizing transceiver transmission performance relies on the entire system architecture rather than solely focusing on the performance or specifications of individual components.

Considering the SiP VSB transmitter presented in Chapter 3, we showed the operating principle and the structure of the DD-MZM with the optical delay line. As discussed, the merits of realizing the delay line (temporal skew) in the optical domain are the compact cost-free implementation without incurring any bandwidth limitations other than the FSR. We showed the successful transmission of 56 Gbaud PAM4 over 60 km under the HD-FEC threshold with second-order Volterra nonlinear equalization.

In practical implementations, these channels are often transmitted using wavelength-division multiplexing to optimize cost and effectively utilize the bandwidth of the fiber. However, this requires using optical Mux/Demux filters to combine and separate the different channels. These filters typically have a Gaussian response with ~150 GHz of bandwidth, which results in a super Gaussian response when performing the entire Mux/Demux operation. This "free" super Gaussian response can be leveraged to enhance the VSB generation by effectively filtering out any residual image band, improving the overall transmission quality and reducing the signal-signal beat interference [102]. This can extend the transmission reach to over 100

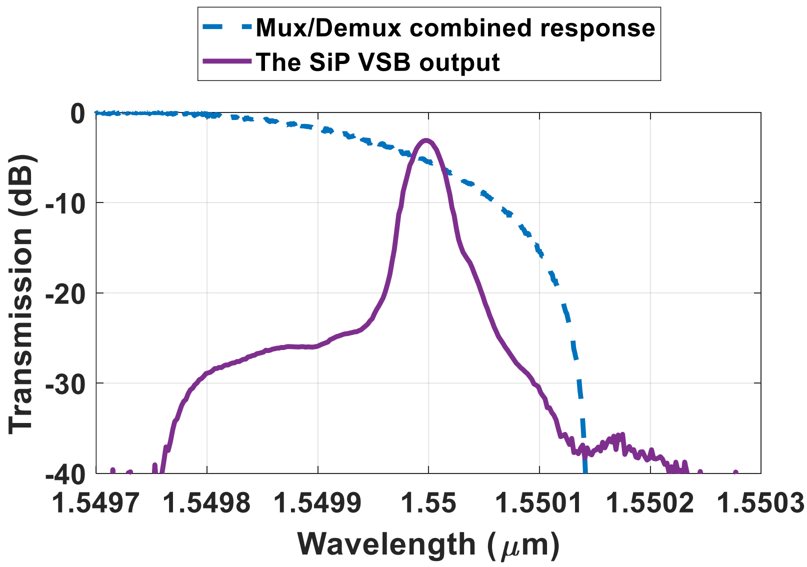

Figure 7.1. Illustration of how the WDM filtering will improve the VSB generation.

km; however, it requires precise control of the wavelength of the laser carrier to avoid attenuating the optical carrier or the other band, as shown in Figure 7.1.

The design of our SiP VSB transmitter can be significantly enhanced with the development of a low-loss SiP tunable delay line. In our current design methodology, the length of the delay line is optimized for a specific symbol rate, taking into account the bandwidth limitations of the SiP MZM. However, this coupling between the three variables and having the delay fixed after device fabrication may potentially limit the performance and flexibility of the VSB transmitter. Therefore, the development of a low-loss tunable delay line in the SiP platform would enable a more versatile operation that supports the different symbol rates while maintaining optimal conditions, allowing for improved transmission performance in terms of BER and reach.

7.1.2 Discussion on Coherent Systems

We believe that coherent invasion into the datacenter is inevitable and will happen sooner than expected. The open questions are which modulator technology and in which operational band. For coherent transmission systems to be competitive with IMDD, they need to offer higher capacities with a competitive power consumption envelope. IMDD solutions for 800 Gbps Ethernet are already commercialized; hence, we envision coherent solutions to start swallowing the market of 1.6 Tbps Ethernet and beyond. In this thesis, we outlined the challenges of operating 4λ×400 Gbps because of the interplay between chromatic dispersion and fiber nonlinearities in the O-band. Thus, the practical IMDD candidate architecture for 1.6 Tbps operation is the 8λ×200 Gbps architecture; however, integrating eight lasers within the same small form factor module is challenging and might become cost-ineffective. In contrast, the 1λ×1.6 Tbps coherent solution will hit the market shortly; yet targeting longer transmission reach [51].

In terms of modulator technologies, SiP and InP served the optical transceivers market impressively during the last decade; however, it seems that we are approaching the limit of what can be achieved with SiP devices employing standard processes. The SiP bandwidth limitation is an issue; however, the bottleneck is the high driving voltage requirement represented by the modulator V_π. Improving both the gain and bandwidth of the RF driver is challenging; the existing RF drivers operating beyond 60 GHz have a maximum output of 2.5 V_{pp}, which is insufficient for driving a conventional SiP IQM. One potential solution is to utilize segmented SiP IQMs with differential drivers, but this approach increases the number of RF components in the system, which is costly and goes against the goal of leveraging the cost-effective SiP platform.

While it is true that major market players can customize the fabrication process to improve the SiP platform's bandwidth and phase-shifting efficiency, these customized processes often involve the deposition of high dielectric constant materials that may be considered contaminants for CMOS processing [134]. However, we believe this is not a significant concern as the monolithic integration aim is not feasible yet. One of the SiP advantages is that it enables the monolithic integration of the DSP ASICs with the photonic devices on the same chip; however, this is not practically precise. It is important to note that at high data rates, such as 800 Gbps and 1.6 Tbps, the DSP is typically fabricated using the most advanced CMOS node, currently 3 nm, which does not support the fabrication or integration of photonic devices. As a result, the ASIC engines are fabricated independently from the optical engine and are co-packaged together during the assembly process.

While SiP has its advantages, InP and TFLN technologies offer better bandwidth and phase-shifting efficiency. InP, in particular, has been proven effective in meeting the demand for higher bandwidth at modest driving voltages, as evidenced by Ciena's 200 Gbaud coherent solutions [51]. On the other hand, TFLN boasts superior overall specifications. However, there are concerns regarding the immaturity of TFLN technology, its costly fabrication, and the weak supply chain, which are common challenges for emerging technologies. It is expected that these concerns will be addressed over time, and TFLN-based products may capture a significant portion of the market for extremely high-speed applications, such as 1.6 Tbps single-carrier coherent transmission.

Employing TFLN offers significant advantages in terms of power consumption, as highlighted in the analysis presented in Chapter 4. While the current fabrication costs of TFLN may be higher compared to other technologies, the long-term benefits in terms of reduced power consumption outweigh this initial investment. By shifting towards TFLN-based solutions, datacenters can experience improved performance while simultaneously lowering their running costs. The reduced power consumption of TFLN-based devices directly translates into lower operational expenses, contributing to more sustainable and environmentally friendly datacenter operations. Moreover, the potential long-term cost savings resulting from decreased power consumption make the higher initial fixed costs associated with TFLN fabrication more viable and justifiable.

The choice of operational band for short-reach coherent transmission systems involves considering the advantages and disadvantages of each band. Operating in the O-band offers the advantage of avoiding chromatic dispersion, which in turn reduces electronic equalization enhanced phase noise (EEPN), relaxes the phase noise requirements for the carrier and LO lasers, and reduces DSP power consumption. On the other hand, optical transceiver companies already have mature C-band coherent technologies that can be easily customized for shorter-reach markets.

Table 7.2. Comparison between C-band and O-band for Coherent Transmission

Point of comparison	C-band	O-band
Fiber loss	0.2 dB/cm	0.36 dB/km
Chromatic dispersion	Requires digital compensation (beyond 2 km)	Negligible
EEPN	High	Low
Components maturity	Mature	Under-development (hybrids, BPDs)
WDM compatibility	Compatible	Challenging because of FWM

Indeed, market dynamics and considerations play a significant role in determining the choice between the C-band and O-band for short-reach transmission in datacenter environments. While the O-band holds promise in terms of technology performance, the availability and flexibility of C-band solutions can be advantageous for datacenter operators. With C-band solutions, operators can acquire 1.6 Tbps pluggable modules that can cater to both intra- and inter-datacenter interconnects, as well as long-haul transmission. This offers operators a higher level of flexibility in designing their datacenters. However, the increased demand for C-band coherent pluggables can strain the supply chain, potentially leading to higher prices. Ultimately, market dynamics and cost considerations will play a crucial role in determining the preferred band for short-reach coherent transmission in datacenter environments.

One of the concerns of datacenter operators regarding the use of coherent modems for short-reach links is the coarse fan-out granularity. They prefer a "pay for what you need" model, which is well-addressed by the IMDD architecture. IMDD systems offer finer fan-out granularity and greater flexibility due to their use of WDM. This means that datacenter operators have the option to selectively use a subset or all of the available WDM channels based on their traffic and specific needs. This flexibility can result in significant savings in terms of running costs. In contrast, coherent solutions typically have fixed granularity, which is at least four times larger than that offered by equivalent IMDD solutions. The fixed granularity of coherent systems means that datacenter operators may have to allocate more resources than necessary for their specific requirements, potentially resulting in underutilization and higher costs. The ability of IMDD systems to provide finer granularity and greater flexibility is a distinct advantage in meeting the specific needs and cost considerations of datacenter operations.

In summary, both IMDD and coherent transmission systems will continue to push for increased capacity and extended transmission reach while considering power consumption. Both architectures will have their place within datacenters, with coherent solutions being more scalable for higher capacities and likely dominating the high-speed market, whether based on InP or TFLN technology. On the other hand, IMDD systems based on SiP will likely dominate the low-cost market, prioritizing cost-effectiveness. Ultimately, the choice of architecture will depend on the specific requirements, cost considerations, and performance objectives of datacenter operators.

7.1.3 Discussion on DSP

As highlighted in Chapter 4, the power consumption of ASIC engines accounts for more than 50% of the overall power consumption of the optical transceiver. Therefore, it is crucial to carefully optimize and tailor DSP functionalities to establish a balance between performance and power consumption.

With the continuous advancements in CMOS technology, the inclusion of more DSP blocks in ASICs is becoming more feasible. We anticipate that the market for DSP ASICs will evolve into four distinct categories: low-cost IMDD, high-performance IMDD, short-reach (coherent-lite) coherent DSP, and long-haul high-performance coherent DSP. While these categories already exist to some extent, we expect further differentiation and specialization in the future.

The low-cost IMDD DSP category will cater to applications utilizing data rates up to 100 Gbps/λ. These DSPs will prioritize minimal power consumption and cost-efficiency, often fabricated using older process nodes to reduce manufacturing costs.

The high-performance IMDD DSP category will target applications at 200 Gbps/λ and potentially even 400 Gbps/λ. These DSPs will incorporate additional DSP blocks, such as simplified versions of maximum likelihood sequence detectors (MLSD) and decision-feedback equalizers (DFE), to achieve higher performance and enable advanced modulation schemes.

The short-reach coherent DSP category will focus on enabling coherent transmission in shorter-reach applications. These DSPs will be streamlined and optimized for power efficiency by eliminating unnecessary functionalities like fiber nonlinearity mitigation, which is less relevant in short-reach scenarios. The aim is to make the power consumption of short-reach coherent solutions more competitive with IMDD alternatives.

The long-haul high-performance coherent DSP category will encompass DSPs that offer comprehensive functionalities and target long-haul transmission applications. These DSPs will prioritize performance and aim to extend the transmission reach as much as possible. They will typically be fabricated using the latest CMOS process nodes to leverage the benefits of advanced technology.

Overall, the differentiation between these four categories of DSP ASICs will become more pronounced as the market continues to evolve. The specific requirements of different applications and transmission scenarios will drive the development of DSP ASICs tailored to each category, enabling more efficient and optimized solutions for datacenter operators.

7.2 Future work

As outlined in Chapter 1, this thesis investigates different aspects coving the wavelength-architecture 2×2 matrix. Each of these configurations comes with its hurdles and challenges that we have tried to address partially through our work in the thesis. In this section, we will introduce several ideas that can serve as future directions for future work, building upon the contributions presented in Chapters 3 to 6.

O-band IMDD transmission:

In Chapter 3, we presented the first O-band IMDD system operating at net 400 Gbps over a distance of 10 km. However, when aiming to achieve 1.6 Tbps solutions using 4λ×400 Gbps, several challenges arise. The primary challenge stems from the power fading caused by chromatic dispersion, particularly at the edges of the O-band, when dealing with high symbol rate transmissions. This renders the use of conventional CWDM with 20 nm spacing impractical and necessitates a restructuring of the WDM grid.

Accordingly, there is a need to optimize the WDM grid for the different candidate architectures to compromise the effects of chromatic dispersion and fiber nonlinearity (FWM) for 400/λ Gbps transmission, including 1) 240 GBaud PAM4; 2) 192 GBaud PAM6; and 3) 160 GBaud PAM8 at 2 and 10km in the O-band over SMF. Because the dispersion penalty scales quadratically with the symbol rate and linearly with fiber length, the optimal WDM grid will vary for the three modulation formats and for different transmission reaches. In addition, polarization diversity can be harnessed to suppress the nonlinearities and improve transmission performance. Several case scenarios can be researched both in simulations and experimentally: XXXX, XYXY, XYYX (such that X is one polarization and Y is the orthogonal polarization) [135]. The outcome of this research should be a robust design methodology and subsequent prescription for a net 1.6 Tbps 4λ WDM grid considering the different modulation formats and transmission reach.

C-band IMDD transmission:

The SiP VSB transmitter demonstrated in Chapter 3 effectively enabled transmitting 56 Gbaud over 60 km of SMF under the HD-FEC threshold. Yet, incorporating a tunable optical delay line instead of the fixed delay line we used can improve the transmission performance and improve the flexibility of the VSB transmitter operation.

Another area of exploration is the integration of the SiP VSB transmitter with RF drivers through a monolithic process, such as Global Foundries 45SPCLO [136]. By co-designing the SiP MZM and its drivers, significant improvements in bandwidth can be achieved. It is worth noting that the design of these drivers commonly incorporates inductive peaking, which further enhances the overall bandwidth. This integration is expected to further support the simplicity and effectiveness of the proposed VSB transmitter configuration, moving the load to the DSP.

O-band coherent transmission:

As discussed in the previous section and Chapter 4, from the technology point of view, O-band coherent solutions are the best candidate to scale the capacities of data transmission within 2 to 10 km reach; however, one limitation is the limited fan-out granularity opposing the "pay for what you need" model supported by IMDD. Hence, we believe that flexible-rate coherent transmission can facilitate the adoption of this technology for intra-DCIs as long as it does not increase power consumption considerably. In addition, this application space is primarily concerned with power consumption; hence, simplifying the DSP requirements will be very beneficial.

C-band coherent transmission:

In Chapter 5, we presented a 30 GHz SiP single-segment MZM capable of supporting net 1 Tbps operation, owing to the higher bandwidth and signal fidelity of the employed RF transmitter. Along that line, it is feasible to improve the electro-optic bandwidth of this IQ modulator beyond 50 GHz without segmenting the electrodes, by either using short segments of inductors along the traveling-wave electrodes or by shrinking the length of the electrodes by employing an L-shaped junction with higher phase-shifting efficiency. Both approaches are proven to be effective in extending the bandwidth of the SiP modulators and can considerably improve transmission performance. Yet, a practical target would be achieving net 1.2 Tbps transmission at a more practical FEC threshold (i.e., O-FEC).

Looking ahead, it is anticipated that SiP technology will face significant challenges in supporting 1.6 Tbps/λ operations. Consequently, transceiver vendors are likely to be receptive to integrating additional DSP functionalities into their DSP ASIC engines to enhance performance. Therefore, the focus of DSP development in this application space will shift towards improving performance rather than solely focusing on power consumption.

References

[1] D. Reinsel, J. Gantz, and J. Rydning, "The Digitization of the World From Edge to Core," [Online], Accessed: May. 20, 2023, Available: https://www.seagate.com/files/www-content/our-story/trends/files/idc-seagate-dataage-whitepaper.pdf.

[2] K. Zhong, X. Zhou, J. Huo, C. Yu, C. Lu, and A. P. T. Lau, "Digital signal processing for short-reach optical communications: A review of current technologies and future trends," *Journal of Lightwave Technology,* vol. 36, no. 2, pp. 377-400, 2018.

[3] P. J. Winzer, D. T. Neilson, and A. R. Chraplyvy, "Fiber-optic transmission and networking: the previous 20 and the next 20 years," *Optics express,* vol. 26, no. 18, pp. 24190-24239, 2018.

[4] H. Rong, H. Zhang, S. Xiao, C. Li, and C. Hu, "Optimizing energy consumption for data centers," *Renewable and Sustainable Energy Reviews,* vol. 58, pp. 674-691, 2016.

[5] S. J. Savory, "Digital coherent optical receivers: Algorithms and subsystems," *IEEE Journal of selected topics in quantum electronics,* vol. 16, no. 5, pp. 1164-1179, 2010.

[6] A. Tatarczak *et al.*, "Reach extension and capacity enhancement of VCSEL-based transmission over single-lane MMF links," *Journal of Lightwave Technology,* vol. 35, no. 4, pp. 565-571, 2016.

[7] E. Agrell *et al.*, "Roadmap of optical communications," *Journal of Optics,* vol. 18, no. 6, p. 063002, 2016.

[8] G. R. Martella, A. Nespola, S. Straullu, F. Forghieri, and R. Gaudino, "Scaling laws for unamplified coherent transmission in next-generation short-reach and access networks," *Journal of Lightwave Technology,* vol. 39, no. 18, pp. 5805-5814, 2021.

[9] J. Zhou and Q. Zhang, "Multiple Tb/s Coherent Optical Transceivers for Short Reach Interconnect," *IEEE Journal of Selected Topics in Quantum Electronics,* 2022.

[10] D. Tauber, "Role of Coherent System in the Next DCI Generation," in *2022 Optical Fiber Communications Conference and Exhibition (OFC),* 2022: IEEE, pp. 1-3.

[11] A. Shahpari *et al.*, "Coherent access: A review," *Journal of Lightwave Technology,* vol. 35, no. 4, pp. 1050-1058, 2016.

[12] E. Berikaa *et al.*, "Net 1.6 Tbps O-band Coherent Transmission over 10 km Using a TFLN IQM and DFB Lasers for Carrier and LO," in *Optical Fiber Communication Conference*, 2023: Optica Publishing Group, p. Th4B. 1.

[13] "Detectors - Fraunhofer Heinrich-Hertz-Institut," [Online] Accessed: May. 20, 2023, Available:https://www.hhi.fraunhofer.de/en/departments/pc/research-groups/detectors.html

[14] K. Liu, C. R. Ye, S. Khan, and V. J. Sorger, "Review and perspective on ultrafast wavelength-size electro-optic modulators," *Laser & Photonics Reviews,* vol. 9, no. 2, pp. 172-194, 2015.

[15] D. Zhu *et al.*, "Integrated photonics on thin-film lithium niobate," *Advances in Optics and Photonics,* vol. 13, no. 2, pp. 242-352, 2021.

[16] C. Wang *et al.*, "Integrated lithium niobate electro-optic modulators operating at CMOS-compatible voltages," *Nature,* vol. 562, no. 7725, pp. 101-104, 2018.

[17] D. J. Lockwood and L. Pavesi, *Silicon Photonics IV*. Springer, 2021.

[18] E. Pincemin and Y. Loussouarn, "Silicon Photonic ZR/ZR+ DCO-CFP2 Interface for DCI and Metro-Regional 400G Optical Communications," in *Optical Fiber Communication Conference*, 2021: Optical Society of America, p. M3F. 2.

[19] A. Rahim *et al.*, "Taking silicon photonics modulators to a higher performance level: state-of-the-art and a review of new technologies," *Advanced Photonics,* vol. 3, no. 2, p. 024003, 2021.

[20] S. Y. Siew *et al.*, "Review of silicon photonics technology and platform development," *Journal of Lightwave Technology,* vol. 39, no. 13, pp. 4374-4389, 2021.

[21] Y. Shi *et al.*, "Silicon photonics for high-capacity data communications," *Photonics Research,* vol. 10, no. 9, pp. A106-A134, 2022.

[22] D. Liang and J. E. Bowers, "Recent progress in heterogeneous III-V-on-silicon photonic integration," *Light: Advanced Manufacturing,* vol. 2, no. 1, pp. 59-83, 2021.

[23] S. Keyvaninia *et al.*, "Demonstration of a heterogeneously integrated III-V/SOI single wavelength tunable laser," *Optics express,* vol. 21, no. 3, pp. 3784-3792, 2013.

[24] A. Shams-Ansari *et al.*, "Electrically pumped laser transmitter integrated on thin-film lithium niobate," *Optica,* vol. 9, no. 4, pp. 408-411, 2022.

[25] K. Zhang, Q. Zhuge, H. Xin, W. Hu, and D. V. Plant, "Performance comparison of DML, EML and MZM in dispersion-unmanaged short reach transmissions with digital signal processing," *Optics express,* vol. 26, no. 26, pp. 34288-34304, 2018.

[26] M. Theurer *et al.*, "200 Gb/s Uncooled EML with Single MQW Layer Stack Design," in *European Conference and Exhibition on Optical Communication*, 2022: Optica Publishing Group, p. Th1E. 5.

[27] X. Pang *et al.*, "200 Gb/s Unamplified IM/DD Transmission over 20-km SMF with an O-band Low-Chirp Directly Modulated Laser," in *2022 European Conference on Optical Communication (ECOC)*, 2022: IEEE, pp. 1-4.

[28] A. Uchiyama, S. Okuda, Y. Hokama, M. Shirao, K. Abe, and T. Yamatoya, "225 Gb/s PAM4 2 km and 10 km Transmission of EMLs with Hybrid Waveguide Structure for 800GbE and 1.6 TbE Transceivers," in *Optical Fiber Communication Conference*, 2023: Optica Publishing Group, p. M2D. 2.

[29] O. Ozolins *et al.*, "Optical Amplification-Free 310/256 Gbaud OOK, 197/145 Gbaud PAM4, and 160/116 Gbaud PAM6 EML/DML-based Data Center Links," in *Optical Fiber Communication Conference*, 2023: Optica Publishing Group, p. Th4B. 2.

[30] M. S. B. Hossain *et al.*, "402 Gb/s PAM-8 IM/DD O-Band EML Transmission," in *2021 European Conference on Optical Communication (ECOC)*, 2021: IEEE, pp. 1-4.

[31] E. Berikaa *et al.*, "TFLN MZMs and Next-Gen DACs: Enabling Beyond 400 Gbps IMDD O-band and C-band Transmission," *IEEE Photonics Technology Letters,* 2023 2023.

[32] D. Che and X. Chen, "Higher-Order Modulation vs Faster-Than-Nyquist PAM-4 for Datacenter IM-DD Optics: An AIR Comparison Under Practical Bandwidth Limits," *Journal of Lightwave Technology,* vol. 40, no. 10, pp. 3347-3357, 2022.

[33] "800G pluggable MSA" [Online], Accessed: May. 20, 2023, Available: https://www.800gmsa.com/.

[34] Q. Zhang, N. Stojanovic, C. Xie, C. Prodaniuc, and P. Laskowski, "Transmission of single lane 128 Gbit/s PAM-4 signals over an 80 km SSMF link, enabled by DDMZM aided dispersion pre-compensation," *Optics express,* vol. 24, no. 21, pp. 24580-24591, 2016.

[35] J. Zhang, J. Yu, J. Shi, and H.-C. Chien, "Digital dispersion pre-compensation and nonlinearity impairments pre-and post-processing for C-band 400G PAM-4 transmission over SSMF based on direct-detection," in *2017 European Conference on Optical Communication (ECOC)*, 2017: IEEE, pp. 1-3.

[36] P. Torres-Ferrera, G. Rizzelli, V. Ferrero, and R. Gaudino, "100+ Gbps/λ 50 km C-band downstream PON using CD digital pre-compensation and direct-detection ONU receiver," *Journal of Lightwave Technology,* vol. 38, no. 24, pp. 6807-6816, 2020.

[37] L. Shu *et al.*, "Single-lane 112-Gbit/s SSB-PAM4 transmission with dual-drive MZM and Kramers–Kronig detection over 80-km SSMF," *IEEE Photonics Journal,* vol. 9, no. 6, pp. 1-9, 2017.

[38] X. Ruan *et al.*, "Experimental comparison of direct detection Nyquist SSB transmission based on silicon dual-drive and IQ Mach-Zehnder modulators with electrical packaging," *Optics Express,* vol. 25, no. 16, pp. 19332-19342, 2017.

[39] X. Li, Z. Xing, M. S. Alam, M. E. Mousa-Pasandi, M. O'Sullivan, and D. V. Plant, "Demonstration of C-band amplifier-free 100 Gb/s/λ direct-detection links beyond 40-km SMF using a high-power SSB transmitter," *Journal of Lightwave Technology,* vol. 38, no. 22, pp. 6170-6177, 2020.

[40] H. Sun *et al.*, "800G DSP ASIC design using probabilistic shaping and digital sub-carrier multiplexing," *Journal of lightwave technology,* vol. 38, no. 17, pp. 4744-4756, 2020.

[41] J. Cheng, C. Xie, Y. Chen, X. Chen, M. Tang, and S. Fu, "Comparison of coherent and IMDD transceivers for intra datacenter optical interconnects," in *2019 Optical Fiber Communications Conference and Exhibition (OFC)*, 2019: IEEE, pp. 1-3.

[42] C. Lam, X. Zhou, and H. Liu, "Coherent-Lite for beyond 400GbE," in *Proc. IEEE 802.3 Beyond 400 Gb/s Ethernet Study Group Meeting*, 2021.

[43] C. Doerr *et al.*, "O, E, S, C, and L band silicon photonics coherent modulator/receiver," in *2016 Optical Fiber Communications Conference and Exhibition (OFC)*, 2016: IEEE, pp. 1-3.

[44] A. Samani *et al.*, "180 Gb/s single carrier single polarization 16-QAM transmission using an O-band silicon photonic IQM," *Optics Express,* vol. 27, no. 10, pp. 14447-14456, 2019.

[45] P. M. Seiler *et al.*, "Multiband silicon photonic ePIC coherent receiver for 64 GBd QPSK," *Journal of Lightwave Technology,* vol. 40, no. 10, pp. 3331-3337, 2022.

[46] A. Maharry *et al.*, "First Demonstration of an O-Band Coherent Link for Intra-Data Center Applications," in *European Conference and Exhibition on Optical Communication*, 2022: Optica Publishing Group, p. Mo4F. 4.

[47] T. Hirokawa *et al.*, "Analog coherent detection for energy efficient intra-data center links at 200 Gbps per wavelength," *Journal of Lightwave Technology,* vol. 39, no. 2, pp. 520-531, 2020.

[48] L. Wilkinson. "OIF Launches 800G Coherent and Co-Packaging Framework IA Projects, Elects New Board Members/Positions, Officers and Working Group Chairs." [Online] Accessed: May. 20, 2023, Available: https://www.oiforum.com/technical-work/hot-topics/800g-coherent/.

[49] J. Wang *et al.*, "Silicon Photonics IQ Modulator Targeted for 800ZR Data Center Interconnection," in *European Conference and Exhibition on Optical Communication*, 2022: Optica Publishing Group, p. We3D. 4.

[50] E. Berikaa, M. S. Alam, A. Samani, S. Lessard, and D. V. Plant, "Net 1 Tbps/λ Transmission Over 80 km of SSMF Using a Single Segment SiP IQM With All-Electronic Equalization," in *Optical Fiber Communication Conference*, 2022: Optical Society of America, p. Th4A. 5.

[51] S. McFeely, "Introducing WaveLogic 6: Another industry first from Ciena," ed.

[52] T. Okoshi, "Recent advances in coherent optical fiber communication systems," *Journal of lightwave technology,* vol. 5, no. 1, pp. 44-52, 1987.

[53] A. Davis, M. Pettitt, J. King, and S. Wright, "Phase diversity techniques for coherent optical receivers," *Journal of lightwave technology,* vol. 5, no. 4, pp. 561-572, 1987.

[54] N. S. Bergano, J. Aspell, C. Davidson, P. Trischitta, B. Nyman, and F. Kerfoot, "A 9000 km 5 Gb/s and 21,000 km 2.4 Gb/s feasibility demonstration of transoceanic EDFA systems using a circulating loop," in *Optical Fiber Communication Conference*, 1991: Optical Society of America, p. PD13.

[55] C. Laperle and M. O'Sullivan, "Advances in high-speed DACs, ADCs, and DSP for optical coherent transceivers," *Journal of lightwave technology,* vol. 32, no. 4, pp. 629-643, 2014.

[56] W. Shieh, C. Sun, and H. Ji, "Carrier-assisted differential detection," *Light: Science & Applications,* vol. 9, no. 1, pp. 1-9, 2020.

[57] X. Li, M. O’Sullivan, Z. Xing, M. S. Alam, M. E. Mousa-Pasandi, and D. V. Plant, "Asymmetric self-coherent detection," *Optics Express,* vol. 29, no. 16, pp. 25412-25427, 2021.

[58] A. Samani *et al.*, "Silicon photonic Mach–Zehnder modulator architectures for on chip PAM-4 signal generation," *Journal of Lightwave Technology,* vol. 37, no. 13, pp. 2989-2999, 2019.

[59] R. Soref and B. Bennett, "Electrooptical effects in silicon," *IEEE journal of quantum electronics,* vol. 23, no. 1, pp. 123-129, 1987.

[60] G. P. Agrawal, "Nonlinear fiber optics," in *Nonlinear Science at the Dawn of the 21st Century*: Springer, 2000, pp. 195-211.

[61] T. Rahman, S. Calabrò, N. Stojanovic, L. Zhang, J. Wei, and C. Xie, "LUT-assisted pre-compensation for 225 Gb/s/λ O-band transmission," 2019.

[62] F. P. Guiomar, J. D. Reis, A. L. Teixeira, and A. N. Pinto, "Mitigation of intra-channel nonlinearities using a frequency-domain Volterra series equalizer," *Optics express,* vol. 20, no. 2, pp. 1360-1369, 2012.

[63] S. Varughese, D. Lippiatt, S. Tibuleac, and S. E. Ralph, "Frequency dependent ENoB requirements for 400G/600G/800G optical links," *Journal of Lightwave Technology,* vol. 38, no. 18, pp. 5008-5016, 2020.

[64] D. Li *et al.*, "Low-complexity equalization scheme for suppressing FFE-enhanced in-band noise and ISI in 100 Gbps PAM4 optical IMDD system," *Optics letters,* vol. 45, no. 9, pp. 2555-2558, 2020.

[65] E. Berikaa, M. S. Alam, M. Jacques, X. Li, P.-C. Koh, and D. V. Plant, "2D Constellation Distortion for Subduing Equalization Noise in Bandwidth-Limited IMDD Systems," *IEEE Photonics Technology Letters,* vol. 34, no. 5, pp. 267-270, 2022.

[66] S. T. Le and J. Cho, "OSNR-Aware Digital Pre-Emphasis for High Baudrate Coherent Optical Transmissions," in *2022 Optical Fiber Communications Conference and Exhibition (OFC),* 2022: IEEE, pp. 1-3.

[67] H. Zhou *et al.*, "Recent advances in equalization technologies for short-reach optical links based on PAM4 modulation: A review," *Applied Sciences*, vol. 9, no. 11, p. 2342, 2019.

[68] D. A. de Arruda Mello and F. A. Barbosa, *Digital Coherent Optical Systems: Architecture and Algorithms*. Springer Nature, 2021.

[69] J. R. Barry and E. A. Lee, "Performance of coherent optical receivers," *Proceedings of the IEEE,* vol. 78, no. 8, pp. 1369-1394, 1990.

[70] G. P. Agrawal, *Fiber-optic communication systems*. John Wiley & Sons, 2012.

[71] I. Fatadin, S. J. Savory, and D. Ives, "Compensation of quadrature imbalance in an optical QPSK coherent receiver," *IEEE Photonics Technology Letters,* vol. 20, no. 20, pp. 1733-1735, 2008.

[72] E. Ip and J. M. Kahn, "Digital equalization of chromatic dispersion and polarization mode dispersion," *Journal of Lightwave Technology,* vol. 25, no. 8, pp. 2033-2043, 2007.

[73] S. J. Savory, "Digital filters for coherent optical receivers," *Optics express,* vol. 16, no. 2, pp. 804-817, 2008.

[74] T. Nakagawa *et al.*, "Non-data-aided wide-range frequency offset estimator for QAM optical coherent receivers," in *2011 Optical Fiber Communication Conference and Exposition and the National Fiber Optic Engineers Conference*, 2011: IEEE, pp. 1-3.

[75] M. Y. Sowailem *et al.*, "770-Gb/s PDM-32QAM coherent transmission using InP dual polarization IQ modulator," *IEEE Photonics Technology Letters,* vol. 29, no. 5, pp. 442-445, 2017.

[76] M. S. Faruk and K. Kikuchi, "Compensation for in-phase/quadrature imbalance in coherent-receiver front end for optical quadrature amplitude modulation," *IEEE Photonics Journal,* vol. 5, no. 2, pp. 7800110-7800110, 2013.

[77] P. O. Weigel *et al.*, "Bonded thin film lithium niobate modulator on a silicon photonics platform exceeding 100 GHz 3-dB electrical modulation bandwidth," *Optics express,* vol. 26, no. 18, pp. 23728-23739, 2018.

[78] F. A. Juneghani *et al.*, "Demonstration of non-symmetric thin-film lithium niobate modulator with a 3-dB bandwidth beyond 100 GHz," in *CLEO: Science and Innovations*, 2022: Optica Publishing Group, p. SF4G. 1.

[79] M. Xu *et al.*, "Thin-film lithium Niobate DP-IQ modulator for driverless 130 Gbaud 64 QAM transmission," in *Optical Fiber Communication Conference*, 2022: Optica Publishing Group, p. Th1J. 2.

[80] G. Chen *et al.*, "Compact 100GBaud driverless thin-film lithium niobate modulator on a silicon substrate," *Optics Express,* vol. 30, no. 14, pp. 25308-25317, 2022.

[81] X. Liu *et al.*, "A Highly Compact Thin-film Lithium Niobate Modulator with Low Half-wave Voltage," in *Optical Fiber Communication Conference*, 2022: Optica Publishing Group, p. Th1J. 6.

[82] E. Berikaa, M. S. Alam, and D. V. Plant, "Beyond 300 Gbps Short-Reach Links Using TFLN MZMs with 500 mVpp and Linear Equalization," *IEEE Photonics Technology Letters,* 2022 (Under review).

[83] J. Cho and L. Schmalen, "Construction of protographs for large-girth structured LDPC convolutional codes," in *2015 IEEE International Conference on Communications (ICC)*, 2015: IEEE, pp. 4412-4417.

[84] M. S. Alam, E. Berikaa, and D. V. Plant, "Net 350 Gbps/λ IMDD Transmission Enabled by High Bandwidth Thin-Film Lithium Niobate MZM," *IEEE Photonics Technology Letters,* 2022.

[85] E. Berikaa, M. S. Alam, and D. V. Plant, "Net 400-Gbps/λ IMDD transmission using a single-DAC DSP-free transmitter and a thin-film lithium niobate MZM," *Optics Letters,* vol. 47, no. 23, pp. 6273-6276, 2022.

[86] H. Yamazaki *et al.*, "Net-400-gbps PS-PAM transmission using integrated AMUX-MZM," *Optics Express,* vol. 27, no. 18, pp. 25544-25550, 2019.

[87] E. L. O. Batista and R. Seara, "On the performance of adaptive pruned Volterra filters," *Signal Processing,* vol. 93, no. 7, pp. 1909-1920, 2013.

[88] T. Rahman, S. Calabrò, N. Stojanovic, L. Zhang, J. Wei, and C. Xie, "LUT-assisted pre-compensation for 225 Gb/s/λ O-band transmission," in *45th European Conference on Optical Communication (ECOC 2019),* 2019: IET, pp. 1-4.

[89] P. Schulte and G. Böcherer, "Constant composition distribution matching," *IEEE Transactions on Information Theory,* vol. 62, no. 1, pp. 430-434, 2015.

[90] E. Berikaa *et al.*, "Net 67 Gbps Transmission Over 2 km at Sub 1 Vpp Using Packaged Silicon Photonic MZM," *IEEE Photonics Technology Letters,* vol. 34, no. 21, pp. 1139-1142, 2022.

[91] M. S. Alam, X. Li, M. Jacques, E. Berikaa, P.-C. Koh, and D. V. Plant, "Net 300 Gbps/λ Transmission Over 2 km of SMF With a Silicon Photonic Mach-Zehnder Modulator," *IEEE Photonics Technology Letters,* vol. 33, no. 24, pp. 1391-1394, 2021.

[92] A. Mohammadi, Z. Zheng, X. Zhang, L. A. Rusch, and W. Shi, "Segmented Silicon Modulator with a Bandwidth beyond 67 GHz for High-Speed Signaling," *Journal of Lightwave Technology,* 2023.

[93] G.-W. Lu, H.-B. Zhang, S. Shinada, J. Hong, Y. Cheng, and S. Yokoyama, "Power-efficient O-band 40 Gbit/s PAM4 transmitter based on dual-drive cascaded carrier-depletion and carrier-injection silicon Mach-Zehnder modulator with binary driving electronics at CMOS voltages," *IEEE Journal of Selected Topics in Quantum Electronics,* vol. 27, no. 3, pp. 1-8, 2021.

[94] O. Dubray *et al.*, "30Gbit/s PAM-4 transmission by modulating a dual silicon ring resonator modulator," in *2016 IEEE Optical Interconnects Conference (OI),* 2016: IEEE, pp. 6-7.

[95] T. Barwicz *et al.*, "Advances in interfacing optical fibers to nanophotonic waveguides via mechanically compliant polymer waveguides," *IEEE Journal of Selected Topics in Quantum Electronics*, vol. 26, no. 2, pp. 1-12, 2020.

[96] A. Janta-Polczynski *et al.*, "Self-Aligned Polymeric Fiber Interface with 20/mm Port Density and 1.1 dB O-Band Loss," in *2020 European Conference on Optical Communications (ECOC)*, 2020: IEEE, pp. 1-3.

[97] E. El-Fiky, A. Samani, D. Patel, M. Jacques, M. Sowailem, and D. V. Plant, "400 Gb/s O-band silicon photonic transmitter for intra-datacenter optical interconnects," *Optics express,* vol. 27, no. 7, pp. 10258-10268, 2019.

[98] D. Patel *et al.*, "Design, analysis, and transmission system performance of a 41 GHz silicon photonic modulator," *Optics express,* vol. 23, no. 11, pp. 14263-14287, 2015.

[99] E. Berikaa, M. S. Alam, Y. Hu, W. Li, and D. V. Plant, "C-band 100 Gb/s Transmission over 40 km SSMF Using a Silicon Photonic Vestigial Sideband Transmitter Based on

Dual-Drive MZM and Passive Optical Delay Line," in *2023 Optical Fiber Communications Conference and Exhibition (OFC)*, 2023: IEEE, pp. 1-3.

[100] T. Bo, H. Kim, Z. Tan, and Y. Dong, "Optical Single-Sideband Transmitters," *Journal of Lightwave Technology,* vol. 41, no. 4, pp. 1163-1174, 2023.

[101] Y. Zhu, L. Li, X. Miao, and W. Hu, "Time skew enabled vestigial sideband modulation for dispersion-tolerant direct–detection transmission," *Optics Letters,* vol. 45, no. 22, pp. 6138-6141, 2020.

[102] M. S. Alam, X. Li, Z. Xing, M. E. Mousa-Pasandi, M. O'Sullivan, and D. V. Plant, "C-band 4× 200 Gbit/s transmission over 40 km of SSMF with an RF delay-assisted WDM-SSB transmitter," in *Optical Fiber Communication Conference,* 2021: Optica Publishing Group, p. W6A. 50.

[103] D. Patel, *Design, analysis, and performance of a silicon photonic traveling wave Mach-Zehnder modulator*. McGill University (Canada), 2015.

[104] J. Harley, D. Mcghan, S. O. Gharan, and E. Maniloff, "Coherent Laser Specifications and Control for 800G 10km application," 2022.

[105] E. Berikaa, M. S. Alam, and D. V. Plant, "Unamplified Coherent Transmission of Net 500 Gbps/Polarization/λ for Intra-Datacenter Interconnects," *IEEE Photonics Technology Letters,* vol. 34, no. 21, pp. 1135-1138, 2022.

[106] B. M. Oliveira, A. Lorences-Riesgo, F. P. Guiomar, M. C. Medeiros, and P. P. Monteiro, "Optimizing probabilistic constellation shaping for amplifier-less coherent optical links," *Journal of Lightwave Technology,* vol. 39, no. 13, pp. 4318-4330, 2021.

[107] J. Cheng, C. Xie, M. Tang, and S. Fu, "Power consumption evaluation of ASIC for short-reach optical interconnects," in *2018 23rd Opto-Electronics and Communications Conference (OECC),* 2018: IEEE, pp. 1-2.

[108] E. Berikaa *et al.*, "Next-Generation O-band Coherent Transmission for 1.6 Tbps 10 km Intra-Datacenter Interconnects," *Journal of Lightwave Technology,* 2023.

[109] H. Ludvigsen, M. Tossavainen, and M. Kaivola, "Laser linewidth measurements using self-homodyne detection with short delay," *Optics Communications,* vol. 155, no. 1-3, pp. 180-186, 1998.

[110] M. Selmi, Y. Jaouen, and P. Ciblat, "Accurate digital frequency offset estimator for coherent PolMux QAM transmission systems," in *2009 35th European Conference on Optical Communication*, 2009: IEEE, pp. 1-2.

[111] P. Xia *et al.*, "8× 250 Gbit/s PAM4 transmission over 1 km single mode fiber with an all-silicon LAN WDM transmitter," in *Optical Fiber Communication Conference*, 2023: Optica Publishing Group, p. Tu3I. 6.

[112] I. Lyubomirsky, J. Riani, B. Smith, S. Bhoja, and R. Baca, "Baseline Proposal for 400G/80km." [Online]. Accessed: May. 20, 2023 Available: https://www.ieee802.org/3/cn/public/18_11/lyubomirsky_3cn_02a_1118.pdf

[113] J. Kim *et al.*, "8.1 a 224Gb/s DAC-based PAM-4 transmitter with 8-tap FFE in 10nm CMOS," in *2021 IEEE International Solid-State Circuits Conference (ISSCC)*, 2021, vol. 64: IEEE, pp. 126-128.

[114] Z. Jiang, "High Data Rate DMT SERDES Design," Carleton University, 2022.

[115] E. Berikaa, M. S. Alam, and D. V. Plant, "Beyond 300 Gbps Short-Reach Links Using TFLN MZMs With 500 mV pp and Linear Equalization," *IEEE Photonics Technology Letters*, vol. 35, no. 3, pp. 140-143, 2022.

[116] C. Lam, X. Zhou, and H. Liu, "200G per Lane for beyond 400GbE," in *Proc. IEEE 802.3 NEA Meeting*, 2020, pp. 1-20.

[117] T. Jyo, M. Nagatani, J. Ozaki, M. Ishikawa, and H. Nosaka, "12.3 A 48GHz BW 225mW/ch linear driver IC with stacked current-reuse architecture in 65nm CMOS for beyond-400Gb/s coherent optical transmitters," in *2020 IEEE International Solid-State Circuits Conference-(ISSCC)*, 2020: IEEE, pp. 212-214.

[118] "Aerodiode model 3 (O-band) DFB laser." [Online]. Accessed: May. 20, 2023, Available: https://www.aerodiode.com/product/1310-nm-laser-diode

[119] F. Change and R. Chen, "Relative Cost Analysis on IMDD vs Coherent for 800G-LR."

[120] H. Li *et al.*, "A 112 Gb/s PAM4 CMOS optical receiver with sub-pJ/bit energy efficiency," in *2019 IEEE Optical Interconnects Conference (OI)*, 2019: IEEE, pp. 1-2.

[121] Y. Seual *et al.*, "A 1.41 pJ/b 224Gb/s PAM-4 SerDes Receiver with 31dB Loss Compensation," in *2022 IEEE International Solid-State Circuits Conference (ISSCC)*, 2022, vol. 65: IEEE, pp. 114-116.

[122] E. Berikaa *et al.*, "Silicon photonic single-segment IQ modulator for net 1 Tbps/λ transmission using all-electronic equalization," *Journal of Lightwave Technology,* 2022.

[123] Z. Zheng, A. Mohammadi, X. Zhang, L. A. Rusch, and W. Shi, "Net 556.8 Gbps/pol Coherent Transmission Enabled by a Two-segment All-Silicon Modulator," in *2022 European Conference on Optical Communication (ECOC)*, 2022: IEEE, pp. 1-4.

[124] Z. Zheng, A. Mohammadi, X. Zhang, W. Shi, and L. A. Rusch, "Pushing Capacity Limits with Multi-Segment SiP Modulators," *Journal of Lightwave Technology,* 2023.

[125] D. Patel, A. Samani, V. Veerasubramanian, S. Ghosh, and D. V. Plant, "Silicon photonic segmented modulator-based electro-optic DAC for 100 Gb/s PAM-4 generation," *IEEE Photonics Technology Letters,* vol. 27, no. 23, pp. 2433-2436, 2015.

[126] A. Samani *et al.*, "Experimental parametric study of 128 Gb/s PAM-4 transmission system using a multi-electrode silicon photonic Mach Zehnder modulator," *Optics express,* vol. 25, no. 12, pp. 13252-13262, 2017.

[127] A. Samani *et al.*, "A low-voltage 35-GHz silicon photonic modulator-enabled 112-Gb/s transmission system," *IEEE Photonics Journal,* vol. 7, no. 3, pp. 1-13, 2015.

[128] D. Patel *et al.*, "A 4× 4 fully non-blocking switch on SOI based on interferometric thermo-optic phase shifters," in *2014 Optical Interconnects Conference*, 2014: IEEE, pp. 104-105.

[129] S. S. Azadeh *et al.*, "Low V π Silicon photonics modulators with highly linear epitaxially grown phase shifters," *Optics express,* vol. 23, no. 18, pp. 23526-23550, 2015.

[130] S. Zhalehpour *et al.*, "All silicon IQ modulator with 1Tb/s line rate," in *2020 Optical Fiber Communications Conference and Exhibition (OFC),* 2020: IEEE, pp. 1-3.

[131] K. Zhong *et al.*, "140-Gb/s 20-km Transmission of PAM-4 Signal at 1.3 μm for Short Reach Communications," *IEEE Photonics Technology Letters,* vol. 27, no. 16, pp. 1757-1760, 2015.

[132] H. Zamiri-Jafarian and S. Pasupathy, "Complexity reduction of the MLSD/MLSDE receiver using the adaptive state allocation algorithm," *IEEE Transactions on Wireless Communications,* vol. 1, no. 1, pp. 101-111, 2002.

[133] E. Berikaa, M. S. Alam, Y. Hu, S. Lessard, and D. V. Plant, "Equalization Noise Reduction Through Constellation Distortion in Coherent Systems," in *Signal Processing in Photonic Communications*, 2022: Optica Publishing Group, p. SpM2I. 4.

[134] S. Ummethala *et al.*, "Hybrid electro-optic modulator combining silicon photonic slot waveguides with high-k radio-frequency slotlines," *Optica*, vol. 8, no. 4, pp. 511-519, 2021.

[135] X. Liu and Q. Fan, "Inter-Channel FWM Mitigation Techniques for O-band WDM Based 800G/1.6 T LR and 5G Fronthaul Applications," in *2023 Optical Fiber Communications Conference and Exhibition (OFC)*, 2023: IEEE, pp. 1-3.

[136] K. Giewont *et al.*, "300-mm monolithic silicon photonics foundry technology," *IEEE Journal of Selected Topics in Quantum Electronics*, vol. 25, no. 5, pp. 1-11, 2019.